This document is comprised by:

1. **Response to reviewer 1 (P2-P23)**
2. **Response to reviewer 2 (P24-P38)**
3. **A list of all relevant changes made in the manuscript (P39-P50)**
4. **Revised manuscript with changes marked-up**

Response to Reviewer 1

We thank Reviewer 1 for her thoughtful and helpful review of our paper. The comments have helped us improve the manuscript significantly. Our reply to reviewer comprises two parts: (1) some short general statements and (2) point-by-point reply to comments from reviewer. Reviewers comments are in blue type. *Extracts from our revised manuscript are in italics.*

Section one: general statements

1. This work contains data which are completely new.

We would like to emphasize that the sequence of microstructures and CPOs developed with increasing strain has not been documented before for ice deformed at cold temperatures (-20, -30 °C). This is highlighted by one of the comments by the reviewer: "The hypothesis that GBM being less active at low temperature, the impact of grain rotation driven by intracrystalline slip prevails is much clearer, especially since it is very coherent with the observations that the cone angle is reduced, and more orientations are found close to the vertical. This assertion is, indeed, justified by the experimental observations. This is, in fact, the main "novelty" of the presented work and should be emphasised more."

Earlier work showing the up-strain microstructures and CPOs (e.g. Jacka & Macagnan, 1984; Montagnat 2015) are at warm conditions where the CPO evolves towards an open cone (small circle). Experiments at colder temperatures (-30 °C and colder) to strains of ~ 20% (Craw et al., 2018; Prior et al 2015) show CPOs have maxima of c-axes parallel to compression. No published work shows the up-strain evolution of microstructures or CPOs at -20 or -30 °C (or colder temperatures). Jacka & Li (2000) show CPOs at ~10% strain at ~ -15 and -20 °C and ~ 3% strain at -45 °C but include no microstructural data and do not explore the up-strain evolution. Recent work by Wilson et al (2019) shows CPOs at -15 and -20 °C at 20% strain, but show no up-strain evolution. In this paper the up-strain sequence at -30°C documents the evolution towards a cluster CPO, the sequence at -10 °C the evolution towards an open cone CPO and the sequence at -20 °C something between these two. Understanding how and why different CPOs develop as a function of temperature should give a better insight into the mechanisms that control CPO development and mechanical behaviour.

2. Different interpretations can be made from the same observation.

One of the reviewer's objections relates to our interpretation of the microstructural development as involving grain boundary sliding (GBS). We accept that the factual observations could be interpreted in different ways and in the revision, we include some alternative interpretations (including "spontaneous" nucleation) of the data, with some discussion of the merits and drawbacks of each of these interpretations. We hope that we have kept the observations and interpretations clearly separated and we have reduced the emphasis on our preferred interpretation of GBS. We have also identified some of the tests that may facilitate distinguishing these different interpretations in the future. Some more details are included in answers to specific points.

The reviewer's comments highlight that our original manuscript did not really make clear that we do interpret intracrystalline dislocation glide that causes lattice rotation as one of the key processes controlling CPO development. We hope that we have made this much clearer in the revised manuscript. The operation of a GBS process, if this is correct, would be additional to the role of intracrystalline dislocation glide and associated recovery and recrystallisation processes.

Section two: point-by-point reply to comments

1. P3 l. 28: why should the sample be cooled in liquid nitrogen? Couldn't that induce some thermal stress due to the fast and strong temperature gradient? Changes in local microstructure, dislocation arrangements, etc. are expected to occur in the first minutes after the test... so this quenching should not avoid it.

The purpose of cooling deformed ice samples in liquid nitrogen is to preserve the ice microstructure during a long-term storage and also for intercontinental transfer (using a nitrogen dry shipper). The time interval between ice deformation work and cryo-EBSD analyses is normally longer than one month. Very cold storage has several advantages:

1. The colder temperatures minimise the chance of long-term microstructure change.
2. The storage is much more reliable than storing in an electric freezer. The dewar usually lasts one to two months between liquid nitrogen top ups and can easily stay cold for > 6 months if fully filled (as has just been done for COVID 19 lock down).
3. The storage solution is much cheaper than a very cold (-80C) freezer.

Thermal shock is a risk with liquid nitrogen storage. Plunging a -20°C sample directly into liquid nitrogen will cause the sample to shatter. More careful handling prevents any fracturing. We have some samples (e.g. MIT666 (Prior et al., 2012)) that have been cycled between liquid nitrogen and much warmer temperatures (e.g. for grain growth experiments (Becroft, 2015)) with no discernible changes to structure or microstructure. We applied a staged cool-down method to progressively cool deformed samples to a liquid nitrogen temperature:

1. Firstly, samples are cooled down to -30 °C in a chest freezer for ~5 minutes while the indium jacket is being peeled off.

2. Secondly, samples are transferred into liquid nitrogen mist at ~ -100 °C for ~10 minutes.

3. Finally, samples are transferred to a liquid nitrogen dewar for a long-term storage.

We use the staged cool-down process to prevent a drastic temperature change, which might lead to thermal stress in sample. The staged cool-down method was not clarified in the manuscript and it has been clarified in the modified version.

We always worry that there could be some post-deformational changes that change the sample microstructure after load has been removed but before the sample is "quenched". Our procedures try to minimise this and as a minimum, ensure all samples are treated in a similar way. After each deformation run ended, we drove back the driving piston, depressurized the pressure vessel, and extracted the sample from deformation rig in 10 to 30 minutes. Each sample was exposed at room temperature for less than 30 seconds for taking photos. Soon after, the samples were cooled down to a liquid nitrogen temperature using the staged cool-down method.

Static annealing of the ice microstructure during the sample extraction is a potential issue in all ice deformation experiments. The experiments shown by Hidas and others (2017) quantified the ice microstructural changes during thermal annealing at -5 to -2 °C. They show no significant ice microstructural change in pre-deformed samples over the time scales of our sample extraction process. More specifically, Hidas and others (2017) shows deformation-induced tilt boundaries and kink bands remain stable during early stages of annealing. It takes >24 h of annealing to start to erase these microstructures.

We have added a statement into section 2.2: "*Minor static recovery of the ice microstructures may happen on this timescale (Hidas et al., 2017), but significant change in CPO or grain size is unlikely.*"

2. P7 l. 8-10: in the paragraph just before it is mentioned that the grain size distributions are mostly bimodals, and therefore not gaussians... The mean and STD parameters are therefore not suited to described them, since they do not represent well the given statistics. I therefore suggest the authors to provide medians and quartile data instead to better fit the type of distributions observed.

The reviewer has a good point and we have addressed this by including a wider range of grain size measurements, that may reflect better a scalar representation of a skewed distribution; for example, we have added median and quartile grain size values to Table 3. We have also kept the values of mean grain size in the paper, as this is a common measure used in microstructural studies and provides some comparability to those studies.

3. P7 l. 30: couldn't it exist a bias link to the lack of resolution in step size and misorientation when getting toward smaller subgrains?

We'll discuss the two issues separately:

The data filtering process removes grains with area equivalent diameters lower than 20 µm. Thus, there is an artificial lower cut off to the grain size and sub grain distributions (as there always is for any microscopic method). Our grain size distributions show peaks above the 20 µm cut off, these peaks are unlikely to change even though we may miss some smaller grains. The subgrain peak in all cases is ~ 20 µm (i.e. at th resolution cut-off), particularly at lower temperatures. The true peak subgrain size is therefore likely to be < 20 µm and it is probable that we are missing a substantial population of smaller subgrains in our analyses. We acknowledge this limitation and have added a statement into section 3.3.3: "*In many cases, particularly at lower temperatures, the peak corresponds to the lower grain size resolution (cut off) indicating that we could be missing smaller subgrains. For this reason, the peak subgrain sizes are not useful and the median and mean subgrain sizes probably represent overestimates.*"

The orientation resolution in these EBSD maps is ~0.5°, so that we cannot reliably identify misorientations of ~1°. The misorientation threshold chosen for identifying subgrain boundaries is ⩾ 2°, the lowest angle that returns reliable results for our data. Lower angle subgrain boundaries could exist and at least one comparison of TEM and EBSD has shown that this is the case (in quartz :(Shigematsu et al., 2006)). We have added a statement into section 2.4: "*The angular resolution (error of crystallographic orientation measurement of each pixel) of the EBSD data is ~0.5°.*"

4-1. Part 3.2.3: this is not clear to me how is the subgrain size defined and calculated.

Thanks for pointing our lack of clarity in defining how subgrain size was defined and calculated.

We have added a statement in section 2.5.1: "*Deformed ice is often characterised by a development of subgrain boundaries where the misorientations between neighbouring pixels are lower than the misorientation angle threshold of grain boundaries (e.g. Montagnat et al., 2015; Weikusat et al., 2017). An ice grain can be separated into several subgrains by one or more subgrain boundaries. We calculated subgrain size using boundary misorientation thresholds of ⩾ 2 ° . Grain size and subgrain size were calculated as the diameter of a circle with the area equal to the measured area of each grain or subgrain.*"

4-2. Although we observe a clear grain boundary structure in the figures, there appears no clear subgrain structure (as one could observe in some minerals or metals for instance). On the contrary, subgrains appear more like straight tilt bands or kink bands, with, in some places, some variations around the straight shape.

We agree with the observation from the reviewer that suggests many of the subgrain boundaries are straight tilt bands or kink bands. The subgrain structure in the submitted manuscript version was revealed by the Weighted Burgers vector (WBV) method. We didn't make it clear that the measurement of subgrain sizes were not based on the WBV data, but on the misorientations between adjacent pixels. The WBV was a legacy of a much earlier manuscript and the reviewer's comments have highlighted that it is better removed. The new maps (Fig. 4(c), 5(c), 6(c)) show subgrain boundaries that correspond to the much simpler misorientation threshold. We modified statements on section 3.3.1 to: "*Distinct sub-grain boundaries can be observed in all the samples (Fig. 4 (c), 5 (c) and 6 (c)). Many of the subgrain boundaries appear to be straight, some with slight curvature. A small number have strong curvature. Interconnected subgrain boundaries can be observed in some of the grains. Subgrain boundaries subdivide grains into subgrains.*"

Figure R1.1 shows the structures of subgrain boundary in deformed ice samples as well as other experimentally or naturally deformed minerals and metals, e.g. quartz (Cross et al., 2017; Killian and Heilbronner, 2017), Olivine (Hansen et al., 2012), Magnox alloy (Wheeler, 2009) and Zircon (MacDonald et al., 2013). We added a new statement section 4.1.2: "*The subgrain boundary geometry is comparable with other experimentally or naturally deformed rock and metal samples, e.g. quartz (Cross et al., 2017a; Killian and Heilbronner, 2017), Olivine (Hansen et al., 2012), Magnox alloy (Wheeler, 2009) and Zircon (MacDonald et al., 2013).*"

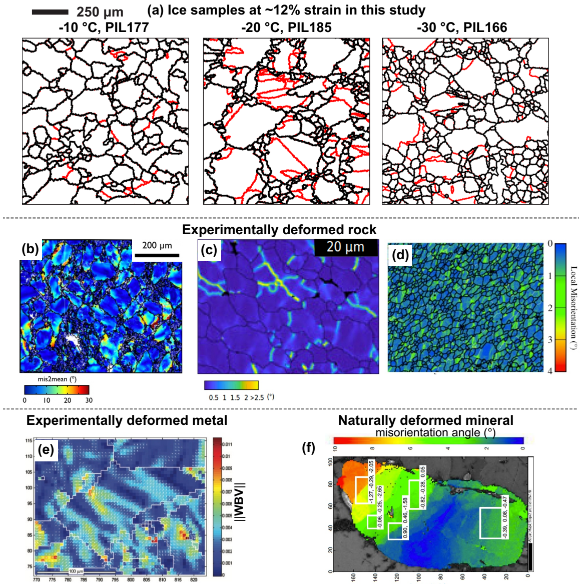

Figure R1.1. Illustrations of subgrain boundaries developed in experimentally deformed materials. **(a)** Experimentally deformed ice samples to ~12% true axial strain at -10, -20 and -30 °C from this study. Sub-grain boundaries where misorientation between neighbouring pixels between 2° and 10° are coloured red. Grain boundaries where misorientation between neighbouring pixels higher than 10° are coloured black **(b)** Experimentally deformed quartz sample W1051 (189±30 MPa, 1000 °C, 41% axial strain, 1.9-2.9 × 10^{-5} s^{-1}) from Cross et al., 2017. Each pixel is coloured by the value of mis2mean (misorientation between each pixel and the mean orientation of their parent grain). **(c)** Experimentally deformed quartzite sample W946 (1.5 GPa, 875 °C, 3.3 shear strain, 3.1 × 10^{-5} s^{-1}) from Killian and Heilbronner, 2017. Each pixel is coloured by Kernel average misorientation (KAM) of a 24-pixel neighbourhood. **(d)** Experimentally deformed olivine sample PT0552 (136 MPa, 8.8 shear strain, 0.551 × 10^{-3} s^{-1}) from Hansen et al., 2012. Each pixel is coloured by local misorientation calculated with 5 by 5 pixel averaging filter. **(e)** Experimentally deformed Magnox alloy containing 0.9% Al and 0.005% Be (30% strain, 200 °C, 1.9 × 10^{-4} s^{-1}) from Wheeler et al., 2009. Each pixel is coloured by the weighted Burgers vector (WBV) magnitude.

The 3D WBV is projected onto the map plane and marked as arrow. **(f)** Naturally deformed Zircon grain BP06/3 from MacDonald et al., 2013. Each pixel is coloured by a misorientation angle calculated from its orientation relative to a given point.

4-3 I would be curious to see, for instance, how was measured this subgrain size in the sample deformed at 3% at -10°C, or at 12% at -20°C. I think that the author should clarify this technical aspect as they make a lot of explanation rely on such "average" parameters. Furthermore, provided it is calculated properly, I doubt the distribution is normal, and I think that a metric other than the average would fit best.

The reviewer is correct that the subgrain size distributions are not normal they are skewed in a manner similar to the grain size distributions. In our modification we have tried to focus on elements of the data that are robust and helpful in interpretation. These are basically that subgrains exist and they are smaller than grains. We have removed the data and discussions related to subgrain sizes calculated using boundary misorientation angles of 4°, 6° and 8° (boundary hierarchies) and we have both mean and median subgrain sizes for comparison with grain sizes. The new presentation of data leads to a statement in section 3.3.3: "*Subgrain size distributions (Fig. 4(e), 5(e) and 6(e)) are similar to the grain size distributions (Fig. 4(d), 5(d) and 6(d)), but the median and mean subgrain sizes are smaller than median and mean grain sizes (Table 3).*"

4-4 In particular, the following assertion is questionnable: "because subgrain rotation recrystallization should produce grains that have similar sizes with subgrains, while bulging nucleation should produce grains that have smaller sizes than subgrains" that rely on a parameter (subgrain size) that is ill measured here, since subgrain structure does not resemble at all the one observe in quartz (Halfpenny et al 2012).

We agree with the reviewer that in this case this approach lacks robustness. We removed the extended discussion that including hypotheses of bulging nucleation in the revised manuscript.

4-5 On top of that, this expected hierarchy of grain size depending from the nucleation mechanism comes from one study on quartz and should not be taken as granted, see for instance Humphreys 2004 (Materials Science Forum) that shows clearly a bulged grain much larger that the surrounding subgrains. It will therefore depend on the material and its anisotropy, and on the resolution of the observations (ability to distinguish between a grain resulting from a bulge and one resulting from subgrain rotation...)

We agree that in this case the boundary hierarchy analyses do not give useful insight and we have removed the hierarchy data and related description and discussion.

5-1 p8 l. 8-9: To consider <D_small> as a good representative of the mean recrystallized grain size is also a strong hypothesis that should be justified (either by some specific observations or by references from previous work). It will, in particular, depend on the relative effect of grain boundary migration compare to nucleation during recrystallization (and therefore on the temperature of the test) since an apparent small grain size at high GBM rate could well be a 2D cut of a strongly lobated grain, while, at lower temperature (lower GBM rate), small grains indeed are newly recrystallized grains (see for instance the sample deformed at 8% at -10°C, could one certify that small grains observed on the 2D sections are indeed small grains?). Here again appears the necessity of statistic metrics adapted to the observed distributions.

Small grains observed from the EBSD data can be a 2D cross section of a larger 3D grain. We thank the reviewer for these comments as they have pushed us to complete new analyses aiming at quantifying the effects of two distinct (albeit related) stereological issues that add value to this paper and maybe will be useful to others as analytical approaches. The first issue relates to the misidentification of "small" grains, as these could appear from slices cut close to the perimeter of a large grain in 3-D (Underwood, 1973). The second issue relates to the oversampling of grains that have highly irregular, branching shapes in 3-D and appear more than once on a 2-D surface (Hooke and Hudleston, 1980; Monz et al, 2020). The new analyses are presented in section 3.3.2 (for observation) and 4.1.2 (for discussion). Details of the stereological analyses are presented in section S3 and S4 of the supplementary material. Here we present key findings:

To assess the first issue (misidentification of "small" grains) we extracted one-dimensional grain size measurements (by linear intercept) from two-dimensional maps. From this analysis, we can state whether a "small" 1-D grain is indeed a "small" grain in 2-D. At ~20% strain the percentage of "small" grains on a 1-D line that correspond to "small" grains in the 2-D EBSD map is 64%, 76% and 43% at -30, -20 and -10 °C, respectively. These data suggest that at 20% strain the presence of "small" grains in 3D is likely, with the confidence in this statement increasing at reduced temperatures. Another observation supports this. Figure R1.2 shows examples of "big" and "small" grains in deformed to ~20% strain at -10 °C and -30 °C. Many "small" grains have "small" grain neighbours. At -30 °C some "small" grains are entirely surrounded by other "small" grains. At -10 °C there are lines of "small" grains in contact along the boundary between "large" grains.

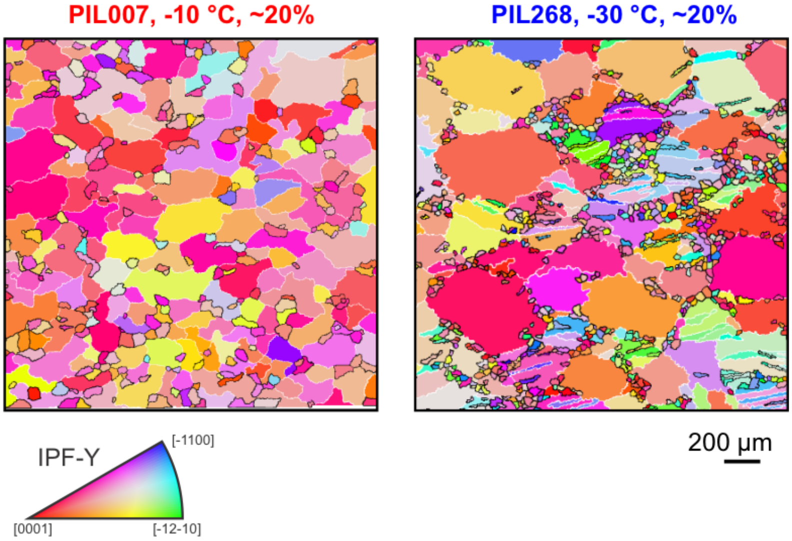

Figure R1.2. Examples of "big grains" and "small grains" in PIL007 deformed at -10 °C to ~20% strain, and PIL268 deformed at -30 °C to ~20%. The "small grains" have black grain boundaries, the "big grains" have white grain boundaries. Each grain is coloured by mean orientation with IPF-Y colour code.

It is very difficult (and at -30 C impossible) to have all of these "small" grains linked to large grains in the third dimension whilst maintaining a microstructure that looks like the microstructures in these maps. This is the case at 20% strain. At lower strains the percentage of "small" 1-D segments that correspond to "small" 2-D grains is lower so the confidence with which we can define "small" grains is reduced.

The 1-dimensional data also provide some insight into the second issue, oversampling of grains . In all samples >90% of 2-D grains along an arbitrary line are unique (that is, they are cut only once). Of course, with lines in multiple directions the total percentage of unique grains will decrease. As EBSD provides full crystal orientation data we can extend this analysis to entire maps. We can assess the likelihood of each 2-D mapped grain being connected in the third dimension to another 2-D mapped grain by comparing each grain's orientation (mean orientation) to all other grains within a certain distance (1mm is used here). If the misorientation between a grain and a nearby grain is below a certain threshold (10°) then we define them as being connected parts of the same grain in 3D. These thresholds probably overestimate the number of grains connected in 3D. 1mm is more than double the size of the largest grain and 10° is more than twice the median and significantly lower than the upper quartile in mis2mean data (the misorientation angle between all pixels in a grain and the mean orientation of that grain) for all samples. The percentage of “unique” grains (that only appear at the surface once) relative to all grains in a 2D map are higher than 70% at all temperatures and strains (Table S2-S4, Table 3).

The procedure outlined in the last paragraph allows us to estimate the number of “distinct” grains (where all 2-D grains attributed to the same 3-D grain are counted as one grain) in each map and from this, the number density (grain number per unit area) of “distinct” grains. The number density of “distinct” grains increases by more than a factor of 3 relative to the starting material in all samples at all temperatures: reaching values > 6 times initial at -10 °C and >12 times initial at the lower temperatures. The number density of “distinct” grains is generally higher at strains of $\varepsilon \geq \sim 12\%$ than at strains of $\varepsilon \leq \sim 8\%$ at all temperatures, and it is generally higher in samples deformed at -20 and -30 °C than samples deformed at -10 °C.

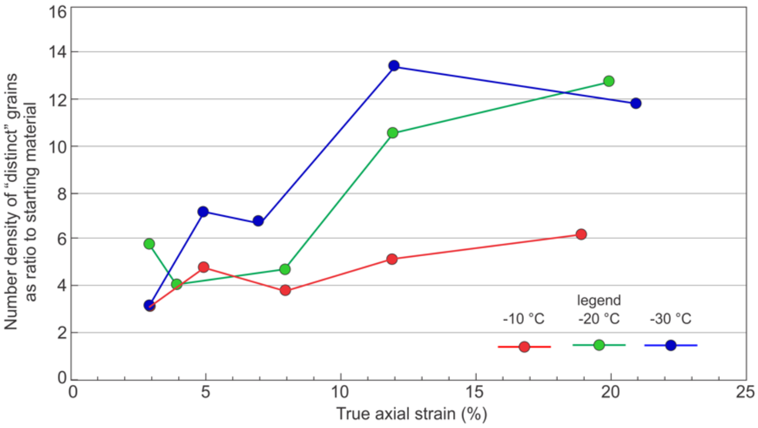

Figure R1.3. Number density of “distinct” grains as ratio to starting material relative to true axial strain.

The analyses above provide some confidence that in all the experiments the number density of grains has increased relative to the starting material and increases with strain. That requires new grains to be generated and any measure of average grain size to reduce. If we couple this to the grain size statistics presented and the analysis of whether we are misidentifying small grains, the weight of evidence suggests that we have a real population of smaller grains. Our confidence in this statement increases with reducing temperature and increasing strain.

Having outlined new analyses that add robustness to our statements about reducing grain size with strain and the existence of a population of “small” grains we come back to the issue of how we distinguish “big” and “small” grains. There will always be a degree of arbitrariness in this and to reflect this we added a statement in section 3.3.2: “*Our scheme for separating “big” and “small” grains is not perfect, but it does provide a fast and repeatable way of looking at the possible differences in microstructures and CPO of smaller and larger grains.*”

5-2 For the sake of clarity, I would suggest the authors not to mix result presentations and interpretations and keep interpretations for the discussion part. In particular when interpretation requires additional hypotheses on top of direct observations and results.

We have been through the manuscript and ensured the observations and interpretations are not mixed up in section 3 (results). We have kept necessary brief descriptions of process in section 3 only for the clarity of concepts introduced from other published works and not for interpretation of our own data.

6. P9 l. 13 "At -10 °C, the CPO intensity of "small grains" is lower than "big grains", and this contrast becomes strengthened as the temperature decreases." This could also be related with the fact that it is less straightforward to distinguish small grains from big grains for these tests, this should be mentioned here.

Yes, this is a very good point. The small grain population is easier to define and is better defined at low temperatures than at high temperature. This clearly relates to the differences in the balance of key processes at different temperatures. We hope that we have emphasised this the revised manuscript.

7. P11 l. 26 The authors mention "much of the stress increase prior to peak stress relates to elastic strain", and, as they notice just after, this is not coherent with the known Young modulus of ice of 9 Gpa... There is a broad literature, dating back to the 70's and 80's (Duval et al. 1983, Jacka 1984 for instance, and review by Schulson and Duval 2009) explaining that the transient behavior of ice is not elastic, but anelastic, and is related to the built of an internal stress field related to strain incompatibilities between grains. **I am therefore very astonished to read this sentence here, and I think that this should be corrected before publication**.

The "dissipative deformation" mentioned here is indeed plastic deformation related to intracrystalline dislocation slip, the porosity loss being very likely negligible.

Published literature labelled the stress increase prior to peak stress in constant displacement rate experiments as: "normally elastic" (Cole, 1987) and "quasi-elastic" (Kirby, 1987). The deceleration during primary creep in constant stress experiments was interpreted as effected by a "delayed elasticity", with a recoverable component of time-dependent elastic strain and an irrecoverable viscous strain (Mellor and Cole, 1982), and "anelasticity" (Duval et al., 1983). The reason we chose to describe the behaviour as substantially elastic is that we have other experiments where we can show that this part of the deformation is recoverable. However, these other experiments are higher rate experiments with slopes on the stress strain curve approaching the 9GPa modulus. The reviewers are correct in pointing out that, in the experiments presented in this paper, the slope is substantially below modulus and the behaviour is not substantially elastic. We have modified the statement in section 4.1.1: "*This likely includes anelastic deformation related to intergranular stress redistribution used to explain primary creep in constant load experiments (Duval et al, 1983). The curvature of the stress strain line at the start of each experiment may relate to initial porosity loss as suggested by rapid increases in ultrasonic p-wave velocity in comparable experiments by Vaughan et al., (2017).*"

8-1. Part 4.1.1: Discussion about GBS. The experimental results shown here present no evidence of a grain size sensitive mechanisms, since there is no initial grain size variation, no study of the influence of grain size on the stress – strain-rate relation. I therefore don't understand why GBS is mentioned here, since it is not necessary at all to explain the observations performed.

Indeed, all results presented here can be explained by intracrystalline dislocation slip accommodated by dynamic recrystallization mechanisms, as very well illustrated in the high quality EBSD observations performed. Furthermore, there exist a large number of studies showing that GBS occurs significantly only in fine-grained materials (see Boullier and Gueguen 1975, Goldsby and Kohlstedt 1997) where grain boundary diffusion can play a role (Ashby 1973). Diffusion in ice is known to be very slow, that renders the hypothesis of a diffusion-controlled mechanism quite unlikely, especially for large grains, and high strain-rate conditions as encountered here.

The particular set of experiments used in our paper does not include variable initial grain size. However, comparable experiments do show grain size sensitivity. The set of -10 °C experiments published by Qi et al 2017 have two different initial grain sizes. A plot of strain rate against the peak stresses (Fig. 3, copied below as Fig. R1.4) shows two different best fit lines for the two initial grain sizes. At peak stress (~ equivalent to min strain rate) grain size is unlikely to have changed substantially from the starting material (we have some new experiments to peak stress only that show this to be correct). The easiest interpretation of these data is that there is grain size sensitivity. In this case the sensitivity is manifest between grain sizes of ~0.25 (standard ice on Fig. 3 of Qi et al) and ~0.6mm (course grained ice). There is no clear distinction in the mechanical data for different initial grain sizes at flow stress (~tertiary creep). At flow stress, after strains of ~0.2, grain sizes have evolved substantially and mean grain sizes correlate with the stress magnitude following a piezometer type relationship, as reported for ice by Jacka and Li (1994).

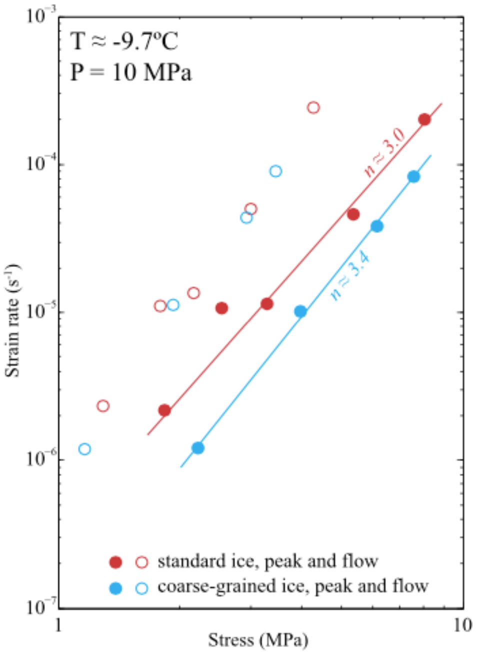

Figure R1.4. Plot of strain rate versus stress on logarithmic scales using data from Qi and others (2017).

GBS has always been a problem area since there are few clear microstructural indicators to show that it has occurred: in stark contrast to intracrystalline dislocation slip and accompanying recovery and recrystallisation. Older papers that identify GBS tend to be restricted to studies of very fine materials as it is in these materials that grain size sensitive mechanisms can dominate. An important concept in material science is that mechanisms can co-exist: the whole premise of deformation mechanism maps (https://engineering.dartmouth.edu/defmech/) is based on the idea that the total strain rate is the sum of the strain rates related to each contributing deformation mechanism. Recently, Kuiper and others (2019a, 2019b) applied the Goldsby-Kohlstedt composite flow law (which considers bulk strain rate as an additive contribution of dislocation creep and GBS) to model the deformation in NEEM ice core. The extrapolation of the experimental data to natural conditions suggests that "GBS-limited creep produces almost all deformation in the upper 2207 m of depth in the NEEM ice core (grain size between ~0.3mm and ~9mm)." GBS will contribute a larger proportion of total strain rate at fine grain sizes (e.g. experiments by Goldsby and Kohlstedt (1997)), but can still be significant at coarser sizes.

The advent of EBSD methods has allowed us to analyse microstructures in new ways and to tease out the potential for GBS in a wide range of materials. The change in misorientation axes from rational (along specific crystal directions) to random (w.r.t. crystal directions) with increasing misorientation and the weakening of CPO in recrystallised grains relative to porphyroclasts are two lines of evidence that are commonly used in the rock deformation community (starting with (Bestmann and Prior, 2003; Fliervoet et al., 1999; Jiang et al., 2000) to identify GBS as an operative mechanisms from the analysis of a final microstructure. We realised that we have not presented the basic misorientation analysis (Bestmann and Prior, 2003) and we have now included data on misorientation axes for low angle and high angle boundaries. These data, and the segmentation of CPOs for coarser and finer grains, show the same patterns that are commonly used to infer GBS in deformed rocks. This does not of course prove that GBS has occurred, it merely says that these ice experiments have microstructural characteristics that match other samples where those characteristics have been used to infer GBS.

If GBS does occur, our interpretation is that this is in addition to dislocation glide (Drury et al., 1985; Gifkins, 1976, 1977; Goldsby and Kohlstedt, 1997, 2001; Hirth, 2002; Hirth and Kohlstedt, 2003; Kuiper et al., 2019a; Kuiper et al., 2019b; Langdon, 2006, 2009; Warren and Hirth, 2006). Some authors term this dislocation accommodated GBS or "disGBS". In this mechanism, the total strain rate is the addition of a dislocation process (that changes crystal shapes and causes lattice rotation and internal distortion) and a GBS process that is probably controlled by a "viscous" mechanism within grain boundaries (small path length diffusion and/or asperity plasticity: idea originally from (Gifkins, 1976)). This is not the same as diffusion creep, irrespective of whether that is controlled by lattice diffusion (Nabarro-Herring creep) or grain boundary diffusion (Coble creep). GBS is required as an accompanying mechanism to polycrystalline diffusion creep, but in that case grain shape change is facilitated by the diffusive mass transfer processes. In diffusion creep, grain size sensitivity comes primarily from the increased path length for diffusion meaning that the change of shape of bigger grains takes longer. In "disGBS" the GBS itself is the prime source of grain size sensitivity. If there is a "viscous" grain boundary volume then the rheology will depend on the volume proportion of the sample that comprises grain boundaries: this proportion will increase with decreasing grain size.

8-2 The authors could try to calculate the strain-rate expected based on a GBS diffusion flow law (Nabarro-Coble for instance) for similar level of stress as the one of their experiences. They would likely see that the stress – strain-rate curves they obtained are not compatible with a GBS influencing mechanism.

Please see our comments related to diffusion creep in the last paragraph of the response to 8-1.

Also see the response to 15. This outlines how we have modified the discussion of weakening.

Here we expand a little to answer this question: this is from a paper we have in progress to model the effect of grain size on the mechanical evolution of deformed ice and is beyond the scope of inclusion in this paper. The ratio of stress drop after peak is ~35% for samples deformed at warm or cold temperatures (as pointed out elsewhere by the reviewer). A simple model uses just the GBS component of the Goldsby-Kohlstedt composite flow law. The strain rate of GBS can be expressed as:

$$\dot{\varepsilon} = A\sigma^{n} d^{-p} \exp\left(-\frac{Q}{RT}\right), \qquad (R1.1)$$

where A is a material-dependent parameter ($MPa^{-n}m^{p}s^{-1}$), σ is the stress (MPa), n is the stress exponent, d is the grain size (m), p is the grain-size exponent, Q is the activation energy ($kJmol^{-1}$), R is the gas constant ($= 8.314 \times 10^{-3}\ kJmol^{-1}K^{-1}$) and T is the absolute temperature (K). The flow law parameters of Q and A for GBS ($n = 1.8, q = 1.4$) were taken from Kuiper and others (2019a, 2019b). For each sample, we calculated the stress, σ, by substituting mean or median grain size and temperature (Table 3) into Eq. (R1.1). σ were normalised with respect to the peak stress. Figure R1.5 shows, the normalised stress estimated using the GBS flow law and measured strain rates and grain sizes as a function of strain at both -10 and -30 °C. There is much more work for us to do, but the models give stress strain patterns that have the same general form as the mechanical data, with an underestimate of weakening at -10C and an overestimate at -30 °C.

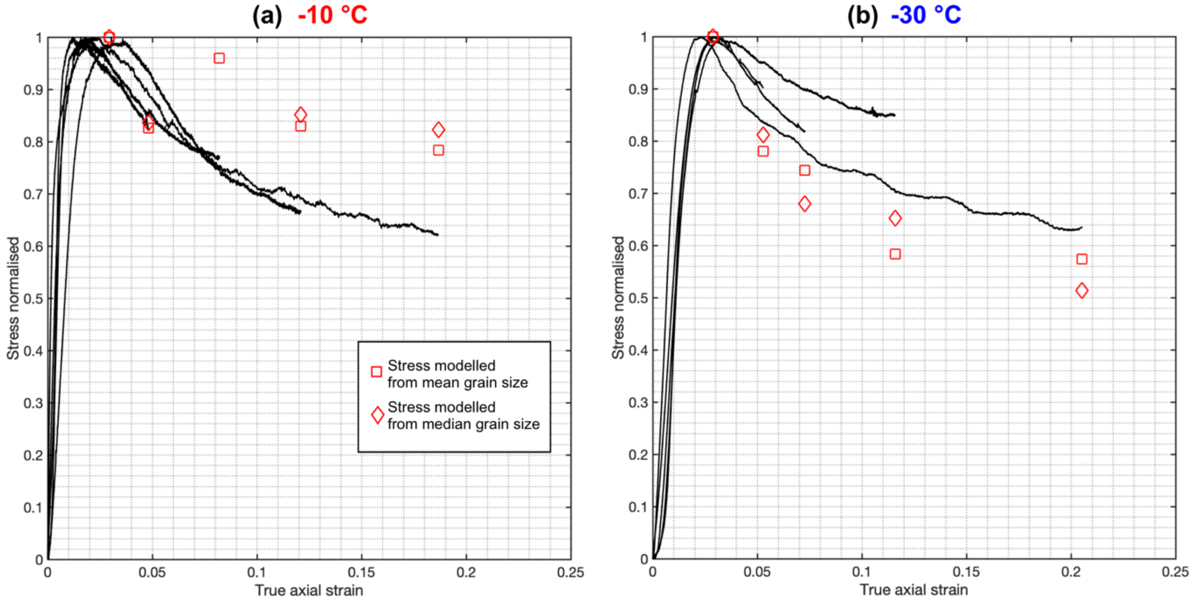

Figure R1.5. Normalised stress vs stress for samples deformed at **(a)** -10 °C and **(b)** -30 °C. For each temperature series, the stresses estimated from GBS mechanism are normalised by the estimated stress at ~3% strain.

9 Part 4.1.2: In this part, the authors use the subgrain size measurements to estimate the role of subgrain rotation in the recrystallization mechanisms.

Once again, the subgrain structure observed here is very far from the ones in quartz, to enable using the paper mentioned here as a reference (Trimby et al. 1998), and I think the authors should be much clearer about the way they evaluate the subgrain size before getting to strong an interpretation from this parameter.

Ice behavior, and in particular in the experiments presented here, is very different from the one of more isotropic materials in the sense that the dislocation substructures are not characterized by subgrain cells as observed in Al or Quartz for instance. This is due to the fact that subgrain substructures as observed in Quartz results from equivalent activity of several slip systems. Although one observe some c-dislocations in the microstructure, slip system activity in ice remains dominated by basal slip, and resulting subgrains have mostly the shape of large tilt and kink bands.

Only close to GB and triple junctions will we find more complex substructures. Is it enough to evaluate an "average" subgrain size? Care must therefore be taken before using interpretations coming from these more isotropic materials. And explanation should be given about how is this subgrain size measured here.

We agree with the reviewer about the lack of clarity of the measurement of subgrains. We have reduced significantly the discussions related to subgrain size. We have plotted subgrain boundary map based on misorientation angle of neighbouring pixels, added misorientation angle analyses and calculated median subgrain size to better support subgrain analyses. Please refer to responses to comments 4-1 to 4-5 for more details.

10 P13 l. 1-2: Indeed, Jacka and Li Jun 1994 evidenced a linear relationship between grain size and stress during dynamic recrystallization of polycrystalline ice (creep experiments, tertiary creep). I think that this should be mentioned here.

We agree with the reviewer. We added a statement in section 4.1.2: "Jacka and Li (1994) show a linear relationship between ice grain size and stress from deformed ice samples that reach tertiary creep."

11. P13. l. 5: here again, caution must be taken with making use of the subgrain size as it is still ill defined... and the ice case can not be compared straightforward to Halpenny et al. studies!

Indeed, observation given l. 16-17 goes in the direction of my remark... Subgrain size, if measurable here, can not be used similarly as in the other studies mentioned since there is no clear subgrain substructure. But, still, subgrain rotation could explain part of the recrystallization by, for instance, closing the bulges (see Chauve et al. 2017, Phil Trans), or by separating grains via highly misoriented tilt or kink bands. But, indeed, one can not talk about "continous" recrystallization as observed in Al for instance (see Sakai et al. Progress in Materials Science, 60(0):130–207, 3 2014 for a review).

We have modified the manuscript by presenting subgrain structures in a clearer way. Please refer to responses to comments 4-1 to 4-5 for details.

12. Part 4.1.3 p 14 l. 11: "Because grains with hard slip orientations should have greater internal distortions", there is absolutely no proof of that in ice, and some recent work tend to show that there is no systematic relation between orientation and strain localisation (see Grennerat et a. 2012 for instance) or between orientation and subgrains density (see Journaux et al. 2019 for instance). I think it should not be considered as granted, in particular when not shown directly in your experiments. Have you tried, for instance, to measure the density of GNDs as a function of grain orientation?

We modified our statement in 4.1.3 to: "*Cone-shaped c-axes CPOs have been related to strain-induced GBM favouring the growth of grains with easy slip orientations (high Schmid Factors) (Duval and Castelnau., 1995; Little et al., 2015; Vaughan et al., 2017; Qi et al., 2017). Linked to this is the idea that grains with hard slip orientations should have greater internal distortions (Duval and Castelnau., 1995; Bestmann and Prior 2003), and therefore store higher internal strain energy. If this is correct then hard slip grains are likely to be consumed by grains with easy slip orientations through GBM (Duval and Castelnau., 1995; Piazolo et al., 2006; Killian et al., 2011; Qi et al., 2017; Xia et al., 2018). However, we have to re-*

evaluate the detail of this idea, as recent studies on deformed ice samples show there is no systematic relation between orientation and strain localisation at low strain (Grennerat et al. 2012). Furthermore, studies of high-strain shear samples find no clear difference in the geometrically necessary dislocation density within the two maxima that develop in simple shear (Journaux et al. 2019). An alternative, and as yet incomplete, explanation from Kamb (1959) relates recrystallisation directly to the elastic anisotropy of crystals and through this to the orientation of the stress field. At this stage the observation that ice CPOs developed at relatively high temperature and particularly at low strain correspond to high Schmid factor orientations remains robust. The underlying mechanisms will need continual review as we collect new data."

We have done a whole series of quantitative Weighted Burgers vector (WBV) analyses on our EBSD data. However, we decided to pull all the WBV analyses out from this paper because we found a strong stereological effect, i.e. effects of different 2-D surfaces chosen from the same 3-D sample, on the GND statistics. We will present unpublished data only for discussion here. These data are subject for future publication. We conducted pixel-by-pixel WBV analyses on different orthogonal surfaces from the same deformed ice samples.

An analysis of a uniaxially deformed sample with a nearly random overall CPO (PIL165: 3% strain) illustrates the problem (Fig. R1.6). The absolute values of WBV and the relative values of WBV for grains in different orientations change depending upon which surface (normal or parallel to shortening) is being examined by EBSD.

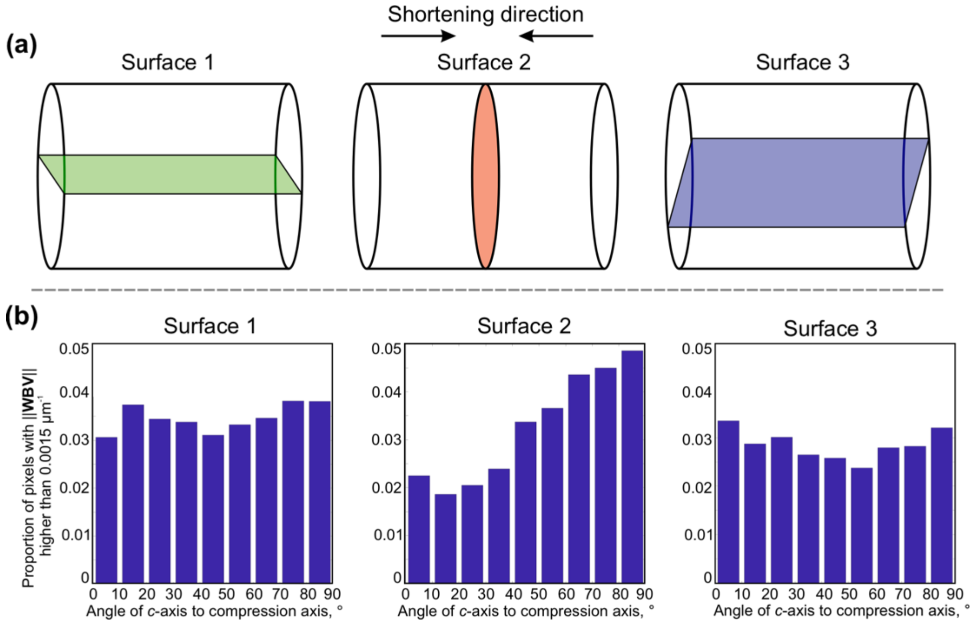

Figure R1.6. **(a)** Illustration of three orthogonal surfaces chosen from a sample (PIL165, -30 °C, ~3% strain, $1 \times 10^{-5} s^{-1}$) for WBV analyses. **(b)** Proportion of pixels with the magnitude of WBV (||**WBV**||) higher than 0.0015 µm^{-1} as a function of *c*-axis angle to compression axis.

In uniaxially compressed and sheared samples, with strong CPOs, the WBV of different texture components depend on the orientation of the sample surface analysed (Figure R1.7). The WBV of the of the distinct c-axis maxima (~ 45 degrees to compression and normal to shear plane respectively) depend on the orientation of the surface examined (Table R1.1).

(a) -10 °C, compression, ~12% strain

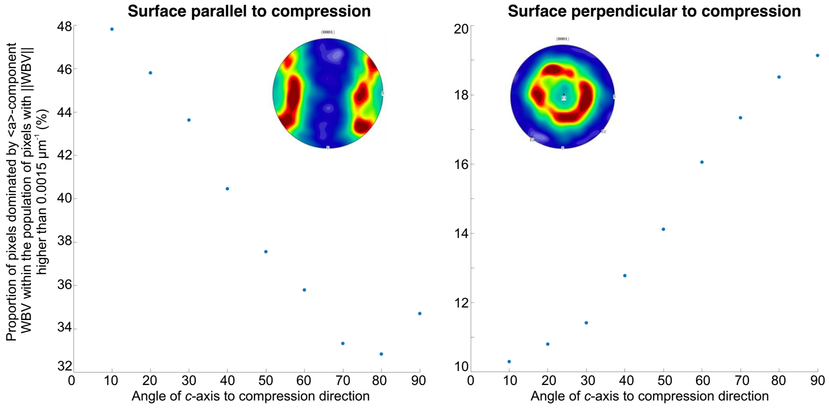

(b) -30 °C, direct shear, shear strain = ~1

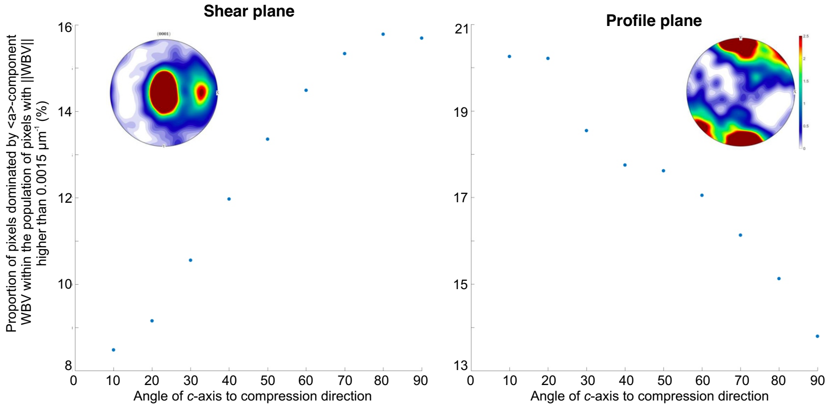

Figure R1.7. Differences between planes parallel or perpendicular to compression or shear in the proportion of basal-component pixels with ||**WBV**|| higher than 0.0015 μm^{-1} as a function of *c*-axis angle to compression for **(a)** PIL177, sample deformed with uniaxial compression at -10 °C to ~12% strain with a strain rate of $1 \times 10^{-5} s^{-1}$, and **(b)** PIL267, sample deformed with direct shear at -30 °C to a shear strain of ~1 with a shear strain rate of ~$1.8 \times 10^{-5} s^{-1}$.

Table R1.1. WBV statistics of grains at easy slip orientations from orthogonal surfaces

Sample No.	Surface type	*c*-axis orientations included in analysis	Proportion of pixels with the magnitude of WBV (||**WBV**||) higher than 0.0015 μm^{-1}	Proportion of pixels dominated by <a>-component WBV within the population of pixels with ||**WBV**|| higher than 0.0015 μm^{-1}
PIL177	Parallel to compression	45°±5° to compression axis	9%	42%
	Perpendicular to compression		3%	31%
PIL267	Shear plane	0°-30° to compression axis	10%	25%
	Profile plane		26%	51%

The statistics of WBV data are different when the same sample is looked at using different imaging surfaces. (e.g. shear plane vs profile plane). A running hypothesis is that the dislocations are mostly arranged in planar subgrain boundaries and the frequency of observation depends on the orientation of the grain relative to the observation surface. The orientation of the subgrain boundary is a function of grain orientation and Burgers vector.

Stereological effects need to be taken special care of when quantifying GNDs from the EBSD data acquired from a single 2-D sample surface. Conclusions derived from GND calculations can be strongly biased by different imaging surfaces. It is not straightforward to compare different texture components where the relative orientation of c-axes and imaging surface are different. Note that the data and conclusions in (Journaux et al., 2019) will probably not be compromised by this effect as, in the profile plane in which the samples were analysed, the M1 and M2 maxima have identical relative orientations of c-axis and analysis surface.

13. P14 l. 20: GBM instead of GMB

This mistake has been corrected.

14-1. About GBS and apparent texture weakening in small grains: to my point of view, this apparent texture weakening could be related to the nucleation process itself, and the fact that close to GBs, local misorientation can be high, and induce nucleation orientations varying from parent grains orientations (by bulging or subgrain rotation). This process would be enough to justify the small difference in texture concentration in small grains (that could also be due to more spread in data as there are less pixels measured in small grains, since GBs are interfering with the measurement, reducing its quality in small grain areas ?). See for instance the work of Falus et al. 2011 about Olivine for rotation recrystallization or Chauve et al. 2017 for the orientation of nucleus formed by bulging.

If "spontaneous" nucleation, driven by the relaxation of the dislocation-related internal stress field, can produce nuclei with orientations not related to their corresponding parent grains (Duval et al., 2012), we agree that this could lead to a weaker CPO. For this reason, we have included this as an alternative explanation to the GBS idea.

We added new statements in section 4.1.4: " '*"Spontaneous" nucleation driven (Duval et al 2012) by the relaxation of the dislocation-related internal stress field may produce nuclei with orientations not related to their corresponding parent grains (Falus et al., 2011; Chauve et al., 2017), and thus lead to a weaker CPO.'… 'Both hypotheses— "spontaneous" nucleation and GBS—explain a weakening of CPO in "small" grains and these two ideas are not mutually exclusive. Further work is needed to test both hypotheses. Most critical are experiments where nuclei can be observed whilst they are very small and subsequent misorientations can be documented, as might be possible with 3-D microscopy methods (Lauridsen et al, 2003; Poulson et al., 2004), and experiments where fiducial markers are used to confirm the physical existence of offsets on grain boundaries (Schmid et al, 1977; Spiers 1979 ; Beeré, 1978; Eleti et al., 2020).'* "

The data in Chauve et al (2017) can be interpreted equally well by GBS as by spontaneous nucleation and bulging, as was pointed out by the reviewer (Prior) of that paper. Falus et al is one of the few papers in the geoscience world that interprets weakening CPO with reduced grain size as related to a spontaneous nucleation process. There are many more papers (excluding our papers) (Cao et al., 2017; Czertowicz et al., 2016; Kaczmarek and Tommasi, 2011; Linckens et al., 2015; Ohuchi et al., 2015; Park and Jung, 2017; Skemer and Karato, 2008; Skemer et al., 2010; Warren and Hirth, 2006; Warren et al., 2008; Zhao et al., 2019) that interpret almost identical data in terms of the operation of GBS. We think the best way forward in our paper is to make sure that the factual observations are clear and to present both ways (GBS and spontaneous nucleation) that have been used in the literature to interpret similar data.

We don't think that the measurement of fewer pixels in the smaller grains makes any contribution to the weaker CPOs identified. The CPOs are weaker irrespective of whether all pixels are used or one point per grain. They are weaker if we choose a random subset of grains so that the number of "big" and "small" grains are the same.

14-2 The work of Qi et al. 2017 mentioned several times in this part concluded that "the dominant mechanism of CPO development occurs with increasing stress, from GBM, which consumes grains with low Schmid factors, at low stress, to the rotation of basal slip planes to an orientation normal to the compression axis at high stress, due to dislocation glide." I didn't find any mention of "grain size sensitive mechanism" as certified l. 25...

Such a grain size sensitive mechanism should be verified by varying grain size during the experiments and evaluate its effect on a given parameter, such as peak stress, strain-rate or so. I maintain that there is no proof of such a GSS mechanism in the experiments presented here, and therefore the interpretation should be cleared about that. That GBS is more active in smaller grains is well known since Boullier and Gueguen work! It does not mean that it should occur in the specific case here, unless otherwise proven...

We agree that rotation of slip planes is a key process in CPO evolution and hopefully our revisions make that much clearer. If GBS occurs it is additional to lattice rotations related to dislocation activity. In the work referred to (Qi et al., 2017: that involves three of the co-authors of this paper) we did not segment the data in a way that required us to bring in interpretations such as GBS, nor spontaneous nucleation. We were always of the view that GBS could be important, as that paper does show the grain size sensitivity of peak stress data. However, it was really the work published by (Craw et al., 2018) that highlighted for the first time an extreme (in that case) difference between CPOs at different grain sizes. GBS is an integral part of the interpretation in that paper and was included in (Qi et al., 2019) to explain some of the features of shear CPOs that are not easily explained by basal slip or dynamic recrystallisation.

14-3 The hypothesis that GBM being less active at low temperature, the impact of grain rotation driven by intracrystalline slip prevails is much clearer, especially since it is very coherent with the observations that the cone angle is reduced, and more orientations are found close to the vertical. This assertion is, indeed, justified by the experimental observations. This is, in fact, the main "novelty" of the presented work and should be emphasised more. Speculation about GBS tends to lessen this message, and also the interest of the good quality observations performed in this work.

We agree with this and hopefully the revised manuscript makes this clear.

15 During dynamic recrystallization, weakening is classically (see Humphreys and Haterly 2001 or 2004 for instance, Sakai et al. 2014) attributed to the reduction of hardening based on GBM and nucleation of grains, both reducing the stored strain energy associated with dislocation pile-up or dislocation structures. Therefore dynamic recrystallization induced weakening does not require the interplay of CPO or grain-size sensitive mechanism to be explained. Another point for this consideration about weakening: the relative weakening at about 20% strain is similar for every temperature cases, at about 35% (Sigma_p – Sigma_f/Sigma_p). Therefore there is not more weakening with small grains that without... It should rule out the hypothesis of a grainsensitive mechanism to explain weakening. Nucleation and GBM (each one having different relative influence depending on the temperature) are enough to explain the observed weakening, as expected from the dynamic recrystallization literature.

We agree with the reviewer that balance between GBM and nucleation can also explain the mechanical weakening and it is important to add this into the discussion. One key issue we want to be clear about is that CPO development is not necessarily the key process controlling weakening (or enhancement): an idea that seems prevalent among the ice sheet modelling community. We modified the statements in section 4.2: " '*All experiments show weakening after peak stress. Weakening is classically observed during dynamic recrystallization, and it has been attributed to a balance between GBM and nucleation of new grains (Montagnat and Duval., 2000; Sakai et al., 2014). In this study, mean and median ice grain size reduces with strain at all temperatures (Table 3, Fig. 11(a)). Grain size is commonly reduced during rock deformation in the laboratory (e.g. Pieri et al., 2001; Hansen et al., 2012) and in nature (Trimby et al., 1998; Bestmann and Prior, 2003). At smaller grain sizes the strain rate contribution of grain size sensitive (GSS) mechanisms increases or the stress required to drive a given strain rate contribution of GSS decreases.'… 'Therefore, further studies are required to quantify: (1) the contribution of nucleation and GBM to the total stress drop if the balance of GBM and nucleation is considered as the weakening mechanism; (2) The contribution of grain size insensitive, e.g. dislocation creep, and grain size sensitive processes, e.g. GBS, to the total stress drop if grain size reduction is considered as the weakening mechanism.'* "

16 Point 2: from figure 2, the steady state is not so obviously reached, unless, maybe at -10°C. Maybe the authors should be more careful about it, especially about mentioning it in the conclusion.

We have modified the statement to: "In all samples stress rises to a peak stress at ~ 1 to 4% strain and then drops to lower stresses at higher strains."

17 Point 3: regarding my previous comments concerning the evaluation of a subgrain size, I think that either the authors explain very clearly how they evaluate this subgrain size, and show that it is meaningful based on their experimental observations (that they do observe a subgrain network, although it does not appear clearly in the given figures, from which extracting a subgrain size appears relevant), or this parameter, even if used in the discussion with care, should not appear in the conclusion.

We removed WBV analyses. Instead, we added subgrain boundary analyses by highlighting subgrain boundaries at where the misorientations between neighbouring pixels are between 2° and 10° (Fig. 4(a-c), 5(a-c) and 6(a-c) in modified manuscript). Many of the subgrain boundaries appear to be straight, with some variations around the straight shape. The subgrain boundaries close to bulged grain boundaries are more curved. An interconnection of subgrain boundaries can be observed in some of the grains.

We didn't make it clear that the measurement of subgrain sizes were not based on the data of WBV, and they were based on the misorientation between adjacent pixels. Therefore, the new subgrain boundary plots corresponds to the original subgrain calculations.

We modified the point 3 to: "*All deformed samples develop distinct subgrain boundaries and show a peak at 2°-3° in neighbour-pair misorientation angle distribution. Mean/median subgrain size is smaller than mean/median grain size. These observations suggest recovery and subgrain rotation were active in all deformed samples.*"

18 Point 5: once again, this conclusion makes use of the subgrain size which measurement method is not clear, and therefore should not be used in the conclusion unless clarified.

We have removed this conclusion since description and discussion of subgrain size have been strongly reduced.

19 Point 6: I think that there is nothing really new in this point... it has been demonstrated for many materials undergoing dynamic recrystallization, and it is a direct evidence from energy considerations... Should it really come as an important conclusion? At least, the authors should be care to mentioned “as already observed”, or “as expected during dynamic recrystallization”...

We have removed boundary lobateness analyses. This is an issue for a different readership.

20 Point 7: based on my comments concerning part 4.2, the mention of GBS to explain weakening should be removed. It is also surprising that an hypothesis that is only briefly mentioned in a very short paragraph (4.2), could come to an important conclusion point...

See responses to 8-1, 8-2 and 14-2.

21 Point 8: same as point 7, and please note that weakening should be measured relatively to the peak stress value (for instance), and it therefore leads to very similar weakening for all temperature conditions (about 35%).

We have removed point 8.

21 - In general, there is a lack of references from the work done on recrystallization (on ice and other materials) by others authors than the authors’ team.... this is especially true, for instance, in part 4.1.3, and this should be corrected. In particular when other’s work do not come to similar conclusions as the authors...

We have included additional references in the modified manuscript.

22. - Maybe related to this lack of references, some assertions are given with too few justifications, that should come either from experimental observations or from previous works. This should be corrected, and the authors could specify that they are making hypotheses when there is no existing justifications.

We have added more references on concepts that are not clarified. We have specified that we are making hypotheses or interpretations wherever that is the case.

23 - This work does not contain any significant novelty, but provides more detailed and accurate observations at the microstructure scale compared to previous (old!) measurements performed by Jacka and co-authors for instance.

Compared to the extensive literature about dynamic recrystallization at hot temperature (see for instance Humphreys and Haterly 2001 or 2004), there is no novelty, and this literature should be mentioned, especially within the discussion, in order to help the interpretation of the results.

This paper include quantitative microstructural analysis of ice deformed at -20 and -30 °C to progressively higher strains. Such data have never been presented before. To our point of view, these new data are novel. See the comments in section one (General statements)

We present the opening angle evolution of the cone-shaped *c*-axis CPO between this study and previous work. This work had not been systematically done before. The summary view of observations of open-angle evolution with strain as a function of temperature (and ultimately also as a function of stress/ strain rate) is crucial as a test of hypothesis for the deformation and recrystallisation mechanisms that control ice microstructure and ice mechanics.

Last but not the least, we added more data, including misorientation analyses and quantification of repeat counted grains in 2-D using line interception method (done before) and full crystallographic data (completely new) to provide a more detailed microstructural analyses, and to support hypotheses.

24 - The high quality observations enable to assert more clearly some mechanisms as important in the case of recrystallization in ice as, for instance, the fact that at low temperature,

intracrystalline rotation will prevail on GBM and therefore induces texture that are closer to the one observed along deep ice cores.

We agree with the reviewer on this point. We hope we have done this in the modified manuscript.

25 - It is not clear, all over the text,why the authors want or need to mention GBS as an impacting mechanisms since the experiments performed show absolutely no proof of it, neither in macroscopic data (dependance of peak stress on grain size for instance), nor in microscopic observations. The only observation of small grain necklaces (but limited in number) at the lowest temperature, and a weaker texture in this small grain population is not sufficient, to my point of view, to assert the occurrence of GBS. It could be mentioned as one of the hypothesis among others, but not come to the conclusion as the mechanism at play. In particular, the use of GBS is not necessary to explain stress weakening and does not appear coherent with the results.

See responses to 8-1, 8-2 and 14-2.

26 - I raise again the point about the lack of proper explanation concerning the measurement of subgrain size in the specific case the presented experiments, since the figures shown do not reveal any proper subgrain structure that could be characterized by a dimension (as a mean size for instance). Since different conclusion are taken out of this subgrain size evaluation, it should be corrected before any publication.

We agree with the reviewer. We have provided new subgrain boundary maps and new subgrain/grain size data. We also strongly reduced data and discussion related to subgrain size.

27 - the authors make no use of their observations from the WBV method neither in the discussion, nor in the conclusion... Should it remain in the paper?

We have removed WBV analyses. We have done a whole series of quantitative Weighted Burgers vector (WBV) analyses on our EBSD data. However, we decided to pull all the WBV analyses out from this paper because we found a strong stereological effect, i.e. effects of different 2-D surfaces chosen from the same 3-D sample, on the GND statistics. Please refer to response to comment 12 for details.

References

Becroft, L., 2015, New grain growth experiments in water ice [MSc thesis: University of Otago, p132].

Bestmann, M. and Prior, D. J.: Intragranular dynamic recrystallization in naturally deformed calcite marble: diffusion accommodated grain boundary sliding as a result of subgrain rotation recrystallization, Journal of Structural Geology, 25(10), 1597–1613, https://doi.org/10.1016/s0191-8141(03)00006-3, 2003.

Cao, Y., Jung, H. and Song, S.: Olivine fabrics and tectonic evolution of fore-arc mantles: A natural perspective from the Songshugou dunite and harzburgite in the Qinling orogenic belt, central China, Geochem. Geophys. Geosyst., 18(3), 907–934, https://doi.org/10.1002/2016GC006614, 2017.

Chauve, T., Montagnat, M., Barou, F., Hidas, K., Tommasi, A. and Mainprice, D.: Investigation of nucleation processes during dynamic recrystallization of ice using cryo-EBSD, Phil. Trans. R. Soc. A, 375(2086), 20150345–20, https://doi.org/10.1098/rsta.2015.0345, 2017.

Cole, D. M.: Strain-Rate and Grain–Size Effects in Ice, Journal of Glaciology, 33(115), 274–280, https://doi.org/10.3189/S0022143000008844, 1987.

Craw, L., Qi, C., Prior, D. J., Goldsby, D. L. and Kim, D.: Mechanics and microstructure of deformed natural anisotropic ice, Journal of Structural Geology, 115, 152–166, https://doi.org/10.1016/j.jsg.2018.07.014, 2018.

Cross, A. J., Prior, D. J., Stipp, M. and Kidder, S.: The recrystallized grain size piezometer for quartz: An EBSD-based calibration, Geophysical Research Letters, 44, 6667–6674, https://doi.org/10.1002/2017gl073836, 2017a.

Czertowicz, T. A., Toy, V. G. and Scott, J. M.: Recrystallisation, phase mixing and strain localisation in peridotite during rapid extrusion of sub-arc mantle lithosphere, Journal of Structural Geology, 88(c), 1–19, https://doi.org/10.1016/j.jsg.2016.04.011, 2016.

Duval, P., Ashby, M. F. and Anderman, I.: Rate-controlling processes in the creep of polycrystalline ice, The Journal of Physical Chemistry, 87(21), 4066–4074, https://doi.org/10.1021/j100244a014, 1983.

Duval, P., Louchet, F., Weiss, J. and Montagnat, M.: On the role of long-range internal stresses on grain nucleation during dynamic discontinuous recrystallization, Materials Science & Engineering A, 546, 207–211, https://doi.org/10.1016/j.msea.2012.03.052, 2012.

Fliervoet, T. F., Drury, M. R., & Chopra, P. N: Crystallographic preferred orientations and misorientations in some olivine rocks deformed by diffusion or dislocation creep. Tectonophysics, 303, 1–27. https://doi.org/10.1016/s0040-1951(98)00250-9, 1999.

Goldsby, D. L. and Kohlstedt, D. L.: Grain boundary sliding in fine-grained ice I, Scripta Materialia, 37, 1399-1406, https://doi.org/10.1016/s1359-6462(97)00246-7, 1997.

Hansen, L. N., Zimmerman, M. E., and Kohlstedt, D. L.: The influence of microstructure on deformation of olivine in the grain-boundary sliding regime, J. Geophys. Res., 117, B09201, https://doi.org/10.1029/2012JB009305, 2012.

Hidas, K., Tommasi, A., Mainprice, D., Chauve, T., Barou, F. and Montagnat, M.: Microstructural evolution during thermal annealing of ice-Ih, Journal of Structural Geology, 99, 31–44, https://doi.org/10.1016/j.jsg.2017.05.001, 2017.

Hooke, R. L. and Hudleston, P. J.: Ice Fabrics in a Vertical Flow Plane, Barnes Ice Cap, Canada, Journal of Glaciology, 25(92), 195–214, https://doi:10.3189/S0022143000010443, 1980.

Humphreys, J. F.: Nucleation in Recrystallization, MSF, 467-470, 107–116, https://doi.org/10.4028/www.scientific.net/msf.467-470.107, 2004.

Jiang, Z., Prior, D. J. and Wheeler, J.: Albite crystallographic preferred orientation and grain misorientation distribution in a low-grade mylonite: implications for granular flow, Journal of Structural Geology, 22(11-12), 1663–1674, https://doi.org/10.1016/s0191-8141(00)00079-1, 2000.

Journaux, B., Chauve, T., Montagnat, M., Tommasi, A., Barou, F., Mainprice, D. and Gest, L.: Recrystallization processes, microstructure and crystallographic preferred orientation evolution in polycrystalline ice during high-temperature simple shear, The Cryosphere, 13(5), 1495–1511, https://doi.org/10.5194/tc-13-1495-2019, 2019.

Kaczmarek, M.-A. and Tommasi, A.: Anatomy of an extensional shear zone in the mantle, Lanzo massif, Italy, Geochem. Geophys. Geosyst., 12(8), 1-24, https://doi.org/10.1029/2011GC003627, 2011.

Kilian, R., Heilbronner, R., and Stünitz, H.: Quartz grain size reduction in a granitoid rock and the transition from dislocation to diffusion creep, Journal of Structural Geology, 33, 1265-1284, https://doi.org/10.1016/j.jsg.2011.05.004, 2011.

Kirby, S. H., Durham, W. B., Beeman, M. L., Heard, H. C. and Daley, M. A.: Inelastic properties of ice Ih at low temperatures and high pressures, J. Phys. Colloques, 48(C1), C1–227–C1–232, https://doi.org/10.1051/jphyscol:1987131, 1987.

Kuiper, E. J. N., Weikusat, I., de Bresser, J. H., Jansen, D., Pennock, G. M., and Drury, M. R.: Using a composite flow law to model deformation in the NEEM deep ice core, Greenland: Part 1 the role of grain size and grain size distribution on the deformation of Holocene and glacial ice, The Cryosphere Discuss, https://doi.org/10.5194/tc-2018-275, 2019a.

Kuiper, E. J. N., de Bresser, J. H. P., Drury, M. R., Eichler, J., Pennock, G. M. and Weikusat, I.: Using a composite flow law to model deformation in the NEEM deep ice core, Greenland: Part 2 the role of grain size and premelting on ice deformation at high homologous temperature, The Cryosphere Discussions, https://doi.org/10.5194/tc-2018-275, 2019b.

Linckens, J., Herwegh, M., & Müntener, O: Small quantity but large effect — How minor phases control strain localization in upper mantle shear zones. Tectonophysics, 643, 26–43. https://doi.org/10.1016/j.tecto.2014.12.008, 2015.

MacDonald, J. M., Wheeler, J., Harley, S. L., Mariani, E., Goodenough, K. M., Crowley, Q. and Tatham, D.: Lattice distortion in a zircon population and its effects on trace element mobility and U–Th–Pb isotope systematics: examples from the Lewisian Gneiss Complex, northwest Scotland, Contrib Mineral Petrol, 166, 21–41, https://doi.org/10.1007/s00410-013-0863-8, 2013.

Mellor, M. and Cole, D. M.: Deformation and failure of ice under constant stress or constant strain-rate, Cold Regions Science and Technology, 5(3), 201–219, https://doi.org/10.1016/0165-232x(82)90015-5, 1982.

Monz, M. E., Hudleston, P. J., Prior, D. J., Michels, Z., Fan, S.., Negrini, M., and Langhorne, P.: Electron backscatter diffraction (EBSD) based determination of crystallographic preferred orientation (CPO) in warm, coarse-grained ice: a case study, Storglaciären, Sweden, The Cryosphere Discuss, https://doi.org/10.5194/tc-2020-135, 2020.

Ohuchi, T., Kawazoe, T., Higo, Y., Funakoshi, K.-I., Suzuki, A., Kikegawa, T. and Irifune, T.: Dislocation-accommodated grain boundary sliding as the major deformation mechanism of olivine in the Earth's upper mantle, Sci. Adv., 1(9), e1500360–11, https://doi.org/10.1126/sciadv.1500360, 2015.

Park, M., and Jung, H: Microstructural evolution of the Yugu peridotites in the Gyeonggi Massif, Korea: Implications for olivine fabric transition in mantle shear zones. Tectonophysics, 709, 55–68. https://doi.org/10.1016/j.tecto.2017.04.017, 2017.

Prior, D. J., Diebold, S., Obbard, R., Daghlian, C., Goldsby, D. L., Durham, W. B. and Baker, I.: Insight into the phase transformations between ice Ih and ice II from electron backscatter diffraction data, Scripta Materialia, 66(2), 69–72, https://doi.org/10.1016/j.scriptamat.2011.09.044, 2012.

Prior, D. J., Diebold, S., Obbard, R., Daghlian, C., Goldsby, D. L., Durham, W. B. and Baker, I.: Insight into the phase transformations between ice Ih and ice II from electron backscatter diffraction data, Scripta Materialia, 66(2), 69–72, https://doi.org/10.1016/j.scriptamat.2011.09.044, 2012.

Qi, C., Goldsby, D. L. and Prior, D. J.: The down-stress transition from cluster to cone fabrics in experimentally deformed ice, Earth and Planetary Science Letters, 471, 136–147, https://doi.org/10.1016/j.epsl.2017.05.008, 2017.

Qi, C., Prior, D. J., Craw, L., Fan, S., Llorens, M.-G., Griera, A., Negrini, M., Bons, P. D. and Goldsby, D. L.: Crystallographic preferred orientations of ice deformed in direct-shear experiments at low temperatures, The Cryosphere, 13(1), 351–371, https://doi.org/10.5194/tc-2018-140-ac2, 2019.

Seidemann, M., 2017, Microstructural evolution of polycrystalline ice during non-steady state creep [PhD thesis: University of Otago, p110].

Shigematsu, N., Prior, D. J. and Wheeler, J.: First combined electron backscatter diffraction and transmission electron microscopy study of grain boundary structure of deformed quartzite, Journal of Microscopy, 224(3), 306–321, https://doi.org/10.1111/j.1365-2818.2006.01697.x, 2006.

Skemer, P. and Karato, S.-I.: Sheared lherzolite xenoliths revisited, Journal of Geophysical Research, 113(B7), 469–14, https://doi.org/10.1029/2007JB005286, 2008.

Skemer, P., Warren, J. M., Kelemen, P. B. and Hirth, G.: Microstructural and Rheological Evolution of a Mantle Shear Zone, Journal of Petrology, 51(1-2), 43–53, https://doi.org/10.1093/petrology/egp057, 2010.

Underwood, E. E., Quantitative Stereology for Microstructural Analysis, in McCall, J. L., and Mueller, W. M., eds., Microstructural Analysis: Tools and Techniques: Boston, MA, Springer US, p. 35-66, 1973.

Warren, J. M. and Hirth, G.: Grain size sensitive deformation mechanisms in naturally deformed peridotites, Earth and Planetary Science Letters, 248(1-2), 438–450, https://doi.org/10.1016/j.epsl.2006.06.006, 2006.

Warren, J. M., Hirth, G. and Kelemen, P. B.: Evolution of olivine lattice preferred orientation during simple shear in the mantle, Earth and Planetary Science Letters, 272(3-4), 501–512, https://doi.org/10.1016/j.epsl.2008.03.063, 2008.

Wheeler, J., Mariani, E., Piazolo, S., Prior, D. J., Trimby, P., and Drury, M. R.: The weighted Burgers vector: a new quantity for constraining dislocation densities and types using electron backscatter diffraction on 2-D sections through crystalline materials, Journal of microscopy, 233, 482-494, https://doi.org/10.1111/j.1365-2818.2009.03136.x, 2009.

Zhao, N., Hirth, G., Cooper, R. F., Kruckenberg, S. C. and Cukjati, J.: Low viscosity of mantle rocks linked to phase boundary sliding, Earth and Planetary Science Letters, 517, 83–94, https://doi.org/10.1016/j.epsl.2019.04.019, 2019.

Response to Reviewer 2

We thank Reviewer 2 for his thoughtful and helpful review of our paper. The comments have helped us improve the manuscript significantly. Our reply to reviewer comprises two parts: (1) some short general statements and (2) point-by-point reply to comments from reviewer. Reviewers comments are in blue type. *Extracts from our revised manuscript are in italics.*

Section one: general statements

1. This work contains data which are completely new.

We would like to thank the reviewer for one particular comment: "This paper essentially presents a nice set of experimental data…. the authors provide a detailed analysis of the microstructure of ice grains and its evolution…". We would like to emphasize that the sequence of microstructures and CPOs developed with increasing strain has not been documented before for ice deformed at cold temperatures (-20, -30 °C).

2. The reviewer suggests rejecting this paper mainly because the interpretation of grain boundary sliding (GBS).

In our view, interpretations are not usually what make a scientific good paper. New data that is factually correct and will stand the test of time make a good paper. It is likely that the interpretations will change in the future as researchers gain new data or insight. We accept that the factual observations that we present and then to infer GBS could be interpreted in different ways. In the revision, we include some alternative interpretations (including "spontaneous" nucleation) of the data, with some discussion of the merits and drawbacks of each of these interpretations. We hope that we have kept the observations and interpretations clearly separated and we have reduced the emphasis on our preferred interpretation of GBS. We have also identified some of the tests that may facilitate distinguishing these different interpretations in the future. Some more details are included in answers to specific points.

The reviewer's comments highlight that our original manuscript did not really make clear that we do interpret intracrystalline dislocation glide that causes lattice rotation as one of the key processes controlling CPO development. We hope that we have made this much clearer in the revised manuscript. The operation of a GBS process, if this is correct, would be additional to the role of intracrystalline dislocation glide and associated recovery and recrystallisation processes.

Section two: point-by-point reply to comments

1. All along the paper, the authors state that grain boundary sliding (gbs) must be invoked to explain the observations. For my point of view, there is absolutely no proof here that gbs has been activated, even in the “small grains”. The authors observe some correlations between grain size distribution, temperature, texture, but whether gbs is necessary to explain all that is another story. The evidences prone by the authors are highly speculative. Authors try to explain that gbs is necessary using arguments based on microstructure evolution. But many other parameters coming in play should be also considered, and mostly those associated with recrystallization (for which the micrographs show direct evidences unlike gbs) such as gbm rate, nucleation rate, stored energy, etc and their evolution with temperature and strain for which our actual knowledge is very limited. To prove that gbs has been active in the specimen, I would suggest the authors to (i) provide direct evidence of a sliding boundary and/or (ii) show that the associated viscosity is compatible with the one of the specimen (as gbs in a polycrystalline aggregate required associated diffusion, which is slow) and/or (iii) model microstructure evolution due to deformation + dynamic recrystallization to show that the observed evolution cannot be explained by these only mechanisms.

The key objective of this paper is to report the detailed changes in microstructures and CPOs to progressively higher strains at low and high temperatures, with the very new data being at lower temperatures. The interpretation of GBS is not central to this and we have downplayed that in the revised manuscript. We still wish to explain the weakening of CPOs in finer grain sizes and have presented two alternative interpretations; GBS and spontaneous nucleation.

We agree with reviewer’s comment that our data cannot prove the existence of grain boundary sliding. We would love to have fiducial marker evidence to show directly the GBS effect (e.g.(Eleti et al., 2020; Schmid et al., 1977; Spiers, 1979): this is a significant technical challenge for now. The particular set of experiments presented in our paper does not include variable initial grain size. However, comparable experiments do show grain size sensitivity. The set of -10 °C experiments published by Qi et al 2017 have two different initial grain sizes. A plot of strain rate against the peak stresses (Fig. 3, copied below as Fig. R2.1) shows two different best fit lines for the two initial grain sizes. At peak stress (~ equivalent to min strain rate) grain size is unlikely to have changed substantially from the starting material (and we have some new experiments to peak stress only that show this to be correct). The easiest interpretation of the Qi et al (2017) mechanical data is that there is grain size sensitivity, which is consistent with the operation of GBS.

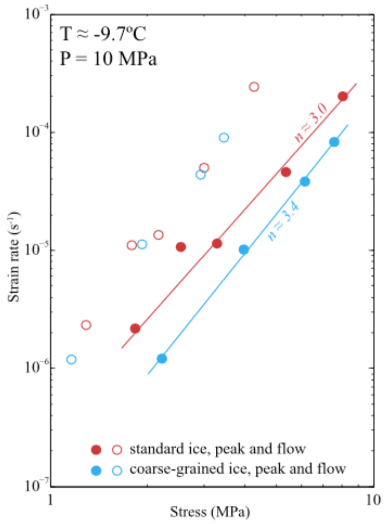

Figure R2.1. Plot of strain rate versus stress on logarithmic scales using data from Qi and others (2017).

If GBS does occur, our interpretation is that this is in addition to dislocation glide (Drury et al., 1985; Gifkins, 1976, 1977; Goldsby and Kohlstedt, 1997, 2001; Hirth, 2002; Hirth and Kohlstedt, 2003; Kuiper et al., 2019a; Kuiper et al., 2019b; Langdon, 2006, 2009; Warren and Hirth, 2006). Some authors term this dislocation accommodated GBS or “disGBS”. In this mechanism, the total strain rate is the addition of a dislocation process (that changes crystal shapes and causes lattice rotation and internal distortion) and a GBS process that is probably controlled by a “viscous” mechanism within grain boundaries (small path length diffusion and/or asperity plasticity: idea originally from (Gifkins, 1976)). This is not the same as diffusion creep, irrespective of whether that is controlled by lattice diffusion (Nabarro-Herring creep) or grain boundary diffusion (Coble creep). GBS is required as an accompanying mechanism to polycrystalline diffusion creep, but in that case grain shape change is facilitated by the diffusive mass transfer process. In diffusion creep, grain size sensitivity comes primarily from the increased path length for diffusion meaning that the change of shape of bigger grains takes longer. In “disGBS” the GBS itself is the prime source of grain size sensitivity. If there is a “viscous” grain boundary volume then the rheology will depend on the volume proportion of the sample that comprises grain boundaries: this proportion will increase with decreasing grain size.

CPO models certainly do not match observations fully for shear (see discussion in Qi et al., 2019) and that paper speculates that GBS may bridge the gap between the results of laboratory experiments and numerical models. Indeed, there is currently a major effort (led by Sandra Piazolo and colleagues) among the community that use the ELLE modelling platform to incorporate GBS: a difficult task. Microstructural modelling is beyond the scope of our paper.

2. The mechanical tests (figure 2) essentially show a dominant temperature effect (known since the early years of glaciology – do the associated activation energy, not calculated here, matches literature data ?) and a softening at strain larger than ~0.03.

Yes, the mechanical data match literature data. We have added a calculation of activation energy to the supplementary information and have referred to this in the text. Best fit to all data (-10, -20 and -30 °C) give activation enthalpies of 98 kJ/mol and 103 kJ/mol from peak and final stress data assuming n=3 and 131 kJ/mol and 138 kJ/mol from peak and flow stress data assuming n=4. These values are close to reported Q values of 71-124 kJ/mol (-5 °C- -30 °C) from Budd and Jacka (1989) and ~133 kJ/mol (-1.5 °C- -12.8 °C) from Glen (1955) and 64-250 kJ/mol from Kuiper and others (2019a, 2019b). Note experiments in this study only cover three temperature values. Hence, the calculated Q values are prone to error. More data points are needed for a more accurate Q investigation.

3. Along the same line, the sentence (p12 line 2) “gbs is kinematically required for all grain size sensitive mechanisms” is incorrect. For example, the Hall-Petch mechanism is largely used in metallurgy to explain size effect observed in many nanometric grains metallic alloys. Hall-Petch is based on the mean free path of dislocations, it explain very well many observations, and does not require any other mechanisms than dislocation glide (no gbs!). Could the mean free path of mobile dislocations have an influence of ice rheology at low temperature ?

Our apologies; the reviewer is correct. That statement does not apply to the full breadth of GSS mechanisms including classic Hall-Petch and also mechanical twinning (Rowe and Rutter, 1990) and we have removed the statement.

As an aside there is a very interesting ongoing discussion of the Hall-Petch (Weertman, 1993) relationship (with strength increasing with grain size) and the inverse Hall-Petch relationship (Masumura et al., 1998) in the materials science literature (Pande and Cooper, 2009; Ryou et al., 2018; Sheinerman et al., 2020). Modelling of the inverse Hall-Petch relationship requires coupling of GBS to intragranular dislocation activity (Carlton and Ferreira, 2007; Ehre and Chaim, 2008; Padmanabhan et al., 2007; Padmanabhan et al., 2014; Ryou et al., 2018; Sheinerman et al., 2020) and the relationships are not very different to those described elsewhere as GBS accommodated by dislocation creep (Goldsby and Kohlstedt, 1997; Hansen et al., 2011; Langdon, 2006, 2009). In minerals, the normal Hall-Petch relationship (increasing strength with decreasing grain size) has only been documented at low homologous temperatures (Hansen et al., 2019; Koizumi et al., 2020) whereas weakening with reduced grain size is the norm at higher temperatures and lower stresses (Brodie and Rutter, 2000; De Bresser et al., 2001; Hiraga et al., 2013; Hirth, 2002; Hirth and Kohlstedt, 2003; Schmid et al., 1977; Ter Heege et al., 2005; Walker et al., 1990). Materials science work defines a material-dependent threshold grain size, above which the Hall-Petch relationship holds and with the inverse Hall-Petch relationship at grain sizes below the threshold (Pande and Cooper, 2009; Ryou et al., 2018). Recent work suggests that the threshold moves to larger grain sizes at lower strain-rates or stresses (Somekawa and Mukai, 2015). The rates that are considered very slow in these metallurgical analysis (e.g. 1 x 10^{-4} s^{-1}) are very fast in the context of geological or glaciological laboratory experiments and this may explain why we only see evidence of the Hall-Petch effect at low homologous T. Some recent work relates GBS associated with the inverse Hall-Petch relationship with amorphization of the grain boundaries (Guo et al., 2018) and a molecular dynamics modelling study of ice (Cao et al., 2018) generates an inverse Hall-Petch relationship that involves a combination of GBS, grain rotation, amorphization and recrystallization, phase transformation, and dislocation nucleation in both bicrystals and polycrystals.

4. Similarly, about the sentence (p15 line 6) “similarly, we suggest that grain size sensitivity of gbs favours a faster strain rate in small grains”: I find no fact in the results supporting this assertion. Strain-rate in various sets of grains is not measured nor estimated here. And also, in section 4.2, the authors make a correlation between the softening observed at -30degC and the grain size, and conclude that the observed softening should likely be attributed to gbs. Gbs could be a possibility, but among many others. For example, what do we know about the density of mobile dislocations ?? If it increases, the stress would decreases as observed. Increase of dislocation density is often used to explain the peak stress for materials with low initial dislocation density (eg. Si, . . .).

Please see our answer to point 1.

5. The statistical relevance of the performed mechanical tests and/or microstructural investigations can also be questioned. Figures 9, 10, 11, 13 show pole figures that do not, by far, exhibit the expected transverse isotropy (expected since the initial specimen are thought to exhibit random CPO with equiaxe grain shape, and since uniaxial compression is transverse isotropic). This severe lack of symmetry in the observed microstructure can originate from (i) initial samples that do not exhibit a random microstructure and/or (ii) mechanical tests that deviate from uniaxial compression (there could be many reasons for that) and/or (iii) the microstructure is not analysed on a sufficiently large material volume (volume smaller than the Representative Volume Element-RVE). Consequently, the global picture shown here (ex. texture strength as function of temperature, which is an interesting result) are probably correct, but I don’t think that, with the results shown, authors can dig deeper into the interpretation of active deformation mechanisms. If the lack of texture symmetry is present in the specimens,

then the applied axial strain-rate would generate significant shear stress (or shear-rate, depending on the experimental boundary conditions), affecting of course the texture and microstructure evolutions (so-called out-of-axis tests). Is there any connection with the large spread observed on the mechanical responses (figure 2) ? For example the peak stress at -10 C varies by almost a factor 2, which is considerable and should be discussed. One could expect some associated spread in the microstructure.

The reviewer is correct about symmetric incompleteness and we have added the following text to address this: *"Many deformed samples exhibit an incompleteness of c-axes cone (lack of cylindrical symmetry) (Fig. 8-10). The incompleteness of c-axes cone is more severe for 5 μm EBSD maps collected from a much smaller area than 30 μm EBSD maps (Fig. 12). These phenomena are common to all ice CPOs from measurements on a single sample planes (by EBSD or optical methods: see any of the papers cited), but are not so apparent in neutron diffraction data (Piazolo et al., 2013; Wilson et al., 2019), that sample a larger volume, suggesting that a single plane through a deformed sample does not generally contain sufficient grains for a fully representative CPO."*

The fact that neutron diffraction data gives CPOs that have close to the cylindrical symmetry, for samples that have fewer grains (initially) in an average cross section (Piazolo et al 2013 initial grain size 0.5mm whereas ours <0.3mm: samples in both cases 1 inch diameter) suggests that the sample as a whole has enough grains to b considered mechanically isotropic. In this case the incompleteness of CPOs is an analytical sampling issue and should not impact on mechanical data. A good example of where samples contain too few grains to be considered isotropic is the re-deformation of natural ice with a 20mm grain size (Craw et al., 2018): this gives rise to significant inconsistency in stress strain curves, although yield stress data correlate sensibly with strain rates.

The scatter of peak stress values we have is fairly typical of confined medium constant displacement rate experiments (data for comparison can be extracted from (Durham et al., 1983; Golding et al., 2020). Unconfined constant displacement rate experiments (Hammonds and Baker, 2016; Vaughan et al., 2017) have less variability and it is likely that some of the scatter in confined medium experiments relates to how stable the confining pressure is. Unconfined creep experiments (constant load) also show a range of minimum strain rates for a set of experiments at the same stress (Journaux et al., 2019; Montagnat et al., 2015; Treverrow et al., 2012). To compare constant rate vs constant load experiments, we can calculate the "viscosity" at peak stress/ minimum strain rate. Confined constant rate and unconfined creep tests both have "viscosities" that vary by up to about 2x for experiments at the same rate or stress. Unconfined constant rate experiments have peak stress "viscosities" that vary by up to about 1.1x. These statements are made on a relatively small data set as there seem to be few "repeat" experiments (in terms of load or rate) in the published literature. At the moment we don't have a full explanation as to what controls this variability. We have to account for the variability in studies where it becomes important (e.g. for calibrating flow laws). In this paper it is not so important and the aspect that is important to us – the curve shape with a peak stress followed by weakening is common to all experiments.

6. The discussion in this paper relies on a separation of the grain size distribution between "small grains" and "large grains", invoking a "bimodal" (p7 line 4) grain size distribution. In figures 3, 4, 5, I do not see any bimodal grain size distribution, but rather a unimodal one with a long tail. Therefore the size threshold (p7 line 16) used to separate small and large grains is completely ad hoc, and I am not sure about the effect of this particular choice on the provided discussion. I also don't understand why the authors state that "The small grains are likely

include all the recrystallized grains" (p7 line 19, p8 line 8, . . .) as (i) if GBM occurs, recrystallization can also lead to large grains and (ii) the grain size distribution of the initial microstructure is not shown.

(1) We modified the description of grain size distribution in section 3.3.2: *"For samples deformed to ~3% strain, the grain size distributions are strongly skewed or possibly bimodal, with a clear main peak at finer grain sizes and a tail of coarser sizes with a broad, poorly defined secondary peak corresponding to the mean grain size of the starting material (Fig. 4(d), 5(d) and 6(d))."*

(2) We removed the statement of: "The small grains are likely include all the recrystallized grains." This is a very good point from the reviewer. We (who come from the rock deformation world) sometimes forget that at the high homologous temperatures in ice recrystallised grains can grow to a large size. In much lower homologous temperature experiments in quartz, for example, it is reasonable that recrystallised grains are small and remnant grains large (see for example (Cross et al., 2017; Hirth and Tullis, 1992). We still wish to segment the grain size on the basis of "big" and "small" grains and we hope that our presentation of this is now more robust and does not assign arbitrarily the status recrystallised or remnant on certain grain size populations. The precise threshold we use does not influence the difference in CPOs between "big" and "small" grains as shown in Fig. R2.2, extracted from new supplementary information.

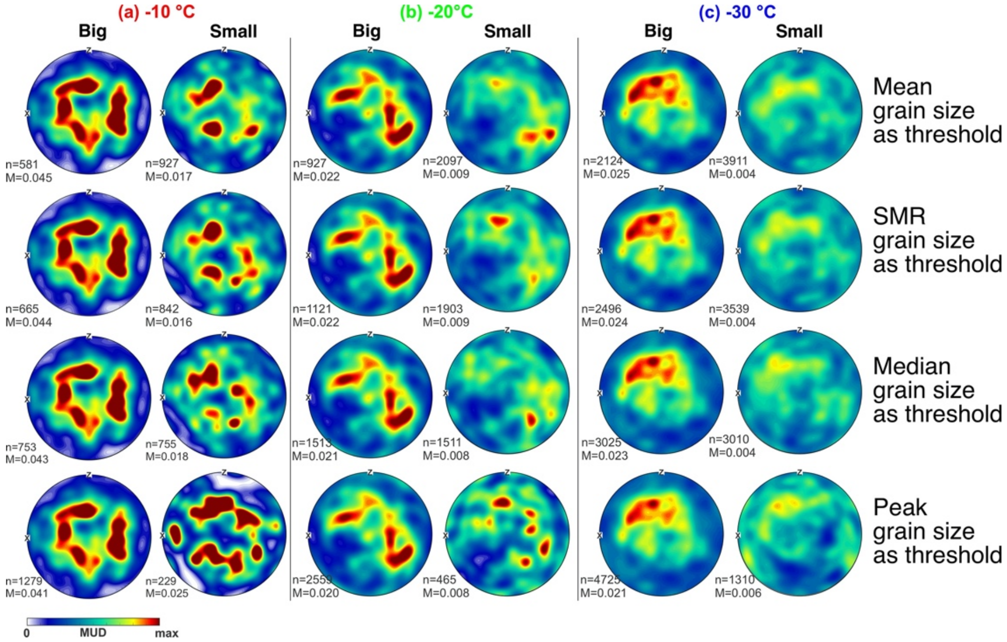

Figure R2.2. The contoured *c*-axis CPOs of "big" and "small" grains in samples deformed at **(a)** -10, **(b)** -20 and **(c)** -30 °C to ~12% strain. "Big" and "small" grains are separated using the threshold of mean grain size (row 1), SMR (square mean root) grain size (row 2), median grain size (row 3) and peak grain size (row 4). Number of grains and M-index value are marked at the bottom left corner of the corresponding *c*-axis CPO.

7. The discussion also largely relies of the size of subgrains. However, in figures 3, 4, 5, it is really hard to identify those subgrains in most of the grains. For example in figure 5 at 20% strain, one only sees some disconnected segments in the WBV map in the large yellow or pink-orange grains at the bottom of the micrograph. How do the authors identity the subgrains and calculate their size in such a case ?

We agree with the observation from the reviewer that suggests many of the subgrain boundaries are straight tilt bands or kink bands. The subgrain structure was revealed by Weighted Burgers vector (WBV) method, which picks up pixels with the WBV magnitude (||**WBV**||) higher than 0.0026 μm^{-1} (equivalent to misorientation angle between neighbouring pixels higher than ~0.7°). Therefore, many of the subgrain boundaries lower than 2° were selected and they might contain non-neglectable errors (Prior, 1999). Moreover, we didn't make it clear that the measurement of subgrain sizes were not based on the data of WBV, and they were based on the misorientation between adjacent pixels. Therefore, the new subgrain boundary plots corresponds to the original subgrain calculations. We kept the WBV analyses based on the thinking that they might contain more information for further comparison. But the WBV analyses have now been removed completely from this paper.

The new maps (Fig. 4(c), 5(c), 6(c)) that show subgrain boundaries correspond to the much simpler misorientation threshold. We modified statements on section 3.3.1 to: "Distinct subgrain boundaries can be observed in all the samples (Fig. 4 (c), 5 (c) and 6 (c)). Many of the subgrain boundaries appear to be straight, some with slight curvature. A small number have strong curvature. Interconnected subgrain boundaries can be observed in some of the grains. Subgrain boundaries subdivide grains into subgrains."

8. This experimental study cannot be used without very special care to infer deformation mechanisms occuring in "terrestrial and planetary ice flow" (1st abstract line), as (i) the grain size investigated (~200 microns) is one order of magnitude smaller than the natural one, and (ii) the strain-rate used during the mechanical tests (10-5s-1) is 3 to 6 orders of magnitude larger than in cold regions of ice sheets.

We modified the first line in abstract to: "To understand better the ice deformation mechanisms…" The reviewer raises the key problem that we struggle with, when we are working in the laboratory with application to natural ice. The absolute fastest documented natural terrestrial strain rates are in lateral shear margins ~ 10^{-9} s^{-1} (Bindschadler et al., 1996; Jackson and Kamb, 1997). Rates in basal ice is harder to estimate; most models would have strain rate maxima also around ~ 10^{-9} s^{-1}. Most parts of ice sheets and glaciers have strain rates that are up to 2 orders of magnitude slower than this. To run an experiment from to 10% strain (i.e something that may go from isotropic starting material to a "steady state" microstructure) will take three years at ~ 10^{-9} s^{-1}. (Jacka and LI, 2000) did an amazing job running experiments for long durations at low rates (down to 4 x 10^{-10} s^{-1}) but these are really the only experiments that achieve substantial strain at "natural" rates. Specific aspects of ice mechanics have been assessed by deforming natural samples to small strains (<1%) in the lab at relatively slow rates (10^{-10} s^{-1} to 10^{-8} s^{-1}) (Castelnau et al., 1998; DahlJensen et al., 1997; Jackson and Kamb, 1997). In general, it is virtually impossible to work at natural rates and we have to develop scaling relationships that involve strain rate, temperature and grain size.

9. I wonder whether there is no damage occurring at the high strain-rate considered, particularly at the smaller temperatures?

Stress-strain curves of all experimental runs show a smooth and continuous increase of stress as a function of strain before reaching the peak (Fig. 3). The stress-strain curves of experiments with a development of cracking during deformation normally show an initial yield point before reaching the peak stress (Mellor and Cole, 1982). The initial yield point is interpreted as a reflection of cracking on the mechanical data (Mellor and Cole, 1982). Such yield point is not observed in any of the experiments in this study.

The chief purpose of the confining pressure in these experiments is to suppress brittle phenomena including cracking and frictional sliding. Fig. R2.4 shows the experiment with the highest differential stress, plotted on a Mohr diagram for stress. The green circle shows the shear and normal stresses for surfaces of all orientations and the maximum (σ_1) and minimum ($\sigma_3 = \sigma_2$ = confining pressure) plot along the line of zero shear stress. Superposed are two failure envelopes. One is a Coulomb (frictional sliding) envelope using the friction coefficient for ice-ice sliding from (McCarthy et al., 2017). Coulomb envelopes usually underestimate brittle strength. The second failure envelope is the composite envelope from (Beeman et al., 1988). Red and blue Mohr circles show the stress states needed for brittle failure at 20MPa pressure with each of these envelopes. Maximum differential stresses applied in our experiments are substantially below those for needed for brittle failure.

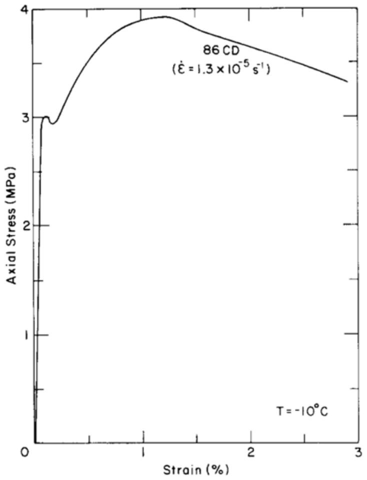

Figure R2.3. Typical stress-strain curve for deformed sample with cracking (from Mellor and Cole, 1982)

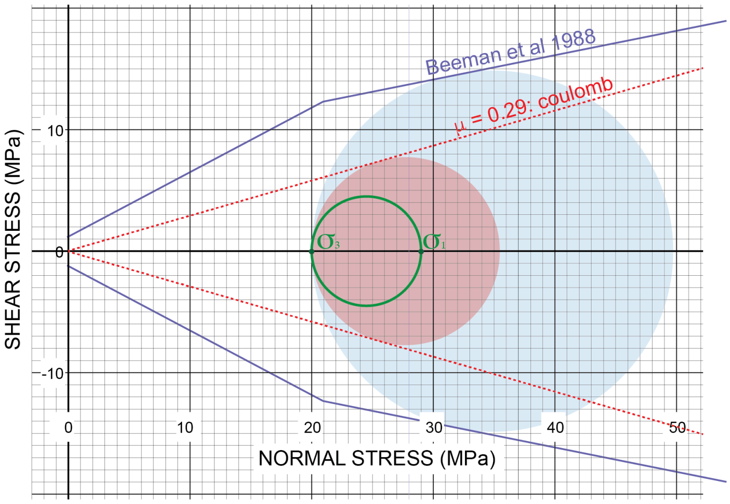

Figure R2.4. Mohr diagram showing stress state of sample PIL164 (the largest differential stress) in green. A coulomb failure envelope using a friction coefficient of 0.29 from (McCarthy et al., 2017) is shown with a red dashed line and the Mohr circle for failure at 20MPa confining pressure is shown in red. The blue lines show the (Beeman et al., 1988) failure envelope from and the Mohr circle for failure at 20MPa confining pressure is shown in blue.

10. p1 line 16 : "displacement rate" instead of "displacement"

Corrected.

11. p1 line 26 : invoking creep stages (secondary, tertiary) for the description of constant strain-rate experiments is misleading.

We have deleted these misleading wording.

12. P5 line 26, I don't understand what is meant with "The CPO data were contoured with half-width of 7.5deg" ?

We modified the statement in section 2.5.2: "The CPO data were contoured with a half-width of 7.5° based on the maximum of multiples of a uniform distribution (MUD) of the points, to more clearly show the CPO patterns."

12. p7 line 26 : to the best of my knowledge, recovery, subgrain rotation and gbm are not deformation mechanisms ! If recovery and/or gbm are initiated, the specimen will not deform.

Thank appreciate the reviewer for pointing out this mistake. We have removed this sentence since we removed boundary hierarchy analyses.

13. eq. 3, how is R (grain radius) estimated for non-spherical grains ??

We have removed grain boundary lobateness analyses.

14. p9, line 1 : I think that calling "m" the 10-10 direction is not standard (m-axes pole figures). Should be clarified ?

We corrected "*m*-axes" to "poles to the *m*-planes".

15. p11 line 26, the sentence "Much of the stress increase prior to peak stress relates to elastic strain" is wrong. First of all, there is no known yield stress for the high temperature rheology of ice, i.e. plastic strain starts as soon any stress is applied, as here in the first part of the loading prior to the peak stress. There are old published data (on single and polycrystals) showing that the initial slope depends on the strain-rate. Of course, there is always an elastic strain associated to the applied stress (Hooke's law). On top of that, the measured slope (~1GPa) very probably also accounts for the way strain is measured experimentally: if it is not measured directly on the specimen (eg. with an extensometer or strain-gage), it is well known that very small modulus are obtained, due to machine rigidity and other artefacts.

intracrystalline dislocation slip, the porosity loss being very likely negligible.

Published literature labelled the stress increase prior to peak stress in constant displacement rate experiments as: "normally elastic" (Cole, 1987) and "quasi-elastic" (Kirby, 1987). The deceleration during primary creep in constant stress experiments was interpreted as effected by a "delayed elasticity", with a recoverable component of time-dependent elastic strain and an irrecoverable viscous strain (Mellor and Cole, 1982), and "anelasticity" (Duval et al., 1983). The reason we chose to describe the behaviour as substantially elastic is that we have other experiments where we can show that this part of the deformation is recoverable. However, these other experiments are higher rate experiments with slopes on the stress strain curve approaching the 9GPa modulus. The reviewers are correct in pointing out that in the experiments presented in this paper the slope is substantially below modulus and the behaviour is not substantially elastic. We have modified the statement in section 4.1.1: "*This likely includes anelastic deformation related to intergranular stress redistribution used to explain primary creep in constant load experiments (Duval et al, 1983). The curvature of the stress strain line at the start of each experiment may relate to initial porosity loss as suggested by rapid increases in ultrasonic p-wave velocity in comparable experiments by Vaughan et al., (2017).*"

17. figures 3, 4, 5 : If I understand (this is not clear in the paper), the shown grain size distributions indicate the number of grains at a given size. It would be more instructive to show the volume fraction, not the number of grains, as the rheology is associated with the volume average of grain deformation.

Grain size distribution has been used to show generation of small grains after deformation. These grains are not observed in undeformed grains. We estimated grain volume for each grain size class for modelling the effect of small grains on mechanical weakening. These grain volume data are subject to another paper.

18. figure 14 is interesting, as it shows that the strain-rate seems to have little effect. To my understanding, this is not expected for thermally activated mechanisms such as recrystallization, where time comes in plays. This figure could be more largely discussed, to my point of view.

We plotted data from this study and previous studies in a diagram of θ as a function of strain with data subdivided with different temperatures and strain rates to increase our understanding of the processes that might control the c-axes cone opening-angle (Table 4 and Fig. 13). The relation to strain rate within the broader data set in this figure is not very clear, because for any given temperature there is not a big range in strain rate. The exception is the data set plotted from (Qi et al., 2017) at -10 °C and ~ 20% strain which does show a rough decrease in θ as strain rate (or stress) increases (See Qi et al., 2017 fig 9. This fits with the Zener-Hollomon concept (Zener and Hollomon, 1944) that suggests that decreasing strain rate will have an equivalent effect to increasing temperature.

References

Beeman, M., Durham, W. B. and Kirby, S. H.: Friction of ice, Journal of Geophysical Research: Solid Earth, 93(B7), 7625–7633, https://doi.org/10.1029/JB093iB07p07625, 1988.

Bindschadler, R., Vornberger, P., Blankenship, D., Scambos, T. and Jacobel, R.: Surface velocity and mass balance of Ice Streams D and E, West Antarctica, Journal of Glaciology, 42(142), 461–475, https://doi.org/10.3189/S0022143000003452, 1996.

Brodie, K. H. and Rutter, E. H.: Deformation mechanisms and rheology: why marble is weaker than quartzite, Journal of the Geological Society, 157(6), 1093–1096, https://doi.org/10.1144/jgs.157.6.1093, 2000.

Budd, W. F. and Jacka, T. H.: A review of ice rheology for ice sheet modelling, Cold Regions Science and Technology, 16, 107–144, https://doi.org/10.1016/0165-232x(89)90014-1, 1989.

Cao, P., Wu, J., Zhang, Z., Fang, B., Peng, L., Li, T., Vlugt, T. J. H. and Ning, F.: Mechanical properties of bi- and poly-crystalline ice, AIP Advances, 8(12), 125108–23, https://doi.org/10.1063/1.5042725, 2018.

Carlton, C. E. and Ferreira, P. J.: What is behind the inverse Hall–Petch effect in nanocrystalline materials? Acta Materialia, 55(11), 3749–3756, https://doi.org/10.1016/j.actamat.2007.02.021, 2007.

Castelnau, O., Shoji, H., Mangeney, A., Milsch, H., Duval, P., Miyamoto, A., Kawada, K. and Watanabe, O.: Anisotropic behavior of GRIP ices and flow in Central Greenland, Earth and Planetary Science Letters, 154(1-4), 307–322, https://doi.org/10.1016/s0012-821x(97)00193-3, 1998.

Cole, D. M.: Strain-Rate and Grain–Size Effects in Ice, Journal of Glaciology, 33(115), 274–280, https://doi:10.3189/S0022143000008844, 1987.

Craw, L., Qi, C., Prior, D. J., Goldsby, D. L. and Kim, D.: Mechanics and microstructure of deformed natural anisotropic ice, Journal of Structural Geology, 115, 152–166, https://doi.org/10.1016/j.jsg.2018.07.014, 2018.

Cross, A. J., Prior, D. J., Stipp, M. and Kidder, S.: The recrystallized grain size piezometer for quartz: An EBSD-based calibration, Geophysical Research Letters, 44(13), 6667–6674, https://doi.org/10.1002/2017gl073836, 2017.

De Bresser, J., Heege, Ter, J. and Spiers, C.: Grain size reduction by dynamic recrystallization: can it result in major rheological weakening? Int J Earth Sci, 90(1), 28–45, https://doi.org/10.1007/s005310000149, 2001.

Drury, M. R., Humphreys, F. J. and White, S. H.: Large strain deformation studies using polycrystalline magnesium as a rock analogue. Part, Physics of the Earth and Planetary Interiors, 40(3), 208–222, https://doi.org/10.1016/0031-9201(85)90131-1, 1985.

Durham, W. B., Heard, H. C. and Kirby, S. H.: Experimental deformation of polycrystalline H2O ice at high pressure and low temperature: Preliminary results, Journal of Geophysical Research, 88(S01), B377–B392, https://doi.org/10.1029/JB088iS01p0B377, 1983.

Duval, P., Ashby, M. F. and Anderman, I.: Rate-controlling processes in the creep of polycrystalline ice, The Journal of Physical Chemistry, 87(21), 4066–4074, https://doi.org/10.1021/j100244a014, 1983.

Ehre, D. and Chaim, R.: Abnormal Hall–Petch behavior in nanocrystalline MgO ceramic, J Mater Sci, 43(18), 6139–6143, https://doi.org/10.1007/s10853-008-2936-z, 2008.

Eleti, R. R., Chokshi, A. H., Shibata, A. and Tsuji, N.: Unique high-temperature deformation dominated by grain boundary sliding in heterogeneous necklace structure formed by dynamic recrystallization in HfNbTaTiZr BCC refractory high entropy alloy, Acta Materialia, 183, 64–77, https://doi.org/10.1016/j.actamat.2019.11.001, 2020.

Gifkins, R. C.: Grain-boundary sliding and its accommodation during creep and superplasticity, MTA, 7(8), 1225–1232, https://doi.org/10.1007/BF02656607, 1976.

Gifkins, R. C.: The effect of grain size and stress upon grain-boundary sliding, MTA, 8(10), 1507–1516, https://doi.org/10.1007/bf02644853, 1977.

Glen, J. W.: The creep of polycrystalline ice. Proceedings of the Royal Society of London. Series A. Mathematical and Physical Sciences, 228, 519-538, https://doi.org/10.1098/rspa.1955.0066, 1955.

Golding, N., Durham, W. B., Prior, D. J. and Stern, L. A.: Plastic faulting in ice, Journal of Geophysical Research: Solid Earth, 1–45, https://doi.org/10.1029/2019JB018749, 2020.

Goldsby, D. L. and Kohlstedt, D. L.: Grain boundary sliding in fine-grained ice I, Scripta Materialia, 37(9), 1399–1406, https://doi.org/10.1016/s1359-6462(97)00246-7, 1997.

Goldsby, D. L. and Kohlstedt, D. L.: Superplastic deformation of ice: Experimental observations, Journal of Geophysical Research: Solid Earth, 106(B6), 11017–11030, https://doi.org/10.1029/2000JB900336, 2001.

Guo, D., Song, S., Luo, R., Goddard, W. A., III, Chen, M., Reddy, K. M. and An, Q.: Grain Boundary Sliding and Amorphization are Responsible for the Reverse Hall-Petch Relation in Superhard Nanocrystalline Boron Carbide, Phys. Rev. Lett., 121(14), 145504, https://doi.org/10.1103/PhysRevLett.121.145504, 2018.

Hammonds, K. and Baker, I.: The effects of Ca ++on the strength of polycrystalline ice, Journal of Glaciology, 62(235), 954–962, https://doi.org/10.1017/jog.2016.84, 2016.

Hansen, L. N., Zimmerman, M. E. and Kohlstedt, D. L.: Grain boundary sliding in San Carlos olivine: Flow law parameters and crystallographic-preferred orientation, Journal of Geophysical Research, 116(B8), 149–16, https://doi.org/10.1029/2011jb008220, 2011.

Hansen, L. N., Kumamoto, K. M., Thom, C. A., Wallis, D., Durham, W. B., Goldsby, D. L., Breithaupt, T., Meyers, C. D. and Kohlstedt, D. L.: Low ‐ Temperature Plasticity in Olivine: Grain Size, Strain Hardening, and the Strength of the Lithosphere, Journal of Geophysical Research: Solid Earth, 124(6), 5427–5449, https://doi.org/10.1029/2018JB016736, 2019.

Hiraga, T., Miyazaki, T., Yoshida, H. and Zimmerman, M. E.: Comparison of microstructures in superplastically deformed synthetic materials and natural mylonites: Mineral aggregation via grain boundary sliding, Geology, 41(9), 959–962, https://doi.org/10.1130/g34407.1, 2013.

Hirth, G. and Tullis, J.: Dislocation regimes in quartz aggregates, Journal of Structural Geology, 14(2), 145–159, https://doi.org/10.1016/0191-8141(92)90053-y, 1992.

Hirth, G.: Laboratory Constraints on the Rheology of the Upper Mantle, in Plastic Deformation of Minerals and Rocks, edited by S.-I. Karato and H.-R. Wenk, pp. 97–120, De Gruyter, Berlin, Boston. 2002.

Hirth, G. and Kohlstedt, D.: Rheology of the upper mantle and the mantle wedge: A view from the experimentalists, in Inside the Subduction Factory, vol. 138, pp. 83–105, American Geophysical Union, Washington, D. C., 2003.

Jacka, T. H. and Jun, L.: Flow rates and crystal orientation fabrics in compression of polycrystalline ice at low temperatures and stresses, Physics of Ice Core Records, 83–102 [online] Available from: http://hdl.handle.net/2115/32463, 2000.

Jackson, M. and Kamb, B.: The marginal shear stress of Ice Stream B, West Antarctica, Journal of Glaciology, 43(145), 415–426, https://doi.org/10.3189/S0022143000035000, 1997.

Jensen, D. D., Thorsteinsson, T., Alley, R. and Shoji, H.: Flow properties of the ice from the Greenland Ice Core Project ice core: The reason for folds? Journal of Geophysical Research: Solid Earth, 102(C12), 26831–26840, https://doi.org/10.1029/97JC01266, 1997.

Journaux, B., Chauve, T., Montagnat, M., Tommasi, A., Barou, F., Mainprice, D. and Gest, L.: Recrystallization processes, microstructure and crystallographic preferred orientation evolution in polycrystalline ice during high-temperature simple shear, The Cryosphere, 13(5), 1495–1511, https://doi.org/10.5194/tc-13-1495-2019, 2019.

Kirby, S. H., Durham, W. B., Beeman, M. L., Heard, H. C. and Daley, M. A.: Inelastic properties of ice Ih at low temperatures and high pressures, J. Phys. Colloques, 48(C1), C1–227–C1–232, https://doi.org/10.1051/jphyscol:1987131, 1987.

Koizumi, S., Hiraga, T. and Suzuki, T. S.: Vickers indentation tests on olivine: size effects, Physics and Chemistry of Minerals, 47(2), 1–14, https://doi.org/10.1007/s00269-019-01075-5, 2020.

Kuiper, E. J. N., Weikusat, I., de Bresser, J. H., Jansen, D., Pennock, G. M., and Drury, M. R.: Using a composite flow law to model deformation in the NEEM deep ice core, Greenland: Part 1 the role of grain size and grain size distribution on the deformation of Holocene and glacial ice, The Cryosphere Discuss, https://doi.org/10.5194/tc-2018-275, 2019a.

Kuiper, E. J. N., de Bresser, J. H. P., Drury, M. R., Eichler, J., Pennock, G. M. and Weikusat, I.: Using a composite flow law to model deformation in the NEEM deep ice core, Greenland: Part 2 the role of grain size and premelting on ice deformation at high homologous temperature, The Cryosphere Discussions, https://doi:10.5194/tc-2018-275, 2019b.

Langdon, T. G.: Grain boundary sliding revisited: Developments in sliding over four decades, J Mater Sci, 41(3), 597–609, https://doi.org/10.1007/s10853-006-6476-0, 2006.

Langdon, T. G.: Seventy-five years of superplasticity: historic developments and new opportunities, J Mater Sci, 44(22), 5998–6010, https://doi.org/10.1007/s10853-009-3780-5, 2009.

Masumura, R. A., Hazzledine, P. M. and Pande, C. S.: Yield stress of fine grained materials, Acta Materialia, 46(13), 4527–4534, https://doi.org/10.1016/s1359-6454(98)00150-5, 1998.

McCarthy, C., Savage, H. and Nettles, M.: Temperature dependence of ice-on-rock friction at realistic glacier conditions, Phil. Trans. R. Soc. A, 375(2086), 20150348–20150348, https://doi.org/10.1098/rsta.2015.0348, 2017.

Mellor, M. and Cole, D. M.: Deformation and failure of ice under constant stress or constant strain-rate, Cold Regions Science and Technology, 5(3), 201–219, https://doi.org/10.1016/0165-232x(82)90015-5, 1982.

Mellor, M. and Cole, D. M.: Stress/strain/time relations for ice under uniaxial compression, Cold Regions Science and Technology, 6(3), 207–230, https://doi.org/10.1016/0165-232x(83)90043-5, 1983.

Montagnat, M., Chauve, T., Barou, F., Tommasi, A., Beausir, B. and Fressengeas, C.: Analysis of dynamic recrystallization of ice from EBSD orientation mapping, Front. Earth Sci., 3, 411–13, https://doi.org/10.3389/feart.2015.00081, 2015.

Padmanabhan, K. A., Dinda, G. P., Hahn, H. and Gleiter, H.: Inverse Hall–Petch effect and grain boundary sliding controlled flow in nanocrystalline materials, Materials Science & Engineering A, 452-453, 462–468, https://doi.org/10.1016/j.msea.2006.10.084, 2007.

Padmanabhan, K. A., Sripathi, S., Hahn, H. and Gleiter, H.: Inverse Hall–Petch effect in quasi- and nanocrystalline materials, Materials Letters, 133(C), 151–154, https://doi.org/10.1016/j.matlet.2014.06.153, 2014.

Pande, C. S. and Cooper, K. P.: Nanomechanics of Hall–Petch relationship in nanocrystalline materials, Progress in Materials Science, 54(6), 689–706, https://doi.org/10.1016/j.pmatsci.2009.03.008, 2009.

Prior, D. J.: Problems in determining the misorientation axes, for small angular misorientations, using electron backscatter diffraction in the SEM, Journal of Microscopy, 195(3), 217–225, https://doi:10.1046/j.1365-2818.1999.00572.x, 1999.

Qi, C., Goldsby, D. L. and Prior, D. J.: The down-stress transition from cluster to cone fabrics in experimentally deformed ice, Earth and Planetary Science Letters, 471, 136–147, https://doi.org/10.1016/j.epsl.2017.05.008, 2017.

Rowe, K. J. and Rutter, E. H.: Palaeostress estimation using calcite twinning: experimental calibration and application to nature, Journal of Structural Geology, 12(1), 1–17, https://doi.org/10.1016/0191-8141(90)90044-y, 1990.

Ryou, H., Drazin, J. W., Wahl, K. J., Qadri, S. B., Gorzkowski, E. P., Feigelson, B. N. and Wollmershauser, J. A.: Below the Hall–Petch Limit in Nanocrystalline Ceramics, ACS Nano, 12(4), 3083–3094, https://doi.org/10.1021/acsnano.7b07380, 2018.

Schmid, S. M., Boland, J. N., and Paterson, M. S.: Superplastic flow in finegrained limestone. Tectonophysics, 43(3-4), 257–291. https://doi.org/10.1016/0040-1951(77)90120-2, 1977

Seidemann, M., 2017, Microstructural evolution of polycrystalline ice during non-steady state creep [PhD thesis: University of Otago, p110].

Sheinerman, A. G., Castro, R. H. R. and Gutkin, M. Y.: A model for direct and inverse Hall-Petch relation for nanocrystalline ceramics, Materials Letters, 260, 126886, https://doi.org/10.1016/j.matlet.2019.126886, 2020.

Somekawa, H. and Mukai, T.: Hall–Petch Breakdown in Fine-Grained Pure Magnesium at Low Strain Rates, Metall and Mat Trans A, 46(2), 894–902, https://doi.org/10.1007/s11661-014-2641-2, 2015.

Spiers, C. J.: Fabric development in calcite polycrystals deformed at 400° C, bulmi, 102(2), 282–289, https://doi.org/10.3406/bulmi.1979.7289, 1979.

Ter Heege, J. H., De Bresser, J. H. P. and Spiers, C. J.: Rheological behaviour of synthetic rocksalt: the interplay between water, dynamic recrystallization and deformation mechanisms, Journal of Structural Geology, 27(6), 948–963, https://doi.org/10.1016/j.jsg.2005.04.008, 2005.

Treverrow, A., Budd, W. F., Jacka, T. H. and Warner, R. C.: The tertiary creep of polycrystalline ice: experimental evidence for stress-dependent levels of strain-rate enhancement, Journal of Glaciology, 58(208), 301–314, https://doi.org/10.3189/2012jog11j149, 2012.

Vaughan, M. J., Prior, D. J., Jefferd, M., Brantut, N., Mitchell, T. M. and Seidemann, M.: Insights into anisotropy development and weakening of ice from in situ P wave velocity monitoring during laboratory creep, Journal of Geophysical Research: Solid Earth, 122(9), 7076–7089, https://doi.org/10.1002/2017JB013964, 2017.

Walker, A. N., Rutter, E. H. and Brodie, K. H.: Experimental study of grain-size sensitive flow of synthetic, hot-pressed calcite rocks, Geological Society, London, Special Publications, 54(1), 259–284, https://doi.org/10.1144/gsl.sp.1990.054.01.24, 1990.

Warren, J. M. and Hirth, G.: Grain size sensitive deformation mechanisms in naturally deformed peridotites, Earth and Planetary Science Letters, 248(1-2), 438–450, https://doi.org/10.1016/j.epsl.2006.06.006, 2006.

Weertman, J. R.: Hall-Petch strengtheningin nanocrystalline metals, Materials Science & Engineering A, 16(1-2), 161–167, https://doi.org/10.1016/0921-5093(93)90319-a, 1993.

Zener, C. and Hollomon, J. H.: Effect of Strain Rate Upon Plastic Flow of Steel, Journal of Applied Physics, 15(1), 22–32, https://doi.org/10.1063/1.1707363, 1944.

A list of all relevant changes made in the manuscript

Extracts from original manuscript are in blue type (**P**=Page, **L**=Line, in the original manuscript). *Extracts from our revised manuscript are in italics (**P**=Page, **L**=Line, in the revised manuscript).*

1. Modifications in "Abstract"

1.1 "Understanding ice deformation mechanisms is crucial for understanding the dynamic evolution of terrestrial and planetary ice flow." **(P1, L10-15)** revised as:
*"In order to better understand ice deformation mechanisms, we document the microstructural evolution of ice with increasing strain." **(P1, L10-15)***

1.2 " 'Mechanical data show peak and steady-state stresses are larger at colder temperatures as expected from the temperature dependency of creep.' … 'At -30 °C, the c-axis CPO transits from a narrow cone to a cluster, parallel to compression, with increasing strain. This closure of the c-axis cone is interpreted as the result of a more active grain rotation together with a less effective GBM. As the temperature decreases, the overall CPO intensity decreases, facilitated by the CPO' " **(P1, L15 – P2, L5)** re-written as:
"*Microstructural data are generated from cryogenic electron backscattered diffraction (cryo-EBSD) analyses. All deformed samples contain sub-grain (low-angle misorientations) structures with misorientation axes that lie dominantly in the basal plane suggesting activity of dislocation creep (glide primarily on the basal plane), recovery and subgrain rotation.' … 'High-angle grain boundaries between small grains have misorientation axes that have distributed crystallographic orientations. This implies that, in contrast to subgrain boundaries, grain boundary misorientation is not controlled by crystallography. Grain boundary sliding of finer grains or nucleation of those grains in random orientations ("spontaneous" nucleation) could explain the weaker CPO of the fine-grained fraction and the lack of crystallographic control on high-angle grain boundaries.' " **(P1, L15 – P2, L11)***

2. Modifications in "Introduction"

2.1 Add references of **"** *Pollard, 2010; Kopp et al., 2017 " (**P2, L14**) and "Budd and Jacka, 1989" (**P2, L22**)*

2.2. *Add sentence of: "Ice core studies and field investigations suggest the temperature of ice in Antarctica and Greenland ranges between ice melting temperature and ~-30 °C (Kamb, 2008; Montagnat et al., 2014; Kuiper et al., 2019a, 2019b)." (**P2, L16-18**)*

2.3 "Enhancement correlates with the development of a crystallographic preferred orientation (CPO) (Jacka and Maccagnan, 1984; Vaughan et al., 2017) and also with other microstructural changes, in particular grain size reduction (Craw et al., 2018; Qi et al., 2019)." (**P2, L19-21**) re-writted as:
*"Enhancement correlates with the development of a crystallographic preferred orientation (CPO) (Jacka and Maccagnan, 1984; Vaughan et al., 2017) and also with other microstructural changes, particularly those associated with dynamic recrystallization (Duval, 1979; Duval et al., 2010; Faria et al., 2014; Montagnat et al., 2015), including grain size reduction (Craw et al., 2018; Qi et al., 2019)." (**P2, L29-L31**)*

2.4 "In this contribution we present microstructural analyses of samples deformed to successively higher strains through the transition from peak stress (secondary creep) to steady-state stress (tertiary creep) at -10, -20 and -30 °C." (**P2, L25-26**) re-written as:
*"In this contribution we present microstructural analyses of samples deformed to successively higher strains through the transition from peak stress to flow stresses at -10, -20 and -30 °C." (**P3, L3-4**)*

2.5 *Add sentences of: "Our results include microstructural data from samples deformed to progressively higher strains at -20 and -30 °C. Such data have not been presented before, and they are important, as understanding how and why different CPOs develop as a function of temperature should give a better insight into the mechanisms that control CPO development and mechanical behaviour. Furthermore, understanding CPOs in nature requires extrapolation of laboratory results to the much lower strain rates that occur in nature. To do this effectively we need to know how CPOs evolve across as wide a range of temperatures and strain rates as is possible. In this paper our objectives are to study the influences of temperature and strain on microstructure and CPO development and to discuss implications for mechanical behaviour." (**P3, L6-13**)*

3. Modifications in "Method"

3.1 Add sentence of *"To minimize thermal cracking, samples were progressively cooled to ~ -30, -100 and -196 °C over about 15 minutes, and thereafter stored in a liquid nitrogen dewar." **(P4, L8-9)**.*

3.2 Add sentence of *"Minor static recovery of the ice microstructures may happen on this timescale (Hidas et al., 2017), but significant change in CPO or grain size is unlikely." **(P4, L10-11)***

3.3 Add sentence of *"The angular resolution (error of crystallographic orientation measurement for each pixel) of the EBSD data is ~0.5°." **(P5, L9-10)***

3.4 Remove " 'We quantified the geometrically necessary dislocations (GNDs) (Ashby, 1970) using the Weighted Burgers Vector (WBV) method (Wheeler et al., 2009). GNDs are the dislocations required to generate an observed lattice distortion (for example, a sub-grain boundary).' … 'The value of ϕWBVc ranges from 0 (when the dislocation is dominated by a-component Burgers vectors) to 1 (when the dislocation is dominated by c-component Burgers vectors).' " (**P5, L9-23**)

3.5 Add sentence of *"Grain size, grain shape, grain boundary morphology, and CPO provide useful information for inferring ice deformation processes." **(P5, L12-13)***

3.6 Add section 2.5.1 and corresponding paragraphs *" 'Ice grains were reconstructed from the raw EBSD pixel maps with 5 µm step size using the MTEX algorithm of Bachmann and others (2011) with a grain boundary threshold of 10°. Grains with area equivalent diameters lower than 20 µm were removed from the data.' … 'We calculated subgrain size using boundary misorientation thresholds of ≥ 2°. Grain size and subgrain size were calculated as the diameter of a circle with the area equal to the measured area of each grain or subgrain. Note that grain size or subgrain sizes represent the sizes of 2-D cross sections through 3-D grains.' … 'Grains (in 2-D) that are in the same orientation (they have a misorientation below a defined threshold) and in reasonable proximity (that depends on grain size) are candidates for being 2-D slices through the same grain that has an irregular geometry in 3-D. These analyses are presented in section S3 of the supplementary material.' " **(P5, L15 – P6, L2)***

3.7 Add section 2.5.2. Add sentences in section 2.5.2 *"The CPO data were contoured with a half-width of 7.5° based on the maximum of multiples of a uniform distribution (MUD) of the points, to more clearly show the CPO patterns." **(P6, L5-6)**. "The opening-angle, θ, of c-axes cone is considered important in indicating the relative activity of grain rotation and grain boundary migration (GBM), which are competing processes in deforming ice (Piazolo et al., 2013; Qi et al., 2017)." **(P6, L10-12)***

3.8 Add section 2.5.3 and corresponding paragraphs *"Deformation processes may leave signatures in misorientation data (Fliervoet et al., 1999; Wheeler et al., 2001, 2003; Montagnat et al., 2015; Qi et al., 2017). Misorientation describes the rotation axis and angle required to map one lattice orientation onto another (Wheeler, et al., 2001). Because of crystal symmetry, there is more than one rotation that can be used to describe a misorientation. We chose the minimum rotation angle and corresponding rotation axis to describe misorientation (i.e., the disorientation, in the material science nomenclature—Grimmer, 1979; Morawiec 1995; Wheeler et al., 2001). Here we refer to the minimum rotation angle and corresponding rotation axis as the misorientation angle and misorientation axis, separately. Misorientation angle distributions are illustrated as histograms; misorientation axes distributions are illustrated as inverse pole figures. In this study, we applied three groups of pixel-by-pixel misorientation analyses, using the EBSD data with 5 µm step size:*

(1) Neighbour-pair misorientations: using neighbouring pixels.
(2) Random-pair misorientations: using randomly selected pixels.
(3) Grain boundary misorientations: using pixels along the grain boundaries of neighbouring grains."

(P6, L18-30)

4. Modifications in "Results"

4.1 Add section 3.1 and corresponding paragraph *"Undeformed samples exhibit a foam-like microstructure with straight or slightly curved grain boundaries and polygonal grain shapes (Fig. 2(a)). The grain size distribution is slightly skewed. The frequencies of grains increase slightly from the minimum cut off grain size (20 µm) to a peak at around 300 µm, and then decrease with further increasing grain size (Fig. 2(b)). Mean and median* *grain sizes are 297 µm and 291 µm, respectively (Table 3). The mean and median subgrain sizes at 291 and 280 µm, respectively, are very close to mean and median grain sizes (Table 3), indicating that there are very few subgrain boundaries. CPO is close to random (Fig. 2(c)), with an M-index of ~0.004 (Table 2). Neighbour-pair and random-pair misorientation angle distributions both resemble the distribution calculated for randomly oriented hexagonal crystals (Fig. 2(d), Morawiec, 1995; Wheeler et al., 2001)." **(P7, L2-10)***

4.2 Change Section 3.1 to *Section 3.2* "At strains larger than ~0.1, stresses reduce only a modest amount, with steady-state reached at a strain of ~0.2. Peak and final stresses are larger at colder temperatures and the peak stresses are better defined at -30 °C than at the warmer temperatures." **(P6, L9-11)** revised as:
*"The rate of stress reduction is at a minimum, for each temperature, at strains larger than ~0.1. Peak and final stresses are larger at colder temperatures. Ratios of peak stress to stresses at higher strain (e.g. final stress of ~20% strain) are approximately the same at all temperatures so that all curves, when normalised to the peak stress look similar." **(P7, L16-19)***

4.3 Change Section 3.2 to *Section 3.3*. "EBSD data are used to generate the illustrative grain orientation maps, grain sub-structure maps, as highlighted by WBV analysis, grain size distributions and subgrain size distributions shown in Fig. 3-5." **(P6, L13-14)** modified to:
*"EBSD data are used to generate the illustrative grain orientation maps, grain sub-structure maps, grain size distributions, subgrain size distributions and misorientation angle distributions shown in Figs. 4-6." **(P7, L21-22)***

4.4 "Note that the quantitative microstructural analyses and CPO data are based on larger areas than those presented in the EBSD maps (Table 2)." **(P6, L16-17)** modified to:
*"We only show selected areas of EBSD maps so that the reader can resolve microstructural features. Quantitative microstructural analyses are based on much larger areas than those presented in the figures (Table 2)." **(P7, L23-25)***

4.5 Re-wrote section 3.2.1 **(P6, L19-26)** (now *section 3.3.1*). *" 'All samples deformed at -10 °C and -20 °C show large, lobate grains interlocking with finer, less lobate grains (Fig. 4(a-b), 5(a-b)). Grain boundary lobateness increases at higher strains. The scale of lobateness—that is, the amplitude of grain boundary irregularities—is smaller at -20 °C than -10 °C. At -30 °C lobate grain boundaries are less common at low strains but are a common attribute of larger grains at 20% strain (Fig. 6(a-b)).' ... 'The colouring of the IPF maps changes with increasing strain, corresponding to the increasing strength of the CPO. At -10 °C, grains with near-pink-and-orange colours dominate the IPF maps at strains higher than ~8% (Fig. 4(a-b)). At -20 and -30 °C, grains with red, pink and orange colours dominate the IPF maps at ~20% strain (Fig. 5(a-b) and 6 (a-b)).' " **(P7, L26 – P8, L8)***

4.6 Re-wrote section 3.2.2 **(P7, L1-24)** (now *section 3.3.2*). *" 'For samples deformed to ~3% strain, the grain size distributions are strongly skewed or possibly bimodal, with a clear main peak at finer grain sizes and a tail of coarser sizes with a broad, poorly defined secondary peak corresponding to the mean grain size of the starting material (Fig. 4(d), 5(d) and 6(d)).' ... 'Stereological artefacts inevitably arise from looking at microstructures on two-dimensional sections. Here we analyse two distinct (albeit related) stereological issues. The first issue relates to the misidentification of "small" grains, as these could appear from slices cut close to the perimeter of a large grain in 3-D (Underwood, 1973). The second issue relates to the oversampling of grains that have highly irregular, branching shapes in 3-D and appear more than once on a 2-D surface (Hooke and Hudleston, 1980; Monz et al, 2020).' ... 'The analyses above provide some confidence that in all the experiments the number density of grains has increased relative to the starting material and increases with strain. If we couple this to the grain size statistics presented and the analysis of whether we are misidentifying small grains, the weight of evidence suggests that we have a real population of smaller grains. Our confidence in this statement increases with reducing temperature and increasing strain. Now we come back to the issue of how we distinguish "big" and "small" grains. Our scheme for separating "big" and "small" grains, using* D_{SMR} *of the sample deformed to ~12% strain as the threshold, is not perfect, but it does provide a fast and repeatable way of looking at the possible differences in microstructures and CPO of smaller and larger grains. The grain size threshold chosen (peak, mean, median and SMR) to separate "big" and "small" grains has little impact on the CPOs of the "big" and "small" grain populations (see section S5 of the supplementary material).' " **(P8, L9 – P10, L11)***

4.7 Re-wrote section 3.2.3 **(P7, L25- P8, L12)** (now *section 3.3.3*). *"Subgrain size distributions (Fig. 4(e), 5(e) and 6(e)) are similar to the grain size distributions (Fig. 4(d), 5(d) and 6(d)), but the median and mean subgrain* *sizes are smaller than median and mean grain sizes (Table 3). In many cases, particularly at lower temperatures, the peak corresponds to the lower grain size resolution (cut off) indicating that we could be missing smaller subgrains. For this reason, the peak subgrain sizes are not useful and the median and mean subgrain sizes probably represent overestimates." **(P10, L12-17)***

4.8 Remove section 3.2.4 (**P8, L13- P8, L30**)

4.9 Add section 3.3.4. *" 'Misorientation angle distributions are presented for misorientations between 2° and 20° (Fig. 4(f), 5(f), 6(f)). Random-pair misorientation angle distributions show the misorientations expected for the measured CPO. It is important to identify differences between neighbour- and random-pair distributions, as these can be attributed to orientation inheritance, among other processes (Wheeler et al., 2001).' … ' Grain boundary (>10°) misorientation axes for neighbouring grains are not strongly aligned. There is a very slight preference for misorientation axes lying in the basal plane (except PIL007) and this preference is slightly stronger at colder temperatures.'… 'Some of the small grains have c-axes within the single grain that are dispersed in a great circle smear, with up to ~5° of c-axis orientation variation. The distributions of misorientation axes between each of the reference grains and it's neighbouring small grains show no particular pattern apart from an absence of misorientation axes close to [0001]. These are all high-angle (>10°) misorientation so the axis errors will be small (Prior, 1999). The boundary misorientation axes between neighbouring "small" grains are distributed relatively uniformly (Fig. 7(d)), apart from an absence of data close to [0001].' " **(P10, L18 – P11, L15)***

4.10 Add section 3.4.4. *" 'The "big" and "small" grains have similar patterns of c-axes (i.e. maxima in approximately the same places)—samples deformed to ~12% strain illustrate this (Fig. 12).' … 'To show how CPO strength differs for "big" and "small" grains for the whole data set we plot the M-indices for the grain size categories against strain (Fig. 11(d)). For all the deformed samples, the M-indices of "big" grains have the same pattern with strain as the complete data set (all grains). The "small" grains generally have lower M-indices at strains of* $\varepsilon \geq$ *~5%. The grain size threshold (*$\overline{D}$, D_{SMR}, D_{median} *and* D_{peak}*) chosen to separate "big" and "small" grains has a minor impact on CPO, with no significant change in CPO pattern or intensity (see section S5 of the supplementary material for the test).' " **(P12, L11-24)***

4.11 Add sentence of *"To increase our understanding of the processes that might control the c-axes cone opening-angle* θ*, we plotted data from this study and previous studies in a diagram of* θ *as a function of strai,n with data subdivided with different temperatures and strain rates (Table 4 and Fig. 13)." **(P12, L26-28)***

4.12 Add sentences and equations of *"For natural ice samples (top of the south dome, Barnes Ice Cap, Baffin Island) from Hooke and Hudleston (1981), Eq. (8) was used to calculate axial engineering strain (*e*) from natural octahedral unit shear strain (*$\bar{\gamma}_{oc}$*). Values of* $\bar{\gamma}_{oc}$ *were taken from Fig. 4 of Hooke and Hudleston (1981) based on the assumption that ice was deformed under uniaxial compression. After that, the axial engineering strains (*e*) were converted to true axial strains (*ε*) using Eq. (4). Hooke and Hudleston (1981) assumed their natural ice samples were deformed under a constant vertical strain rate,* $\dot{e}$*, of* $5.71 \times 10^{-11} s^{-1}$*, which converted to true axial strain rate (*$\dot{\varepsilon}$*) using Eq. (5). The derivation of Eq. (4-8) are shown in section S2 of the supplementary material."*

$$\bar{\gamma}_{oc} = \frac{2\sqrt{2}}{3}\left(e + \frac{1}{\sqrt{1-e}} - 1\right) \tag{8}$$

(P13, L16-23)

4.13 Add sentence *of "For natural ice deformed under temperatures of -4~-6 °C,* θ *generally decreases with increasing strain for both "coarse" ice (>0.15 cm2) and "fine" ice (<0.1 cm2)." **(P14, L5-6)***

5 Modifications of "Discussion"

5.1 "The stress-strain curves (Fig. 1) at all temperatures first rise to the peak stresses and then relax to approach near-constant stresses with strains." (**P11, L21-22**) revised to:
*"All stress-strain curves (Fig. 3) show stress rising to the peak stress and then relaxing, with the rate of stress drop decreasing with strain." **(P14, L13-14)***

5.2 "…and is comparable to the constant-load experiments (Budd and Jacka, 1989; Jacka and Li, 2000; Treverrow et al, 2012; Wilson and Peternell, 2012) where strain rate first decreases to a minimum and then increases to approach a near-constant strain rate" (**P11, L24-25**) revised to:
*"…and has an approximate inverse relationship (Mellor and Cole, 1982, 1983; Weertman, 1983) to constant-load experiments (Budd and Jacka, 1989; Jacka and Li, 2000; Treverrow et al, 2012; Wilson and Peternell, 2012)…" **(P14, L15-17)***

5.3 Add sentence *"Stress-strain curves of all experimental runs show a smooth and continuous increase of stress as a function of strain before reaching the peak. Approximately linear portions of the stress-strain data prior to peak have been termed quasi-elastic (Kirby et al., 1987)." **(P14, L19-21)***

5.4 "This and the curvature of the stress strain line at the start of each experiment suggests that there is also some dissipative deformation here. This can include porosity loss (Vaughan et al., 2017) and the intergranular stress redistribution used to explain primary creep in constant load experiments (Duval et al, 1983)." (**P11, L27-30**) revised to:
*"This likely includes anelastic deformation related to intergranular stress redistribution used to explain primary creep in constant load experiments (Duval et al, 1983; Castelnau et al., 2008). The curvature of the stress strain line at the start of each experiment may relate to initial porosity loss as suggested by rapid increases in ultrasonic p-wave velocity in comparable experiments by Vaughan and others (2017)." **(P14, L22-25)***

5.5 Add sentences *"As our experiments are all at the same approximate strain rate, we cannot calculate the stress dependency of strain rate (the stress exponent, n). Qi and others (2017) calculate a peak stress n value of 3 and flow stress n value of 3.9 for comparable experiments (including PIL007 used here) at -10 °C. Craw and others (2018) calculate a peak stress n value of 4.1 for comparable experiments at -30 °C." **(P14, L26-29)***

5.6 Add sentences *"Our peak and final stress data can be used to calculate the activation energy by assumption of a value of stress exponent, n (see section S6 of the supplementary material for the calculation). Best fit to all data (-10, -20 and -30 °C) give activation energy of 98 kJ/mol and 103 kJ/mol from peak and final stress data assuming n=3 and 131 kJ/mol and 138 kJ/mol from peak and flow stress data assuming n=4. These numbers are consistent with published values (64-250 kJ/mol) at relatively high temperature (Glen, 1955; Goldsby, 2001; Budd and Jacka, 1989; Cuffey and Paterson, 2010; Durham et al., 2010; Kuiper et al., 2019a, 2019b)." **(P15, L1-6)***

5.7 Remove "The drop of stress after peak correlates with dynamic recrystallization driven grain size reduction and CPO development (Jacka and Maccagnan, 1984; Vaughan et al., 2017; Qi et al., 2019). Experiments with initial grain size as a variable, under comparable conditions to our experiments, suggest that grain size sensitive mechanisms are important (Qi et al., 2017). Grain boundary sliding (GBS) is kinematically required for all grain size sensitive mechanisms (Stevens,1971; Gates and Stevens, 1974), including diffusion creep (Boullier and Gueguen, 1975; Behrmann and Mainprice, 1987) and dislocation slide accompanied by GBS (disGBS) (Warren and Hirth, 2006). Goldsby and Kohlstedt (1997, 2001, 2002) suggest a general importance of GBS on the basis of the constitutive law parameters required to fit the mechanical data from experimentally deformed fine-grained ice. Recent studies suggest GBS in fine-grained ice layers has a key role in controlling the Greenland ice flow (Kuiper et al., 2019a, 2019b) by applying the Goldsby-Kohlstedt flow law (Goldsby and Kohlstedt, 1997, 2001) to modelling the deformation in the NEEM (North Greenland Eemian Ice Drilling) deep ice core. The grain size reduction resulting from dynamic recrystallization is thought to cause mechanical weakening by increasing the strain rate contribution of grain size sensitive deformation mechanisms (De Bresser et al., 2001). A development of strong CPO can also lead to mechanical weakening in viscously anisotropic materials (Durham and Goetze, 1977; Hansen et al., 2012) such as ice." (**P12, L1-11**)

5.8 Sub-divide section 4.1.2, remove discussions related with boundary hierarchy analyses and boundary lobateness (sphericity parameters). Rewrite section. 4.1.2:
*"**4.1.2.1. Nucleation***
'The number density (number of grains per unit area) of "distinct" grains (counting 2-D grains attributed to the same 3-D grain as one: section S4 of supplementary material) increases by more than a factor of 3 times that of the starting material in all deformed samples at all temperatures (Table 3). We can be reasonably confident that the number of grains in the samples has increased as a function of deformation. This requires a process of nucleation to create new grains. For all the deformed samples, the grain size distributions are characterised by peaks at finer grain sizes, and a smaller mean/median grain size compared with the undeformed sample (Fig. 2,

4-6, Table 3). The smallest grains in the deformed samples were not present in the starting material. These observations suggest that nucleation generates the grains with smaller sizes. Grain number density generally increases and all measures of 2-D grain size decrease with strain (Table 3), at all temperatures, suggesting that nucleation operates continuously as part of the recrystallisation process throughout the deformation.'

4.1.2.2. Dislocation activity, recovery, subgrain rotation and subgrain rotation recrystallisation

'Microstructure maps show subgrain boundaries in all deformed ice samples (Fig. 4(a-c), 5(a-c) and 6(a-c)). The subgrain boundary geometry is comparable with other experimentally or naturally deformed rock and metal samples, e.g. quartz (Cross et al., 2017a; Killian and Heilbronner, 2017), Olivine (Hansen et al., 2012), Magnox alloy (Wheeler, 2009) and Zircon (MacDonald et al., 2013). The misorientation axes for subgrain boundaries are generally rotations around rational crystallographic axes, particularly directions in the basal plane, suggesting that the boundaries may represent arrays of dislocations (Humphreys and Hatherley, 2004; Shigematsu et al., 2006). There is much higher frequency of low angle (Particularly < 10°) neighbour-pair misorientations than are expected from the CPO (as shown by the random-pair misorientation angles).' … 'At all temperatures and strains the mean/median subgrain size is smaller than the mean/median grain size. This indicates that the subgrain rotation recrystallization could be the nucleation mechanism that generates the "small" grain population. Previous studies on deformed metals and quartzites describe the structure of smaller grains encircling larger grains as "core-and-mantle" structure (Gifkins, 1976; White, 1976).' … 'The network of smaller grains that encircle bigger grains at strains higher than 12% at -20 and -30 °C is consistent with the operation of a subgrain rotation recrystallization mechanism. The network of finer grains encircling larger grains has been observed in deformed metals, and it is named as the "necklace structure" in the material science literature (e.g. Ponge and Gottstein, 1998; Jafari and Najafizadeh, 2009; Eleti et al., 2020). Lately, Eleti and others (2020) used a fiducial marker grid to show that the deformation of finer grains in the necklace structure includes a significant component of GBS.' … 'Jacka and Li (1994) show an inverse relationship between ice grain size and stress from deformed ice samples that reach tertiary creep.'

4.1.2.3. Grain boundary migration

*'Lobate grain boundaries are commonly interpreted as the result of strain-induced grain boundary migration (GBM) (Urai et al., 1986; Jessell, 1986; Duval and Castelnau., 1995). Samples deformed at -10 and -20 °C show more grains with lobate boundaries at higher strains (>~3%), suggesting more widespread strain-induced GBM with an increasing strain. The proportion of repeated (i.e. interconnected and highly lobate) grains is generally higher in the higher-temperature experiments (Table 2, section S4 of the supplementary material). This observation suggests that GBM is also more widespread at higher temperatures.' " (***P15, L8 – P16, L29***)

5.9 Separate section 4.1.3 (Inferences from CPO development) **(P14, L1 – P15, L8)** into two sections of *4.1.3 (CPO development)* and *4.1.4 (CPO development: differences related to grain size). Sections of 4.1.3 and 4.1.4 are mostly newly written.*

"**4.1.3 CPO development**

'Many deformed samples exhibit an incompleteness of c-axes cone (lack of cylindrical symmetry) (Fig. 8-10). The incompleteness of c-axes cone is more severe for 5 μm EBSD maps collected from a much smaller area than 30 μm EBSD maps (Fig. 12). These phenomena are common to all ice CPOs from measurements on a single sample planes (by EBSD or optical methods: see any of the papers cited), but are not so apparent in neutron diffraction data (Piazolo et al., 2013; Wilson et al., 2019), that sample a larger volume, suggesting that a single plane through a deformed sample does not generally contain sufficient grains for a fully representative CPO.' … 'Cone-shaped c-axes CPOs have been related to strain-induced GBM favouring the growth of grains with easy slip orientations (high Schmid Factors) (Duval and Castelnau., 1995; Little et al., 2015; Vaughan et al., 2017; Qi et al., 2017). Linked to this is the idea that grains with hard slip orientations should have greater internal distortions (Duval and Castelnau., 1995; Bestmann and Prior 2003), and therefore store higher internal strain energy. If this is correct then hard slip grains are likely to be consumed by grains with easy slip orientations through GBM (Duval and Castelnau., 1995; Castelnau et al., 1996; Bestmann and Prior, 2003; Piazolo et al., 2006; Killian et al., 2011; Qi et al., 2017; Xia et al., 2018). However, we have to re-evaluate the detail of this idea, as recent studies on deformed ice samples show there is no systematic relation between orientation and strain localisation at low strain (Grennerat et al. 2012). Furthermore, studies of high-strain shear samples find no clear difference in the geometrically necessary dislocation density within the two maxima that develop in simple shear (Journaux et al. 2019). An alternative, and as yet incomplete, explanation from Kamb (1959) relates recrystallisation directly to the elastic anisotropy of crystals and through this to the orientation of the stress field. At this stage the observation that ice CPOs developed at relatively high temperature and particularly at low strain correspond to high Schmid factor orientations remains robust. The underlying mechanisms will need continual review as we collect new data.' … ' The opening-angle θ of the c-axes cone as well as the CPO intensity decrease with decreasing temperature (Table 2, 4; Fig. 8-10, 11(c), 13). Earlier studies have inferred that the selective growth of the grains oriented for easy slip orientations becomes

less active due to the reduction of GBM activity at lower temperatures (Qi et al., 2017, 2019). Lower temperatures, for constant displacement rate experiments, correspond to higher stresses. Previous studies in deformed metals suggest a higher stress is likely a cause of higher dislocation densities (Bailey and Hirsch, 1960; Ajaja, 1991), that in turn will require kinematically more lattice rotation. The misorientation angle at which neighbour-pair frequency reduces to be equal to the random-pair frequency increases with decreasing temperature (Fig. 4(f), 5(f), 6(f)). Moreover, neighbour-pair misorientation axes at misorientation angles of 5°-10° show primary maxima lying in the basal plane (Fig. 4 (g), 5(g), 6(g)) for all deformed samples. These observations support the hypothesis that grain rotation becomes more prominent at lower temperatures (Jacka and Li., 2000), and it is dominantly driven by intracrystalline glide on the basal plane. More active grain rotation can lead to a closure of c-axis cone at lower temperatures: maxima parallel to compression are characteristic of strains ≥ 20% at temperatures colder than -30 °C (Craw et al., 2018; Prior et al., 2015).' " ***(P16, L30 – P18, L16)***

"**4.1.4 CPO development: differences related to grain size**
'The CPO intensity (as indicated by M-index) of "small" grains is generally lower than "big" grains, and this contrast strengthens with decreasing temperature (Fig. 11(d)). At ~12% strain, the CPO pattern of "big" grains is clearer than "small" grains, at all temperatures (Fig. 12). These observations suggest a mechanism that weakens the CPO development may be associated with the "small" grains. At lower temperatures (-20 °C and -30 °C) typical "core-and-mantle" structures have small grains with orientations that are dispersed around neighbouring large grains (Fig. 7) and the misorientations of small grains with large or small neighbours lack a consistent or rational crystallographic control crystallographic control.' … 'Both hypotheses—"spontaneous" nucleation and GBS—explain a weakening of CPO in "small" grains and these two ideas are not mutually exclusive. We have greater confidence in the GBS interpretation because it is consistent with the grain size sensitivity that is observed in comparable ice deformation experiments. Without GBS another explanation is needed for the grain size sensitivity. Further work is needed to test both hypotheses. Most critical are experiments where nuclei can be observed whilst they are very small and subsequent misorientations can be documented, as might be possible with 3-D microscopy methods (Lauridsen et al., 2003; Poulson et al., 2004), and experiments where fiducial markers are used to confirm the physical existence of offsets on grain boundaries (Schmid et al, 1977; Spiers, 1979 ; Beeré, 1978; Eleti et al., 2020).' " ***(P18, L17 – P19, L18)***

5.10 Re-write section 4.2 (**P15, L9-18**). *"The mechanical weakening, i.e. stress drop after peak in constant load experiments and strain rate enhancement from secondary to tertiary creep in constant load experiments, has been associated with: (1) the softening of grains related to reduction in defect content associated with dynamic recovery and recrystallisation (Montagnat and Duval., 2000; Sakai et al., 2014), (2) increased contribution of grain size sensitive deformation mechanisms due to grain size reduction resulting from dynamic recrystallization (De Bresser et al., 2001), and (3) development of strong CPO in viscously anisotropic materials (Durham and Goetze, 1977; Hansen et al., 2012) such as ice. The microstructural data as discussed in section 4.1 will enable us to comment on the contribution of different mechanisms to the weakening in deformed polycrystalline ice.*
All experiments show weakening after peak stress. Weakening is classically observed during dynamic recrystallization, and it was attributed to a balance between GBM and nucleation of new grains (Montagnat and Duval., 2000; Sakai et al., 2014). In this study, mean and median ice grain size reduces with strain at all temperatures (Table 3, Fig. 11(a)). Grain size is commonly reduced during rock deformation in the laboratory (e.g. Pieri et al., 2001; Hansen et al., 2012) and in nature (Trimby et al., 1998; Bestmann and Prior, 2003). At smaller grain sizes the strain rate contribution of grain size sensitive (GSS) mechanisms increases or the stress required to drive a given strain rate contribution of GSS decreases. For this reason, grain size reduction has been proposed as a weakening mechanism (Rutter and Brodie, 1988; De Bresser et al 2001; Kilian et al., 2011; Campbell and Menegon, 2019). On the other hand, many published papers on ice sheet mechanics imply that enhancement (weakening) is caused by anisotropy development and there are analytical numerical models that seek to quantify this relationship (Azuma, 1995; Morland and Staroszczyk, 2009; Placidi et al., 2010). At -10 °C the CPO development includes many grains with basal plane orientations that would facilitate further axial shortening and it is intuitive that the CPO development could provide a cause for the weakening. However, at -30 °C the CPO developed at high strain is a narrow cone or cluster with many basal planes sub-perpendicular to compression. In this case the CPO would hinder further axial shortening and it is intuitive that the CPO should cause strengthening. Nevertheless, weakening occurs at -30 °C. Development of CPO cannot provide a uniform explanation for weakening across the range of laboratory experiments presented here. Therefore, further studies are required to quantify: (1) the contribution of nucleation and GBM to the total stress drop if the balance of GBM and nucleation is considered as the weakening mechanism; (2) The contribution of grain

size insensitive, e.g. dislocation creep, and grain size sensitive processes, e.g. GBS, to the total stress drop if grain size reduction is considered as the weakening mechanism.” ***(P19, L19-P20, L11)***

6 Re-write section 5 (conclusions) (**P15, L19-P16, L22**).

“

1. *We deformed isotropic polycrystalline pure water ice to successive strains (~3%, 5%, 8%, 12% and 20%) under a constant displacement rate (strain rate* $\sim 1.0 \times 10^{-5} s^{-1}$*) at -10, -20 and -30 °C. For all deformed samples, stress first rises to a peak at ~1-4% strain and then drops to lower stresses at higher strains. Samples deformed at colder temperatures show higher peak and final stresses, as expected for the temperature dependency of creep. Microstructural and CPO analyses were conducted on deformed ice samples using cryo-EBSD.*
2. *All deformed samples develop distinct subgrain boundaries and show a peak at 2°-3° in the neighbour-pair misorientation angle distribution. Mean/median subgrain size is smaller than mean/median grain size. These observations suggest that dislocation glide and associated recovery and subgrain rotation were active in all deformed samples. Neighbour-pair low-angle (5°-10°) misorientation axes show primary maxima lying in the basal plane, for all samples, suggesting that basal glide dominated the intragranular deformation process. Subgrain boundary misorientation distributions extend to higher misorientation angles with strain and with decreasing temperature, suggesting that subgrain rotation develops progressively and is more effective at lower temperatures.*
3. *All deformed samples have skewed grain size distributions with a strong peak at small (<100 μm) sizes and a tail to larger sizes. The grain size peak is smaller than the grain size of the starting material (~297 μm) and a stereological analysis suggests that many of the small grains, measured in 2 - dimensions, are also small in 3 – dimensions. The number density of “distinct” grains (counting 2-D grains that are out of the analysis plane to the same 3-D grain) is more than 3 times that in the starting material for all deformed samples and the number density increases with strain. These data suggest that nucleation is involved in dynamic recrystallization. “Core-and-mantle” (small grains surrounding larger grains) are observed at high strains and are clearest at -20 and -30 °C, suggesting that subgrain rotation recrystallization has occurred and is more important at lower temperatures. Lobate grain boundaries suggest that strain induced grain boundary migration has occurred in all samples.*
4. *Many of the deformed samples have CPOs defined by open cones (small circles) of c-axes. The cone opening-angle decreases with strain. The CPO intensity and c-axis opening-angle both decrease as the temperature drops from -10 °C to -30 °C. At -30 °C and 20% strain the c-axes define a cluster with maximum parallel to compression, rather than an open cone. We interpret that the of the open c-axis cone develops because strain-induced GBM favours the growth of grains in easy slip orientations. The closure of the c-axes cone with strain is interpreted primarily as the result of grain rotation related to intragranular dislocation glide on the basal plane. We infer that grain rotation becomes more prominent at lower temperatures, whilst GBM is more effective at higher temperatures.*
5. *Small grains have a weaker CPO than large grains. This distinction is slight at -10 °C, but becomes much clearer at lower temperatures. Neighbour-pair high-angle (≥ 10°) misorientation axes, corresponding to grain boundaries are not strongly aligned in the basal plane, nor with any other crystal direction. An additional process is needed to explain these observations. We identify two candidate processes; (1) grain boundary sliding causing rotation of grains without crystallographic control on the rotation axes and (2) “spontaneous” nucleation in random initial orientations.”* ***(P20, L11 – P21, L14)***

7 Added references:

Ajaja, O.: Role of recovery in high temperature constant strain rate deformation, J Mater Sci, 26, 6599–6605, https://doi:10.1007/BF02402651, 1991.

Austin, N. J. and Evans, B.: Paleowattmeters: A scaling relation for dynamically recrystallized grain size, Geology, 35, 343–4, https://doi.org/10.1130/g23244a.1, 2007.

Azuma, N.: A flow law for anisotropic polycrystalline ice under uniaxial compressive deformation, Cold Regions Science and Technology, 23, 137–147, https://doi.org/10.1016/0165-232x(94)00011-l, 1995.

Bailey, J. E. and Hirsch, P. B.: The dislocation distribution, flow stress, and stored energy in cold-worked polycrystalline silver, Philosophical Magazine, 5, 485–497, https://doi.org/10.1080/14786436008238300, 1960.

Beeré, W.: Stresses and deformation at grain boundaries, Philosophical Transactions of the Royal Society of London. Series A, Mathematical and Physical Sciences, 288(1350), 177–196, https://doi.org/10.1098/rsta.1978.0012, 1978.

Berger, A., Herwegh, M., Schwarz, J.-O. and Putlitz, B.: Quantitative analysis of crystal/grain sizes and their distributions in 2D and 3D, Journal of Structural Geology, 33, 1751–1763, https://doi.org/10.1016/j.jsg.2011.07.002, 2011.

Budd, W. F., Warner, R. C., Jacka, T. H., Li, J. and Treverrow, A.: Ice flow relations for stress and strain-rate components from combined shear and compression laboratory experiments, Journal of Glaciology, 59(214), 374–392, https://doi.org/10.3189/2013jog12j106, 2013.

Campbell, L. R. and Menegon, L.: Transient High Strain Rate During Localized Viscous Creep in the Dry Lower Continental Crust (Lofoten, Norway), Journal of Geophysical Research: Solid Earth, 124, 10240–10260, https://doi.org/10.1029/2019jb018052, 2019.

Castelnau, O., Duval, P., Lebensohn, R. A. and Canova, G. R.: Viscoplastic modeling of texture development in polycrystalline ice with a self-consistent approach: Comparison with bound estimates, Journal of Geophysical Research: Solid Earth, 101 13851–13868, https://doi.org/10.1029/96JB00412, 1996.

Castelnau, O., Duval, P., Montagnat, M. and Brenner, R.: Elastoviscoplastic micromechanical modeling of the transient creep of ice, Journal of Geophysical Research, 113(B11), 749–14, https://doi.org/10.1029/2008JB005751, 2008.

Cross, A. J., Prior, D. J., Stipp, M. and Kidder, S.: The recrystallized grain size piezometer for quartz: An EBSD-based calibration, Geophysical Research Letters, 44, 6667–6674, https://doi.org/10.1002/2017gl073836, 2017a.

Cross, A. J., Hirth, G. and Prior, D. J.: Effects of secondary phases on crystallographic preferred orientations in mylonites, Geology, 45, 955–958, https://doi.org/10.1130/g38936.1, 2017b.

Derby, B.: The dependence of grain size on stress during dynamic recrystallisation, Acta Metallurgica et Materialia, 39, 955–962, https://doi.org/10.1016/0956-7151(91)90295-c, 1991.

Durham, W. B. and Goetze, C.: Plastic flow of oriented single crystals of olivine: 1. Mechanical data, Journal of geophysical Research, 82, 5737-5753, https://doi.org/10.1029/jb082i036p05737, 1977.

Duval, P.: Creep and recrystallization of polycrystalline ice, bulmi, 102, 80–85, https://doi.org/10.3406/bulmi.1979.7258, 1979.

Duval, P., Ashby, M. F., and Anderman, I.: Rate-controlling processes in the creep of polycrystalline ice, J. Phys. Chem., 87, 4066–4074, https://doi.org/10.1021/j100244a014, 1983.

Duval, P., Montagnat, M., Grennerat, F., Weiss, J., Meyssonnier, J., and Philip, A.: Creep and plasticity of glacier ice: a material science perspective, Journal of Glaciology, 56, 1059–1068, https://doi.org/10.3189/002214311796406185, 2010.

Eleti, R. R., Chokshi, A. H., Shibata, A., and Tsuji, N.: Unique high-temperature deformation dominated by grain boundary sliding in heterogeneous necklace structure formed by dynamic recrystallization in HfNbTaTiZr BCC refractory high entropy alloy, Acta Materialia, 183, 64–77, https://doi.org/10.1016/j.actamat.2019.11.001, 2020.

Falus, G., Tommasi, A., and Soustelle, V.: The effect of dynamic recrystallization on olivine crystal preferred orientations in mantle xenoliths deformed under varied stress conditions, Journal of Structural Geology, 33, 1528–1540, https://doi.org/10.1016/j.jsg.2011.09.010, 2011.

Fliervoet, T. F., Drury, M. R., and Chopra, P. N., Crystallographic preferred orientations and misorientations in some olivine rocks deformed by diffusion or dislocation creep: Tectonophysics, 303, 1-27, https://doi.org/10.1016/s0040-1951(98)00250-9, 1999.

Gifkins, R.: Grain-boundary sliding and its accommodation during creep and superplasticity, Metallurgical transactions a, 7, 1225-1232, https://doi.org/10.1007/bf02656607, 1976.

Glen, J. W.: The creep of polycrystalline ice. Proceedings of the Royal Society of London. Series A. Mathematical and Physical Sciences, 228, 519-538, https://doi.org/10.1098/rspa.1955.0066, 1955.

Gomez-Rivas, E., Griera, A., Llorens, M. G., Bons, P. D., Lebensohn, R. A., and Piazolo, S.: Subgrain rotation recrystallization during shearing: insights from full-field numerical simulations of halite polycrystals, Journal of Geophysical Research: Solid Earth, 122, 8810-8827, https://doi.org/10.1002/2017jb014508, 2017.

Grennerat, F., Montagnat, M., Castelnau, O., Vacher, P., Moulinec, H., Suquet, P. and Duval, P.: Experimental characterization of the intragranular strain field in columnar ice during transient creep, Acta Materialia, 60, 3655–3666, https://doi.org/10.1016/j.actamat.2012.03.025, 2012.

Grimmer, H.: The distribution of disorientation angles if all relative orientations of neighbouring grains are equally probable, Scripta Metallurgica, 13, 161–164, https://doi.org/10.1016/0036-9748(79)90058-9, 1979.

Hidas, K., Tommasi, A., Mainprice, D., Chauve, T., Barou, F. and Montagnat, M.: Microstructural evolution during thermal annealing of ice-Ih, Journal of Structural Geology, 99, 31–44, https://doi.org/10.1016/j.jsg.2017.05.001, 2017.

Hooke, R. L. and Hudleston, P. J.: Ice Fabrics in a Vertical Flow Plane, Barnes Ice Cap, Canada, Journal of Glaciology, 25(92), 195–214, doi:10.3189/S0022143000010443, 1980.

Hooke, R. L. and Hudleston, P. J.: Ice fabrics from a borehole at the top of the south dome, Barnes Ice Cap, Baffin Island, Geological Society of America Bulletin, 92(5), 274–281, https://doi.org/10.1130/0016-7606(1981)92<274:iffaba>2.0.co;2, 1981.

Humphreys, F. J. and Hatherly, M. (2nd Eds.): Recrystallization and related annealing phenomena, Elsevier, 2004.

Jafari, M. and Najafizadeh, A.: Correlation between Zener–Hollomon parameter and necklace DRX during hot deformation of 316 stainless steel, Materials Science and Engineering A, 501, 16–25, https://doi.org/10.1016/j.msea.2008.09.073, 2009.

Jessell, M. W.: Grain boundary migration and fabric development in experimentally deformed octachloropropane, Journal of Structural Geology, 8, 527–542, https://doi.org/10.1016/0191-8141(86)90003-9, 1986.

Journaux, B., Chauve, T., Montagnat, M., Tommasi, A., Barou, F., Mainprice, D. and Gest, L.: Recrystallization processes, microstructure and crystallographic preferred orientation evolution in polycrystalline ice during high-temperature simple shear, The Cryosphere, 13, 1495–1511, https://doi.org/10.5194/tc-13-1495-2019, 2019.

Kamb, W. B.: Ice petrofabric observations from Blue Glacier, Washington, in relation to theory and experiment, Journal of Geophysical Research, 64, 1891–1909, https://doi:10.1029/JZ064i011p01891, 1959.

Kamb, B.: Basal Zone of the West Antarctic Ice Streams and its Role in Lubrication of Their Rapid Motion, American Geophysical Union (AGU), Washington, D. C., 2008.

Kirby, S. H., Durham, W. B., Beeman, M. L., Heard, H. C. and Daley, M. A.: Inelastic properties of ice 1h at low temperatures and high pressures, J. Phys. Colloques, 48, C1–227–C1–232, https://doi.org/10.1051/jphyscol:1987131, 1987.

Kopp, R. E., DeConto, R. M., Bader, D. A., Hay, C. C., Horton, R. M., Kulp, S., Oppenheimer, M., Pollard, D. and Strauss, B. H.: Evolving Understanding of Antarctic Ice-Sheet Physics and Ambiguity in Probabilistic Sea-Level Projections, Earth's Future, 5, 1217–1233, https://doi.org/10.1002/2017ef000663, 2017.

Langdon, T. G.: A unified approach to grain boundary sliding in creep and superplasticity, Acta Metallurgica et Materialia, 42, 2437–2443, https://doi.org/10.1016/0956-7151(94)90322-0, 1994.

Langdon, T. G.: Grain boundary sliding revisited: Developments in sliding over four decades, J Mater Sci, 41, 597–609, https://doi.org/10.1007/s10853-006-6476-0, 2006.

Langdon, T. G.: Seventy-five years of superplasticity: historic developments and new opportunities, J Mater Sci, 44, 5998–6010, https://doi.org/10.1007/s10853-009-3780-5, 2009.

Lauridsen, E. M., Poulsen, H. F., Nielsen, S. F. and Juul Jensen, D.: Recrystallization kinetics of individual bulk grains in 90% cold-rolled aluminium, Acta Materialia, 51, 4423–4435, https://doi.org/10.1016/s1359-6454(03)00278-7, 2003.

Little, T. A., Prior, D. J., Toy, V. G. and Lindroos, Z. R.: The link between strength of lattice preferred orientation, second phase content and grain boundary migration: A case study from the Alpine Fault zone, New Zealand, Journal of Structural Geology, 81(C), 59–77, https://doi.org/10.1016/j.jsg.2015.09.004, 2015.

MacDonald, J. M., Wheeler, J., Harley, S. L., Mariani, E., Goodenough, K. M., Crowley, Q. and Tatham, D.: Lattice distortion in a zircon population and its effects on trace element mobility and U–Th–Pb isotope systematics: examples from the Lewisian Gneiss Complex, northwest Scotland, Contrib Mineral Petrol, 166, 21–41, https://doi.org/10.1007/s00410-013-0863-8, 2013.

Mellor, M. and Cole, D. M.: Stress/strain/time relations for ice under uniaxial compression, Cold Regions Science and Technology, 6, 207–230, https://doi.org/10.1016/0165-232x(83)90043-5, 1983.

Montagnat, M. and Duval, P.: Rate controlling processes in the creep of polar ice, infuence of grain boundary migration associated with recrystallization, Earth and Planetary Science Letters, 183, 179–186, https://doi.org/10.1016/s0012-821x(00)00262-4, 2000.

Montagnat, M., Azuma, N., Dahl-Jensen, D., Eichler, J., Fujita, S., Gillet-Chaulet, F., Kipfstuhl, S., Samyn, D., Svensson, A. and Weikusat, I.: Fabric along the NEEM ice core, Greenland, and its comparison with GRIP and NGRIP ice cores, The Cryosphere, 8, 1129–1138, https://doi.org/10.5194/tc-8-1129-2014, 2014.

Monz, M. E., Hudleston, P. J., Prior, D. J., Michels, Z., Fan, S.., Negrini, M., and Langhorne, P.: Electron backscatter diffraction (EBSD) based determination of crystallographic preferred orientation (CPO) in warm, coarse-grained ice: a case study, Storglaciären, Sweden, The Cryosphere Discuss, https://doi.org/10.5194/tc-2020-135, 2020.

Morawiec, A.: Misorientation-Angle Distribution of Randomly Oriented Symmetric Objects, J Appl Crystallogr, 28, 289–293, https://doi.org/10.1107/s0021889894011088, 1995.

Morland, L. W. and Staroszczyk, R.: Ice viscosity enhancement in simple shear and uni-axial compression due to crystal rotation, International Journal of Engineering Science, 47, 1297–1304, https://doi.org/10.1016/j.ijengsci.2008.09.011, 2009.

Obbard, R., Baker, I. and Sieg, K.: Using electron backscatter diffraction patterns to examine recrystallization in polar ice sheets, Journal of Glaciology, 52, 546–557, https://doi.org/10.3189/172756506781828458, 2006.

Piazolo, S., Montagnat, M. and Blackford, J. R.: Sub-structure characterization of experimentally and naturally deformed ice using cryo-EBSD, Journal of Microscopy, 230, 509–519, https://doi.org/10.3189/172756506781828458, 2008.

Pieri, M., Burlini, L., Kunze, K., Stretton, I. and Olgaard, D. L.: Rheological and microstructural evolution of Carrara marble with high shear strain: results from high temperature torsion experiments, Journal of Structural Geology, 23, 1393–1413, https://doi.org/10.1016/s0191-8141(01)00006-2, 2001.

Placidi, L., Greve, R., Seddik, H. and Faria, S. H.: Continuum-mechanical, Anisotropic Flow model for polar ice masses, based on an anisotropic Flow Enhancement factor, Continuum Mech. Thermodyn., 22, 221–237, https://doi.org/10.1007/s00161-009-0126-0, 2010.

Pollard, D.: A retrospective look at coupled ice sheet–climate modeling, Climatic Change, 100, 173–194, https://doi.org/10.1007/s10584-010-9830-9, 2010.

Ponge, D. and Gottstein, G.: Necklace formation during dynamic recrystallization: Mechanisms and impact on flow behavior, Acta Materialia, 46, 69–80, https://doi.org/10.1016/s1359-6454(97)00233-4, 1998.

Raj, R. and Ashby, M. F.: On grain boundary sliding and diffusional creep, Metallurgical Transactions, 2, 1113–1127, https://doi:10.1007/BF02664244, 1971.

Rutter, E. H. and Brodie, K. H.: The role of tectonic grain size reduction in the rheological stratification of the lithosphere, Geol Rundsch, 77, 295–307, https://doi.org/10.1007/bf01848691, 1988.

Sakai, T., Belyakov, A., Kaibyshev, R., Miura, H. and Jonas, J. J.: Dynamic and post-dynamic recrystallization under hot, cold and severe plastic deformation conditions, Progress in Materials Science, 60, 130–207, https://doi.org/10.1016/j.pmatsci.2013.09.002, 2014.

Schmid, S. M., Boland, J. N. and Paterson, M. S.: Superplastic flow in finegrained limestone, Tectonophysics, 43, 257-291, https://doi.org/10.1016/0040-1951(77)90120-2, 1977.

Seidemann, M., Prior, D. J., Golding, N., Durham, W. B., Lilly, K., and Vaughan, M. J.: The role of kink boundaries in the deformation and recrystallisation of polycrystalline ice, Journal of Structural Geology, 136, 104010, https://doi.org/10.1016/j.jsg.2020.104010, 2020.

Shigematsu, N., Prior, D. J. and Wheeler, J.: First combined electron backscatter diffraction and transmission electron microscopy study of grain boundary structure of deformed quartzite, Journal of Microscopy, 224, 306–321, http://doi:10.1111/j.1365-2818.2006.01697.x, 2006.

Spiers, C. J.: Fabric development in calcite polycrystals deformed at 400° C, Bulletin de Minéralogie, 102, 282–289, https://doi.org/10.3406/bulmi.1979.7289, 1979.

Underwood, E. E., Quantitative Stereology for Microstructural Analysis, in McCall, J. L., and Mueller, W. M., eds., Microstructural Analysis: Tools and Techniques: Boston, MA, Springer US, p. 35-66, 1973.

Weikusat, I., Kuiper, E.-J. N., Pennock, G. M., Kipfstuhl, S. and Drury, M. R.: EBSD analysis of subgrain boundaries and dislocation slip systems in Antarctic and Greenland ice, Solid Earth, 8, 883–898, https://doi.org/10.5194/se-8-883-2017, 2017.

Wheeler, J., Prior, D., Jiang, Z., Spiess, R. and Trimby, P.: The petrological significance of misorientations between grains, Contrib Mineral Petrol, 141(1), 109–124, https://doi.org/10.1007/s004100000225, 2001.

Wilson, C. J. L., Peternell, M., Piazolo, S. and Luzin, V.: Microstructure and fabric development in ice: Lessons learned from in situ experiments and implications for understanding rock evolution, Journal of Structural Geology, 61, 50–77, https://doi.org/10.1016/j.jsg.2013.05.006, 2014.

Wilson, C. J. L., Peternell, M., Hunter, N. J. R. and Luzin, V.: Deformation of polycrystalline D2O ice: Its sensitivity to temperature and strain-rate as an analogue for terrestrial ice, Earth and Planetary Science Letters, 532, 115999, https://doi:10.1016/j.epsl.2019.115999, 2020.

8 Modifications to “Tables”

8.1 Add new data of repeat-counted grains and number density of “distinct” grains in Table 3.

8.2 Add new cone opening-angle data from Hooke and Hudleston (1981) in Table 4.

9 Modifications to “Figures”

9.1 Remove Fig. 6, 7, 8.

9.2 Add *Fig. 2* -microstructure of undeformed ice sample

9.3 Add misorientation data to *Fig. 4-6*.

9.4 Add detailed misorientation analyse of “core-and-mantle” structure in *Fig. 7*.

9.5 Add distribution of grain size, subgrain size and number density of “distinct” grains as a function of strain in *Fig. 11*.

9.6 Add CPO data of randomly selected small grains with the same number of big grains in *Fig. 12*.

9.7 Add natural ice data from Hooke and Hudleston (1981) to *Fig. 13*.

9.8 Remove bulging in *Fig. 14*.

Temperature and strain controls on ice deformation mechanisms: insights from the microstructures of samples deformed to progressively higher strains at -10, -20 and -30 °C

Sheng Fan[1], Travis Hager[2], David J. Prior[1], Andrew J. Cross[2,3], David L. Goldsby[2], Chao Qi[4], Marianne Negrini[1], John Wheeler[5]

[1] Department of Geology, University of Otago, Dunedin, New Zealand
[2] Department of Earth and Environmental Science, University of Pennsylvania, Philadelphia, PA, USA
[3] Department of Geology and Geophysics, Woods Hole Oceanographic Institution, Woods Hole, MA, USA
[4] Key laboratory of Earth and Planetary Physics, Institute of Geology and Geophysics, Chinese Academy of Sciences, Beijing, China
[5] Department of Earth and Ocean Sciences, University of Liverpool, Liverpool, UK

Correspondence to: Sheng Fan (sheng.fan@postgrad.otago.ac.nz).

Abstract In order to better understand ice deformation mechanisms, we document the microstructural evolution of ice with increasing strain. We include data from experiments at relatively low temperatures (-20 and -30 °C), where the microstructural evolution with axial strain has never before been documented. Polycrystalline pure water ice was deformed under a constant displacement rate (strain rate ~$1.0 \times 10^{-5}\ s^{-1}$) to progressively higher strains (~3, 5, 8, 12 and 20%) at temperatures of -10, -20 and -30 °C. Microstructural data are generated from cryogenic electron backscattered diffraction (cryo-EBSD) analyses. All deformed samples contain sub-grain (low-angle misorientations) structures with misorientation axes that lie dominantly in the basal plane suggesting the activity of dislocation creep (glide primarily on the basal plane), recovery and subgrain rotation. Grain boundaries are lobate in all experiments suggesting the operation of strain induced grain boundary migration (GBM). Deformed ice samples are characterised by interlocking big and small grains and are, on average, finer grained than undeformed samples. Misorientation analyses between nearby grains in the 2-D EBSD maps are consistent with some 2-D grains being different limbs of the same irregular grain in the 3-D volume. The proportion of repeated (i.e. interconnected) grains is greater in the higher-temperature experiments suggesting that grains have more irregular shapes, probably because GBM is more effective at higher temperatures. The number of grains per unit area (accounting for multiple occurrences of the same 3-D grain) are higher in deformed samples than undeformed samples, and this increases with strain, suggesting that nucleation is involved in recrystallisation. “Core-and-mantle” structures (rings of small grains surrounding big grains) occur in -20 and -30 °C experiments, suggesting that subgrain rotation recrystallization is active. At temperatures warmer than -20 °C, *c*-axes develop a crystallographic preferred orientation (CPO) characterized by a cone (i.e., small circle) around the compression axis. We suggest the *c*-axis cone forms via the selective growth of grains in easy slip orientations (i.e., ~45° to shortening direction) by GBM. The opening-angle of the *c*-axis cone decreases with strain, suggesting strain-induced GBM is balanced by grain rotation. Furthermore, the opening-angle of the *c*-axis cone decreases with temperature. At -30 °C, the *c*-

axis CPO changes from a narrow cone to a cluster, parallel to compression, with increasing strain. This closure of the *c*-axis cone is interpreted as the result of a more active grain rotation together with a less effective GBM. We suggest that lattice rotation facilitated by intracrystalline dislocation glide on the basal plane is the dominant mechanism controlling grain rotation. Low-angle neighbour-pair misorientations, relating to subgrain boundaries, are more extensive and extend to higher misorientation angles at lower temperatures and higher strains supporting a relative increase in importance of dislocation activity. As the temperature decreases, the overall CPO intensity decreases, primarily because the CPO of small grains is weaker. High-angle grain boundaries between small grains have misorientation axes that have distributed crystallographic orientations. This implies that, in contrast to subgrain boundaries, grain boundary misorientation is not controlled by crystallography. Grain boundary sliding of finer grains or nucleation of those grains in random orientations (“spontaneous” nucleation) could explain the weaker CPO of the fine-grained fraction and the lack of crystallographic control on high-angle grain boundaries.

1 Introduction

Glaciers and ice sheets play key roles in shaping planetary surfaces, and form important feedbacks with climate, both on Earth (Hudleston, 2015; Pollard, 2010; Kopp et al., 2017) and elsewhere in the solar system (Hartmann, 1980; Whalley and Azizi, 2003). Understanding the controls on the flow rate of terrestrial glaciers and ice sheets is crucial, as this will be a major control on future sea level change (Bindschadler et al., 2013; Dutton et al., 2015; Bamber et al., 2019). Ice core studies and field investigations suggest the temperature of ice in Antarctica and Greenland ranges between ice melting temperature and ~-30 °C (Kamb, 2008; Montagnat et al., 2014; Kuiper et al., 2019a, 2019b). Glacial flow is driven by gravity and facilitated by both basal sliding along the ice-bedrock interface (including the shearing of subglacial till deposits) and the internal creep of ice masses. The contribution of creep deformation to the total flow rate is controlled primarily by differential stress and temperature within the ice body (Rignot et al., 2011; Hudleston, 2015). Creep experiments show a change in the mechanical behaviour as initially isotropic polycrystalline ice is deformed (Budd and Jacka, 1989; Faria et al., 2014; Hudleston, 2015). Mechanical weakening occurs during the transition from secondary creep (minimum strain rate) to tertiary creep (quasi-constant strain rate) in constant load experiments (e.g., Budd and Jacka, 1989; Montagnat et al., 2015; Hudleston, 2015; Wilson et al 2014) and from peak stress to steady-state stress in constant displacement experiments (e.g., Weertman, 1983; Durham et al., 1983, 2010; Vaughan et al., 2017; Qi et al., 2017). This mechanical weakening is often referred to as strain rate “enhancement” in the glaciological and ice sheet literature (Budd and Jacka, 1989; Alley, 1992; Placidi et al., 2010; Treverrow et al 2012; Budd et al., 2013). Enhancement correlates with the development of a crystallographic preferred orientation (CPO) (Jacka and Maccagnan, 1984; Vaughan et al., 2017) and also with other microstructural changes, particularly those associated with dynamic recrystallization (Duval, 1979; Duval et al., 2010; Faria et al., 2014; Montagnat et al., 2015), including grain size reduction (Craw et al., 2018; Qi et al., 2019). Understanding the deformation and recrystallization mechanisms responsible for ice microstructure and CPO development is therefore essential for quantifying how different mechanisms contribute to ice creep enhancement in nature. The relative roles of intracrystalline plasticity, recrystallization and grain size sensitive mechanisms, especially at low temperatures, are not well known.

In this contribution we present microstructural analyses of samples deformed to successively higher strains through the transition from peak stress to flow stresses at -10, -20 and -30 °C. These conditions were chosen so that the experiments included evolution of CPO towards a cone (small circle, centred on the compression direction) that occurs at high temperature and towards a cluster (maximum parallel to the compression direction) at low temperature. Our results include microstructural data from samples deformed to progressively higher strains at -20 and -30 °C. Such data have not been presented before, and they are important, as understanding how and why different CPOs develop as a function of temperature should give a better insight into the mechanisms that control CPO development and mechanical behaviour. Furthermore, understanding CPOs in nature requires extrapolation of laboratory results to the much lower strain rates that occur in nature. To do this effectively we need to know how CPOs evolve across as wide a range of temperatures and strain rates as is possible. In this paper our objectives are to study the influences of temperature and strain on microstructure and CPO development and to discuss implications for mechanical behaviour.

2 Methods

2.1 Sample fabrication

Dense, polycrystalline ice samples were prepared by the flood-freeze (standard ice) method (Cole, 1979; Durham et al., 1983; Stern et al., 1997) to meet the requirements of controlled grain size, random CPO and minimised porosity. We crushed ice cubes made from frozen Milli-Q water (ultra-pure water), into ice powders. These ice powders were then sieved at -30 °C in a chest freezer, to limit the particle sizes to 180 to 250 μm. Particles were then packed into the bottom of lightly greased stainless-steel cylindrical moulds (inner diameter 25.4 mm) to achieve a porosity of ~40%. A perforated brass spacer was placed on top of the packed ice power and the mould was sealed with a double O-ring plug. Air was removed from pore spaces with a vacuum pump after the moulds were equilibrated at 0 °C in a water-ice bath for 40 minutes. Degassed Milli-Q water (0 °C) was then flooded into the pore spaces. The perforated spacer prevents ice particles from floating in the water. After flooding, the moulds were transferred to a -30 °C chest freezer and placed vertically into cylindrical holes in a polystyrene block, with the base of moulds touching a copper plate at the bottom of the freezer. This ensures that freezing front migrates slowly upwards. After 24 hours the ice samples were gently pushed out using an Arbor press. Both ends of the cylindrical samples were cut and polished to be flat, parallel with one another, and perpendicular to the sample's long axis—at this point, the length of each sample was recorded (Table 1). Each sample was encapsulated in a thin-walled indium jacket (~0.38 mm wall thickness), the bottom of which had already been welded (melted) to a stainless-steel end-cap. After that, the top of each indium tube was welded to a steel semi-internal force gauge, with an insulating zirconia spacer placed between the force gauge and sample. The sample was kept cold in a -60 °C ethanol bath (Qi et al., 2017) during welding.

2.2 Experimental set up and process

We conducted axial compression experiments at the Ice Physics Laboratory, University of Pennsylvania. Experiments were conducted at a nitrogen gas confining pressure of ~20 ± 0.5 MPa at temperatures of -10, -20, and -30°C (±0.5°C), in a cryogenic, gas-medium apparatus (Durham et al., 1983; Heard et al., 1990). Samples were left to thermally equilibrate with the apparatus for more than 60 minutes before deformation started. Deformation experiments were performed at a constant axial displacement rate, giving an initial constant strain rate of ~1.0×10^{-5} s^{-1}. The experiments were terminated once final axial true strains of ~3%, 5%, 8%, 12% and 20% were achieved. After that, the ice samples were immediately extracted from the apparatus, photographed and measured. To minimize thermal cracking, samples were progressively cooled to ~ -30, -100 and -196 °C over about 15 minutes, and thereafter stored in a liquid nitrogen dewar. Typical time between the end of the experiments and the start of cooling was between 10 and 30 minutes. Minor static recovery of the ice microstructures may happen on this timescale (Hidas et al., 2017), but significant change in CPO or grain size is unlikely.

2.3 Mechanical data processing

During each experimental run, time, displacement and load were recorded once every five to seven seconds. The axial stress was calculated from the load divided by cross-sectional area of the ice sample and is corrected for the change of sample cross-sectional area, calculated by assuming constant sample volume during the deformation. The sample length $L(t)$ at time t is calculated from the displacement and the initial sample length (L_0). From this we calculate the axial stretch (λ: Eq. (1)) and the true axial strain (ε: Eq. (2)) (Hobbs et al., 1976).

$$\lambda = \frac{L(t)}{L_0} \tag{1}$$

$$\varepsilon = -\ln(\lambda) \tag{2}$$

2.4 Cryo-EBSD data

The relatively recent development of cryo-EBSD technique (Illiescu et al., 2004, Obbard et al., 2006; Piazolo et al., 2008) enables measurement of full crystallographic orientations. EBSD maps provide quantitative microstructural data, with significant detail in ice samples with large sizes up to about 70 mm by 40 mm (Prior et al., 2015). We prepared the ice samples and acquired the cryo-EBSD data following the procedures described by Prior and others (2015). Samples were cut in half along the cylindrical long-axis using a band saw in a -20 °C cold room and a ~5 mm slice was cut from half of the sample. One side of the slice, at a temperature of ~-30 to -50 °C, was placed against a copper ingot (70 mm by 35 mm) at ~5 °C. As soon as a bond formed between the ice sample and the ingot, the samples were placed in a polystyrene sample transfer box (~-100 °C). We acquired a polished sample surface for cryo-EBSD by hand lapping on grit paper. The samples were polished at ~-40 °C using grit sizes of 80, 240, 600, 1200 and 2400. The sample-ingot assemblies were then transferred to the polystyrene sample transfer box and cooled to close to liquid nitrogen temperature, before they were transferred into the SEM for the collection of cryo-EBSD data.

EBSD data were acquired using a Zeiss Sigma VP FEGSEM combined with a NordlysF EBSD camera from Oxford Instruments. We used pressure cycling in the SEM chamber remove frost and create a damage-free sample surface (Prior et al., 2015). EBSD data were acquired at a stage temperature of ~-95 °C, with 5-7 Pa nitrogen gas pressure, 30kV accelerating voltage and ~60 nA beam current. For each ice sample, we collected a reconnaissance map with a step size of 30 μm from the whole section and a map with the step size of 5 μm, from a selected sub-area, for detailed microanalysis (mapped areas listed in Table 2). We acquired and montaged the raw EBSD data by using Oxford Instruments' Aztec software. Details on the raw EBSD data have been summarized in Table 2. The angular resolution (error of crystallographic orientation measurement for each pixel) of the EBSD data is ~0.5°.

2.5 Processing of the cryo-EBSD data

Grain size, grain shape, grain boundary morphology, and CPO provide useful information for inferring ice deformation processes. We quantified these microstructural parameters (among others) from raw EBSD data using the MTEX toolbox (Bachmann et al., 2011; Mainprice et al., 2015) in MATLAB.

2.5.1 Grain size and subgrain size

Ice grains were reconstructed from the raw EBSD pixel maps with 5 μm step size using the MTEX algorithm of Bachmann and others (2011) with a grain boundary threshold of 10°. Grains with area equivalent diameters lower than 20 μm were removed from the data. No pixel interpolation was applied to the EBSD pixel map, preserving any non-indexed space. Deformed ice is often characterised by a development of subgrain boundaries where the misorientations between neighbouring pixels are lower than the misorientation angle threshold of grain boundaries (e.g. Montagnat et al., 2015; Weikusat et al., 2017). An ice grain can be separated into several subgrains by one or more subgrain boundaries. We calculated subgrain size using boundary misorientation thresholds of ≥ 2°. Grain size and subgrain size were calculated as the diameter of a circle with the area equal to the measured area of each grain or subgrain. Note that grain size or subgrain sizes represent the sizes of 2-D cross sections through 3-D grains.

The 2-D measurements of a grain will always underestimate the 3-D size. It is also possible that grains, with irregular 3-D geometries, could be appear as two or more separate grains in the same 2-D slice (Monz et al., 2020). To assess these stereological issues, we have analysed the maps with some 1-D lines; the comparison of 1-D and 2-D giving some insights (Cross et al., 2017a) as to the effects of taking a 2-D slice through a 3-D volume (section S3 of supplementary material). We have also assessed how many grains are in the same orientation on a 2-D slice. Grains (in 2-D) that are in the same orientation (they have a misorientation below a defined threshold) and in reasonable proximity (that depends on grain size) are candidates for being 2-D slices through the same grain that has an irregular geometry in 3-D. These analyses are presented in section S3 of the supplementary material.

2.5.2 Crystallographic preferred orientation

The EBSD maps with 5 μm and 30 μm step size have been used to generate the crystallographic preferred orientation (CPO) data with one point per pixel. The CPO data were contoured with a half-width of 7.5° based on the maximum of multiples of a uniform distribution (MUD) of the points, to more clearly show the CPO patterns. CPO intensity was quantified using the M-index of Skemer and others (2005). M-indices and eigenvectors (orientation and magnitude) are consistent between CPOs generated from the EBSD maps with 30 μm and 5 μm step sizes.

Ice CPOs formed during uniaxial compression at high temperatures are often characterised by *c*-axes aligning in an open cone (i.e., a small circle) (Fig. 1(a)), around the compression axis (Kamb, 1972; Jacka and Maccagnan, 1984; Wilson et al., 2014; Jacka and Li, 2000; Qi et al., 2017). The opening-angle, θ, of *c*-axes cone is considered important in indicating the relative activity of grain rotation and grain boundary migration (GBM), which are competing processes in deforming ice (Piazolo et al., 2013; Qi et al., 2017). In order to quantify cone opening-angles, we counted the number of *c*-axes that lie at a given angle (co-latitude) from the compression axis—this method is adapted from Jacka and Maccagnan (1984) and Piazolo et al. (2013). In practice we counted the *c*-axes between two co-latitudes separated by a 4° interval (selected by trial, see section S1 of the supplementary material) and calculated the MUD for this co-latitude range to plot on a graph of MUD as a function of co-latitude (Fig. 1(b-c)).

2.5.3 Misorientation

Deformation processes may leave signatures in misorientation data (Fliervoet et al., 1999; Wheeler et al., 2001, 2003; Montagnat et al., 2015; Qi et al., 2017). Misorientation describes the rotation axis and angle required to map one lattice orientation onto another (Wheeler, et al., 2001). Because of crystal symmetry, there is more than one rotation that can be used to describe a misorientation. We chose the minimum rotation angle and corresponding rotation axis to describe misorientation (i.e., the disorientation, in the material science nomenclature—Grimmer, 1979; Morawiec 1995; Wheeler et al., 2001). Here we refer to the minimum rotation angle and corresponding rotation axis as the misorientation angle and misorientation axis, separately. Misorientation angle distributions are illustrated as histograms; misorientation axes distributions are illustrated as inverse pole figures. In this study, we applied three groups of pixel-by-pixel misorientation analyses, using the EBSD data with 5 μm step size:

(1) Neighbour-pair misorientations: using neighbouring pixels.

(2) Random-pair misorientations: using randomly selected pixels.

(3) Grain boundary misorientations: using pixels along the grain boundaries of neighbouring grains.

3 Results

3.1 Starting material

Undeformed samples exhibit a foam-like microstructure with straight or slightly curved grain boundaries and polygonal grain shapes (Fig. 2(a)). The grain size distribution is slightly skewed. The frequencies of grains increase slightly from the minimum cut off grain size (20 μm) to a peak at around 300 μm, and then decrease with further increasing grain size (Fig. 2(b)). Mean and median grain sizes are 297 μm and 291 μm, respectively (Table 3). The mean and median subgrain sizes at 291 and 280 μm, respectively, are very close to mean and median grain sizes (Table 3), indicating that there are very few subgrain boundaries. CPO is close to random (Fig. 2(c)), with an M-index of ~0.004 (Table 2). Neighbour-pair and random-pair misorientation angle distributions both resemble the distribution calculated for randomly oriented hexagonal crystals (Fig. 2(d), Morawiec, 1995; Wheeler et al., 2001).

3.2 Mechanical data

Stress-strain curves are plotted in Fig. 3. Imposed initial strain rate and temperature are shown in Table 1 together with peak and final stresses and corresponding strain rates. The strain rate increases slightly with strain (Table 1), as is required kinematically for a shortening sample at constant displacement rate. For all the deformation runs, stress initially increases as a function of strain, before reaching a peak stress at axial strains of $0.01 \leq \varepsilon \leq 0.04$. Beyond the peak stress, stress deceases with increasing strain, with the rate of stress drop decreasing with increasing strain. The rate of stress reduction is at a minimum, for each temperature, at strains larger than ~0.1. Peak and final stresses are larger at colder temperatures. Ratios of peak stress to stresses at higher strain (e.g. final stress of ~20% strain) are approximately the same at all temperatures so that all curves, when normalised to the peak stress look similar.

3.3 Microstructure

EBSD data are used to generate the illustrative grain orientation maps, grain sub-structure maps, grain size distributions, subgrain size distributions and misorientation angle distributions shown in Figs. 4-6. The grain size and subgrain size distributions are presented as histograms with 4 μm bins. We only show selected areas of EBSD maps so that the reader can resolve microstructural features. Quantitative microstructural analyses are based on much larger areas than those presented in the figures (Table 2).

3.3.1 Sub-structure

All samples deformed at -10 °C and -20 °C show large, lobate grains interlocking with finer, less lobate grains (Fig. 4(a-b), 5(a-b)). Grain boundary lobateness increases at higher strains. The scale of lobateness—that is, the amplitude of grain boundary irregularities—is smaller at -20 °C than -10 °C. At -30 °C lobate grain boundaries are less common at low strains but are a common attribute of larger grains at 20% strain (Fig. 6(a-b)). Samples deformed at -20 °C and -30 °C to strains higher than

~12% show a “core-and-mantle” structure (Gifkins, 1976; White, 1976; Ponge and Gottstein, 1998), characterised by a “net” or “necklace” of finer grains encircling larger grains.

Distinct sub-grain boundaries can be observed in all the samples (Fig. 4 (c), 5 (c) and 6 (c)). Many of the subgrain boundaries appear to be straight, some with slight curvature. A small number have strong curvature. Interconnected subgrain boundaries can be observed in some of the grains. Subgrain boundaries subdivide grains into subgrains.

The colouring of the IPF maps changes with increasing strain, corresponding to the increasing strength of the CPO. At -10 °C, grains with near-pink-and-orange colours dominate the IPF maps at strains higher than ~8% (Fig. 4(a-b)). At -20 and -30 °C, grains with red, pink and orange colours dominate the IPF maps at ~20% strain (Fig. 5(a-b) and 6 (a-b)).

3.3.2 Grain size

For samples deformed to ~3% strain, the grain size distributions are strongly skewed or possibly bimodal, with a clear main peak at finer grain sizes and a tail of coarser sizes with a broad, poorly defined secondary peak corresponding to the mean grain size of the starting material (Fig. 4(d), 5(d) and 6(d)). As strain increases, the grain size distributions generally narrow and shift towards finer grain sizes (Fig. 3(d), 4(d) and 5(d)). The secondary peak, corresponding to the mean grain size of the starting material, becomes harder to see with increasing strain and is absent by 12% strain at all temperatures.

For each sample, we calculated the mean grain diameter ($\overline{D}$) and square mean root diameter ($D_{SMR} = (\overline{\sqrt{D}})^2$) and estimated the peak grain diameter (D_{peak}) by visual inspection of the distributions. D_{SMR} minimizes the bias from very large grains in the calculation of an average. To better describe the statistics of the skewed or bimodal grain size distributions, we also calculated median grain size (D_{median}), lower quartile ($D_{q,25\%}$) and higher quartile ($D_{q,75\%}$). Data are presented in Table 3. $\overline{D}$, D_{SMR}, D_{median} and D_{peak} have the relation of $\overline{D} > D_{SMR} > D_{median} > D_{peak}$, and converge as the strain increases (Fig. 4 (d), 5 (d), 6 (d) and Table 3).

We wish to compare the microstructures associated with different grain size populations. Ideally, we would like to distinguish the microstructural and CPO characteristics of recrystallised grains (i.e., grains formed during the experiment) and remnant grains (i.e., remnants of grains present in the starting material). While the mean diameter, $\overline{D}$, is commonly used to represent a characteristic sample grain size (e.g., Jacka and Maccagnan, 1984; Piazolo et al., 2013; Vaughan et al., 2017; Qi et al., 2017; Qi et al., 2019) it averages the recrystallised and remnant fractions. Lopez-Sanchez and Llana-Fúnez (2015) showed that the frequency peak (D_{peak}) of a grain size distribution provides a robust measure of the recrystallized grain size from the study of deformed rock samples. In our data, the population of grains smaller than D_{peak} is too small, in many samples, to provide representative data. Instead we define, for each temperature series, a threshold grain size, equal to the D_{SMR} of the sample deformed to ~12% strain. The grains with the grain sizes greater than the threshold are classified as “big” grains and grains smaller than or equal to the threshold are classified as “small” grains.

Stereological artefacts inevitably arise from looking at microstructures on two-dimensional sections. Here we analyse two distinct (albeit related) stereological issues. The first issue relates to the *misidentification* of “small” grains, as these could appear from slices cut close to the perimeter of a large grain in 3-D (Underwood, 1973). The second issue relates to the *oversampling* of grains that have highly irregular, branching shapes in 3-D and appear more than once on a 2-D surface (Hooke and Hudleston, 1980; Monz et al, 2020).

It is clear that 2-D grain size measurements will always underestimate the “true” 3-D grain size (Underwood, 1973; Berger et al., 2011). A trickier problem lies in understanding how, specifically, grain size distributions in two dimensions relate to those in three dimensions. As we have categorized grains in 2-D maps as “big” and “small” grain, we need to assess the likelihood of a “small” grain in 2-D being a slice through of a “big” grain in 3-D. One way to estimate this is to further flatten the two-dimensional data into one-dimension and measure grain sizes along a line. From this analysis, we can evaluate the likelihood that a “small” 1-D grain is indeed a “small” grain in 2-D. This analysis is presented in section S3 of the supplementary material. At ~20% strain the percentage of “small” grains on a 1-D line that correspond to “small” grains in the 2-D EBSD map is 64%, 76% and 43% at -30, -20 and -10 °C, respectively. These data suggest that at 20% strain the presence of “small” grains in 3-D is likely, with the confidence in this statement increasing at reduced temperatures. Another observation supports this: at 20% strain many “small” grains have “small” grain neighbours (Fig. 4-7). At -30 °C and -20 °C some “small” grains are entirely surrounded by other “small” grains. At -10 °C there are lines of “small” grains in contact along the boundary between “large” grains. It is very difficult (and at -30 °C impossible) to have all of these “small” grains linked to large grains in the third dimension whilst maintaining a microstructure (e.g. in an orthogonal plane) that looks like the microstructures in these maps. This is the case at 20% strain. At lower strains the percentage of “small” 1-D segments that correspond to “small” 2-D grains is lower so the confidence with which we can define “small” grains is reduced.

The linear intercept analyses described in the previous paragraph also allow a crude assessment of grain oversampling—in other words, how likely are we to measure a large, branching grain more than once? In all samples >90% of 2-D grains along an arbitrary line are unique (that is, they are cut only once). Of course, with lines in multiple directions the percentage of unique grains might decrease. Using EBSD crystal orientation data, we can assess the likelihood of nearby grains in the 2-D map belonging to the same grain in 3-D (Monz et al., 2020). For every grain identified within a given EBSD map, we searched for all the nearby grains misoriented by less than a 10°, within a 1mm radius. These thresholds probably overestimate the number of grains connected in 3D. 1mm is close to double of the size of the largest grain and 10° is more than twice the median and significantly larger than the higher quartile in mis2mean data (the misorientation angle between all pixels in a grain and the mean orientation of that grain) for all samples.

Full details are outlined in section S4 of the supplementary material and key outcomes are listed in Table 3. The percentage of “unique” grains (that only appear at the surface once) relative to all grains in a 2D map is higher than 68% at all temperatures and strains (Table S2, Table 3). The procedure outlined in the last paragraph allows us to estimate the number of “distinct” grains (where all 2-D grains attributed to the same 3-D grain are counted as one grain) in each map and from this, the number density (grain number per unit area) of “distinct” grains. The number density of “distinct” grains within all deformed samples at all temperatures is greater than 3 times that in the starting material: reaching values > 6 times the starting material at -10 °C and >11 times the starting material at lower temperatures (Fig. 11(c), Table 3). The number density of “distinct” grains is generally higher at strains of ε ≥~12% than at strains of ε ≤~8% at all temperatures, and it is generally higher in samples deformed at -20 and -30 °C than samples deformed at -10 °C (Fig. 11(c), Table 3).

The analyses above provide some confidence that in all the experiments the number density of grains has increased relative to the starting material and increases with strain. If we couple this to the grain size statistics presented and the analysis of whether we are misidentifying small grains, the weight of evidence suggests that we have a real population of smaller grains. Our confidence in this statement increases with reducing temperature and increasing strain. Now we come back to the issue of how we distinguish "big" and "small" grains. Our scheme for separating "big" and "small" grains, using D_{SMR} of the sample deformed to ~12% strain as the threshold, is not perfect, but it does provide a fast and repeatable way of looking at the possible differences in microstructures and CPO of smaller and larger grains. The grain size threshold chosen (peak, mean, median and SMR) to separate "big" and "small" grains has little impact on the CPOs of the "big" and "small" grain populations (see section S5 of the supplementary material).

3.3.3 Subgrain size

Subgrain size distributions (Fig. 4(e), 5(e) and 6(e)) are similar to the grain size distributions (Fig. 4(d), 5(d) and 6(d)), but the median and mean subgrain sizes are smaller than median and mean grain sizes (Table 3). In many cases, particularly at lower temperatures, the peak corresponds to the lower grain size resolution (cut off) indicating that we could be missing smaller subgrains. For this reason, the peak subgrain sizes are not useful and the median and mean subgrain sizes probably represent overestimates.

3.3.4 Misorientation

Misorientation angle distributions are presented for misorientations between 2° and 20° (Fig. 4(f), 5(f), 6(f)). Random-pair misorientation angle distributions show the misorientations expected for the measured CPO. It is important to identify differences between neighbour- and random-pair distributions, as these can be attributed to orientation inheritance, among other processes (Wheeler et al., 2001). Neighbour- and random-pair distributions at misorientation angles greater than 20° (not shown) are very similar in all samples, indicating that these are simply a function of the CPO. In all deformed samples there is a large peak at 2° in neighbour-pair data that is not present in random-pair data. The difference between neighbour-pair and random-pair frequency lessens as misorientation angle increases. The misorientation angle at which neighbour-pair frequency has reduced to be equal to the random-pair frequency increases with decreasing temperature. It is at 10° to 14° at -10°C and does not change substantially with strain. At -20°C this angle is 10° to 14° at low strain but increases to around 18°-20° at 12% and 20% strain. At -30°C this angle is 16° to 18° at 3% strain, 18° to 20° at 5% strain and 20° at higher strain.

Neighbour-pair misorientation axes at misorientation angles 5°-10° show primary maxima lying in the basal plane (Fig. 4 (g), 5(g), 6(g)) for all deformed samples. Misorientation axes below 5° are omitted from these plots as the axes have relatively high angular errors (Prior, 1999). Misorientation axes from 2°-5° (not shown for all: an example is in Fig. 8(c)) also lie dominantly in the basal plane but have lower intensities, which we attributed to higher angular error. Grain boundary (>10°)

misorientation axes for neighbouring grains are not strongly aligned. There is a very slight preference for misorientation axes lying in the basal plane (except PIL007) and this preference is slightly stronger at colder temperatures.

Figure 7 illustrates misorientation analyses of a typical “core-and-mantle” structure characterized by “small” grains (illustrated with thin boundaries) arranged along boundaries of “big” reference grains (ref1 to ref5 illustrated with thick boundaries) in sample PIL268 (-30 °C, ~20% strain). The *c*-axes of reference grains are dispersed in a complex way, with the *c*-axes within an individual reference grain varying by up to ~20°. The complex dispersions include some data that lie along great circles and maybe some small circles. Great circle dispersions indicate rotation axes in the basal plane, consistent with neighbour-pair misorientation axes of low angle boundaries, which have a primary maximum parallel with poles to *m*-planes ([-1100]) (Fig. 7(c)). The *c*-axes of “small” grains are dispersed around the *c*-axes of “big” reference grains (Fig. 7(b)); the small grains occupy a much wider range of orientations than the large grains. Some of the small grains have *c*-axes within the single grain that are dispersed in a great circle smear, with up to ~5° of *c*-axis orientation variation. The distributions of misorientation axes between each of the reference grains and it’s neighbouring small grains show no particular pattern apart from an absence of misorientation axes close to [0001]. These are all high-angle (>10°) misorientation so the axis errors will be small (Prior, 1999). The boundary misorientation axes between neighbouring “small” grains are distributed relatively uniformly (Fig. 7(d)), apart from an absence of data close to [0001].

3.4 Crystallographic preferred orientations

The contoured *c*-axes, *a*-axes and poles to *m*-planes pole figures are illustrated in Fig. 8-10. The *c*-axes figures are presented with (1) the compression axis vertical and (2) with the compression axis perpendicular to the page. These two reference frames, which are commonly used by different communities, enable different elements of symmetry to be illustrated. At all temperatures CPO intensity increases with strain.

3.4.1 -10 °C series

The CPO of the sample (PIL176) deformed to ~3% strain at -10 °C is characterized by several weak maxima of *c*-axes with similar angles relative to the compression direction, and random distributions of *a*-axes and poles to *m*-planes. As the strain increases from ~5%, the CPO becomes clearer, with *c*-axes aligned in a cone (small circle). The cone is incomplete, with distinct maxima that are distributed along a small circle and individually elongated along the small circle trajectory. The *a*-axes and poles to *m*-planes align in a broad swath along the plane perpendicular to the compression axis and bound by the *c*-axis cone.

3.4.2 -20 °C series

The CPO of the sample (PIL183) deformed to ~3% strain at -20 °C is very weak. At ~5% strain (PIL182), the CPO is characterized by a blurred cone formed by several weak maxima of *c*-axes, and randomly distributed *a*-axes and poles to *m*-planes. As the strain increases from ~8% to ~12%, the CPO becomes clearer, with *c*-axes aligned in distinct clusters superposed on a blurred broad small circle cone. The *a*-axes and poles to *m*-planes align in weak a broad swath along the plane perpendicular to the compression axis and bound by the *c*-axis small cone. At ~20% strain, the *c*-axes align in two clusters that lie in a cone (small circle), and the *a*-axes and poles to *m*-planes align in broad swath along the plane perpendicular to the compression axis and bound by the *c*-axis small cone.

3.4.3 -30 °C series

The CPOs of the samples (PIL165, PIL162) deformed to ~3% and ~5% strain at -30 °C are very weak. As the strain increases from ~8% to ~12%, the *c*-axis CPO exhibits a pattern of a distinct narrow cone superposed on an overall broad cluster, the *a*-axes and poles to *m*-planes align in a broad swath along the plane perpendicular to the compression axis. At ~20% strain, the *c*-axes align in distinct clusters superposed on an overall broad cluster, and the *a*-axes and poles to *m*-planes align in a broad swath along the plane perpendicular to the compression axis and bound by the *c*-axis narrow cone.

3.4.4 CPOs of different grain size fractions

The “big” and “small” grains have similar patterns of *c*-axes (i.e. maxima in approximately the same places)—samples deformed to ~12% strain illustrate this (Fig. 12). The data are taken from smaller area maps (Table 2) with a 5 µm step size; the CPOs for all grains are comparable to data from larger areas using a 30 µm step size (compare Fig. 12a with Fig. 9-11), with CPOs from the 30 µm maps being slightly weaker. At -10 °C, the CPO intensity of “small” grains is slightly lower than “big” grains (Fig. 12(b-c)). This contrast becomes strengthened as the temperature decreases. At -30 °C the CPO intensity of “small” grains is much lower than “big” grains (Fig. 12(b-c)). CPO intensity is not significantly affected by the number of grains used to calculate M-index—we verified this by calculating M-index for a subpopulation of small grains, of the same size as the “big” grain population (Fig. 12(d)).

To show how CPO strength differs for “big” and “small” grains for the whole data set we plot the M-indices for the grain size categories against strain (Fig. 11(d)). For all the deformed samples, the M-indices of “big” grains have the same pattern with strain as the complete data set (all grains). The “small” grains generally have lower M-indices at strains of $\varepsilon \geq$ ~5%. The grain size threshold ($\overline{D}$, D_{SMR}, D_{median} and D_{peak}) chosen to separate “big” and “small” grains has a minor impact on CPO, with no significant change in CPO pattern or intensity (see section S5 of the supplementary material for the test).

3.4.5 The opening-angle of the *c*-axis cone

To increase our understanding of the processes that might control the *c*-axes cone opening-angle θ, we plotted data from this study and previous studies in a diagram of θ as a function of strai,n with data subdivided with different temperatures and strain rates (Table 4 and Fig. 13). For data from the literature, we digitised the *c*-axis orientations from published stereonets (Jacka and Maccagnan, 1984; Jacka and Li, 2000) and calculated θ using the same method described in Section two (Method). For data from Montagnat and others (2015) and Craw and others (2018), we measured the values of θ directly from contoured *c*-

axis CPO figures. For data from Vaughan and others (2017), we calculated the values of θ from raw EBSD data. The values of θ from Hooke and Hudleston (1981), Piazolo and others (2013), Qi and others (2017) and Wilson and others (2020) are taken directly from these papers. The experiments reported by Piazolo and others (2013) were conducted on D_2O ice at -7 °C, which is a direct analogue for deforming H_2O ice at −10 °C (Wilson et al., 2019). These angles were analysed using methods similar to ours. In order to make a direct comparison with the data reported from this study and Qi and others (2017), we converted the reported axial engineering strain (e) and strain rate ($\dot{e}$) (Piazolo et al., 2013; Montagnat et al., 2015; Vaughan et al., 2017) to true axial strain (ε) and strain rate ($\dot{\varepsilon}$) using the equations:

$$\varepsilon = -\ln(1-e) \tag{4}$$

$$\dot{\varepsilon} = \frac{\dot{e}}{1-e} \tag{5}$$

Equation (6) and (7) were used to forward model axial engineering strain (e) and strain rate ($\dot{e}$) from octahedral shear strain (γ) and strain rate ($\dot{\gamma}$) (Jacka and Maccagnan, 1984; Jacka and Li, 2000).

$$\gamma = \frac{\sqrt{2}}{3}\left(e + \frac{1}{\sqrt{1-e}} - 1\right) \tag{6}$$

$$\dot{\gamma} = \frac{\sqrt{2}}{3}\left(\frac{1}{2(1-e)^{\frac{3}{2}}} + 1\right)\dot{e} \tag{7}$$

After that, the axial engineering strain (e) and strain rate ($\dot{e}$) were converted to true axial strain (ε) and strain rate ($\dot{\varepsilon}$) using Eq. (4) and Eq. (5).

For natural ice samples (top of the south dome, Barnes Ice Cap, Baffin Island) from Hooke and Hudleston (1981), Eq. (8) was used to calculate axial engineering strain (e) from natural octahedral unit shear strain ($\bar{\gamma}_{oc}$). Values of $\bar{\gamma}_{oc}$ were taken from Fig. 4 of Hooke and Hudleston (1981) based on the assumption that ice was deformed under uniaxial compression. After that, the axial engineering strains (e) were converted to true axial strains (ε) using Eq. (4). Hooke and Hudleston (1981) assumed their natural ice samples were deformed under a constant vertical strain rate, $\dot{e}$, of $5.71 \times 10^{-11} s^{-1}$, which converted to true axial strain rate ($\dot{\varepsilon}$) using Eq. (5). The derivation of Eq. (4-8) are shown in section S2 of the supplementary material.

$$\bar{\gamma}_{oc} = \frac{2\sqrt{2}}{3}\left(e + \frac{1}{\sqrt{1-e}} - 1\right) \tag{8}$$

To our knowledge, Fig. 13 contains data from all published 3-D uniaxial compression ice experiments and deformed natural ice that present *c*-axis CPOs as a function of strain. 2-D experiments, involving deformation on a microscope stage (e.g. Peternell et al., 2014; Peternell and Wilson, 2016) are excluded as these have different kinematics. There are numerous other high temperature and low strain rate axial compression experiments to strains of ~10% to 30% where *c*-axis cones have opening-angles of ~35 degrees (e.g., Wilson and Russell-Head, 1982; Gao and Jacka, 1987; Treverrow et al., 2012; Wilson et al., 2019). These data are consistent with the pattern shown in Fig. 13 but are not part of a strain series and are not added to the diagram to maintain clarity. There are comparatively few CPOs from samples at low temperatures (< -15 °C) so we have included all published data from experiments at < -15 °C irrespective of whether these are part of a strain series. The values of

θ are scattered between 0° and 42° for all experiments. Experiments to low strains have random CPOs where a cone angle cannot be defined, and these data are not shown on Fig. 13. For experimental data, the evolution pattern of θ as a function of strain at temperatures warmer than -15 °C show θ decreases with increasing strain up to ~20% true axial strain. The only two data points of θ from samples deformed to the strain of ~50% are at 30°. There is little difference as a function of temperature at ≥ -15 °C. For natural ice deformed under temperatures of -4~-6 °C, θ generally decreases with increasing strain for both "coarse" ice (>0.15 cm^2) and "fine" ice (<0.1 cm^2).

Samples deformed at temperatures colder than -20 °C have lower θ values compared with samples deformed at warmer temperatures at similar strains. At -30 °C, the opening-angle of the *c*-axis cone decreases to ~0° at strains of ~20%. The strain corresponding to the formation of a clear *c*-axis cone (non-random CPO) increases with decreasing temperature.

4 Discussion

4.1 Deformation mechanisms

4.1.1 Inferences from mechanical evolution

All stress-strain curves (Fig. 3) show stress rising to the peak stress and then relaxing, with the rate of stress drop decreasing with strain. This pattern matches published constant-displacement-rate experiments (Mellor and Cole, 1982; Durham et al., 1983; Durham et al., 1992; Piazolo et al., 2013; Vaughan et al., 2017; Qi et al., 2017; Craw et al., 2018; Qi et al., 2019), and has an approximate inverse relationship (Mellor and Cole, 1982, 1983; Weertman, 1983) to constant-load experiments (Budd and Jacka, 1989; Jacka and Li, 2000; Treverrow et al, 2012; Wilson and Peternell, 2012) where strain rate first decreases to a minimum and then increases to approach a near-constant strain rate.

Stress-strain curves of all experimental runs show a smooth and continuous increase of stress as a function of strain before reaching the peak. Approximately linear portions of the stress-strain data prior to peak have been termed quasi-elastic (Kirby et al., 1987). Slopes of ~1GPa are significantly below the published value of Young's modulus (~9GPa: Gammon et al, 1983) and indicate that there is significant dissipative deformation here. This likely includes anelastic deformation related to intergranular stress redistribution used to explain primary creep in constant load experiments (Duval et al, 1983; Castelnau et al., 2008). The curvature of the stress strain line at the start of each experiment may relate to initial porosity loss as suggested by rapid increases in ultrasonic p-wave velocity in comparable experiments by Vaughan and others (2017).

As our experiments are all at the same approximate strain rate, we cannot calculate the stress dependency of strain rate (the stress exponent, n). Qi and others (2017) calculate a peak stress n value of 3 and flow stress n value of 3.9 for comparable experiments (including PIL007 used here) at -10 °C. Craw and others (2018) calculate a peak stress n value of 4.1 for comparable experiments at -30 °C. Our experiments show higher peak and final stress values at colder temperatures than at warmer temperatures. This phenomenon is well known, and the temperature dependence of creep rate is commonly parameterised using an Arrhenius relationship with an activation energy (Homer and Glen, 1978; Durham et al., 1983, 2010;

Budd and Jacka, 1989; Cuffey and Paterson, 2010; Scapozza and Bartelt, 2003). Our peak and final stress data can be used to calculate the activation energy by assumption of a value of stress exponent, n (see section S6 of the supplementary material for the calculation). Best fit to all data (-10, -20 and -30 °C) give activation energy of 98 kJ/mol and 103 kJ/mol from peak and final stress data assuming n=3 and 131 kJ/mol and 138 kJ/mol from peak and flow stress data assuming n=4. These numbers are consistent with published values (64-250 kJ/mol) at relatively high temperature (Glen, 1955; Goldsby, 2001; Budd and Jacka, 1989; Cuffey and Paterson, 2010; Durham et al., 2010; Kuiper et al., 2019a, 2019b).

4.1.2 Inferences from microstructure

4.1.2.1. Nucleation

The number density (number of grains per unit area) of "distinct" grains (counting 2-D grains attributed to the same 3-D grain as one: section S4 of supplementary material) increases by more than a factor of 3 times that of the starting material in all deformed samples at all temperatures (Table 3). We can be reasonably confident that the number of grains in the samples has increased as a function of deformation. This requires a process of nucleation to create new grains. For all the deformed samples, the grain size distributions are characterised by peaks at finer grain sizes, and a smaller mean/median grain size compared with the undeformed sample (Fig. 2, 4-6, Table 3). The smallest grains in the deformed samples were not present in the starting material. These observations suggest that nucleation generates the grains with smaller sizes. Grain number density generally increases and all measures of 2-D grain size decrease with strain (Table 3), at all temperatures, suggesting that nucleation operates continuously as part of the recrystallisation process throughout the deformation.

4.1.2.2. Dislocation activity, recovery, subgrain rotation and subgrain rotation recrystallisation

Microstructure maps show subgrain boundaries in all deformed ice samples (Fig. 4(a-c), 5(a-c) and 6(a-c)). The subgrain boundary geometry is comparable with other experimentally or naturally deformed rock and metal samples, e.g. quartz (Cross et al., 2017a; Killian and Heilbronner, 2017), Olivine (Hansen et al., 2012), Magnox alloy (Wheeler, 2009) and Zircon (MacDonald et al., 2013). The misorientation axes for subgrain boundaries are generally rotations around rational crystallographic axes, particularly directions in the basal plane, suggesting that the boundaries may represent arrays of dislocations (Humphreys and Hatherley, 2004; Shigematsu et al., 2006). There is much higher frequency of low angle (Particularly < 10°) neighbour-pair misorientations than are expected from the CPO (as shown by the random-pair misorientation angles). The subgrain boundaries and the pattern of misorientation angles are commonly interpreted as the result of dynamic recovery of dislocations generated during deformation and subsequent subgrain rotation related to ongoing recovery (Guillope and Poirier, 1979; Trimby et al., 1998; Fliervoet et al., 1999; Wheeler et al., 2001) and has been observed from ice deformation experiments previously and interpreted in this way (e.g. Montagnat et al., 2015; Qi et al., 2017; Seidemann at al., 2020). The misorientation angle at which neighbour-pair frequency has reduced to be equal to the random-pair frequency increases with decreasing temperature (Fig. 4 (f), 5(f), 6(f)). This observation suggest intragranular distortion is more significant at lower temperatures.

Subgrain rotation is a process that involves an increase in the misorientation across a subgrain boundary forming via the progressive addition of dislocations (White., 1979; Lallemant, 1985; Placidi et al., 2004). New grains will form as the misorientation across the subgrain boundary becomes large enough, with the subgrain boundary eventually dividing its parent grain (Poirier and Nicolas, 1975; Guillope and Poirier, 1979; Urai et al., 1986; Halfpenny et al., 2006; Gomez-Rivas et al., 2017). This process is known as the subgrain rotation recrystallization (Hirth and Tullis, 1992; Stipp et al., 2002; Passchier and Trouw, 2005). When subgrain rotation recrystallization is responsible for nucleation, the recrystallized “daughter” grains should be initially of a similar size to the internal subgrain size of the “parent” grain (Urai et al., 1986). At all temperatures and strains the mean/median subgrain size is smaller than the mean/median grain size. This indicates that the subgrain rotation recrystallization could be the nucleation mechanism that generates the “small” grain population. Previous studies on deformed metals and quartzites describe the structure of smaller grains encircling larger grains as “core-and-mantle” structure (Gifkins, 1976; White, 1976). The production of smaller grains that form the “mantle” region was considered as a result of continual rotation of subgrains to develop small strain free grains (White, 1976; Urai et al., 1986; Jacka and Li, 2000). The network of smaller grains that encircle bigger grains at strains higher than 12% at -20 and -30 °C is consistent with the operation of a subgrain rotation recrystallization mechanism. The network of finer grains encircling larger grains has been observed in deformed metals, and it is named as the “necklace structure” in the material science literature (e.g. Ponge and Gottstein, 1998; Jafari and Najafizadeh, 2009; Eleti et al., 2020). Lately, Eleti and others (2020) used a fiducial marker grid to show that the deformation of finer grains in the necklace structure includes a significant component of GBS.

All measures of grain and subgrain sizes are smaller at lower temperatures. This is likely a consequence of the higher stresses of the lower temperature experiments resulting in smaller subgrain and recrystallised grain sizes through a piezometer or similar relationship (Derby, 1991; Austin and Evans, 2007; Lopez Sanchez and Llana Funez, 2015; Cross et al., 2017a). Jacka and Li (1994) show an inverse relationship between ice grain size and stress from deformed ice samples that reach tertiary creep.

4.1.2.3. Grain boundary migration

Lobate grain boundaries are commonly interpreted as the result of strain-induced grain boundary migration (GBM) (Urai et al., 1986; Jessell, 1986; Duval and Castelnau., 1995). Samples deformed at -10 and -20 °C show more grains with lobate boundaries at higher strains (>~3%), suggesting more widespread strain-induced GBM with an increasing strain. The proportion of repeated (i.e. interconnected and highly lobate) grains is generally higher in the higher-temperature experiments (Table 2, section S4 of the supplementary material). This observation suggests that GBM is also more widespread at higher temperatures.

4.1.3 CPO development

The CPO intensity and opening-angle of the *c*-axis CPO decrease as the temperature drops. Previous studies suggest the CPO development is mainly controlled by the deformation and recrystallization mechanisms (Alley, 1992; Qi et al., 2017). Fig. 14 explains how key processes (Fig. 14(b)) involved in the deformation and recrystallization mechanisms (Fig. 14(a)) may affect the CPO development as a function of strain and temperature (Fig. 14(c)). Many deformed samples exhibit an incompleteness of *c*-axes cone (lack of cylindrical symmetry) (Fig. 8-10). The incompleteness of *c*-axes cone is more severe for 5 µm EBSD maps collected from a much smaller area than 30 µm EBSD maps (Fig. 12). These phenomena are common to all ice CPOs from measurements on a single sample planes (by EBSD or optical methods: see any of the papers cited), but are not so apparent in neutron diffraction data (Piazolo et al., 2013; Wilson et al., 2019), that sample a larger volume, suggesting that a single plane through a deformed sample does not generally contain sufficient grains for a fully representative CPO.

Our -10 °C series CPO data show a monotonic increase in CPO intensity as indicated by M-index, and a clearer cone-shaped pattern of the *c*-axes with increasing strain. Similar observations were made in previous ice deformation experiments (e.g. Jacka and Maccagnan, 1984; Piazolo et al., 2013; Montagnat et al., 2015; Vaughan et al., 2017; Qi et al., 2017). Cone-shaped *c*-axes CPOs have been related to strain-induced GBM favouring the growth of grains with easy slip orientations (high Schmid Factors) (Duval and Castelnau., 1995; Little et al., 2015; Vaughan et al., 2017; Qi et al., 2017). Linked to this is the idea that grains with hard slip orientations should have greater internal distortions (Duval and Castelnau., 1995; Bestmann and Prior 2003), and therefore store higher internal strain energy. If this is correct then hard slip grains are likely to be consumed by grains with easy slip orientations through GBM (Duval and Castelnau., 1995; Castelnau et al., 1996; Bestmann and Prior, 2003; Piazolo et al., 2006; Killian et al., 2011; Qi et al., 2017; Xia et al., 2018). However, we have to re-evaluate the detail of this idea, as recent studies on deformed ice samples show there is no systematic relation between orientation and strain localisation at low strain (Grennerat et al. 2012). Furthermore, studies of high-strain shear samples find no clear difference in the geometrically necessary dislocation density within the two maxima that develop in simple shear (Journaux et al. 2019). An alternative, and as yet incomplete, explanation from Kamb (1959) relates recrystallisation directly to the elastic anisotropy of crystals and through this to the orientation of the stress field. At this stage the observation that ice CPOs developed at relatively high temperature and particularly at low strain correspond to high Schmid factor orientations remains robust. The underlying mechanisms will need continual review as we collect new data.

At temperatures greater than -10° the cone opening angle (θ) from experiments decreases from 42° at ~3% strain to ~ 30° at 20-50% strain. Hooke and Huddleston’s (1981) data from Barnes ice cap suggest it may reduce further to ~18° at ~143% strain (Table 4, Fig. 13). The cone opening angle does not stabilise at the easiest slip orientation of 45°, suggesting that GBM alone cannot be the mechanism that controls the CPO development. Previous studies suggest CPO evolves through the parallel operation of rotation and selective growth (e.g. Kamb, 1972; Qi et al., 2017). The narrowing of cone-shaped *c*-axis CPO has been explained by an activation of grain rotation (Jacka and Li., 2000; Qi et al., 2017). Jacka and Macagnan (1984) show that the *c*-axis cone narrows in compression and opens in extension, consistent with the expected kinematics of grain rotation. Neighbour-pair misorientation axes at misorientation angles of 5°-10° show primary maxima lying in the basal plane (Fig. 4(g), 5(g), 6(g)) at both low and high strains. Therefore, we infer the decreasing of opening-angle θ as a function of strain is likely to result from more active grain rotation driven by intracrystalline glide on the basal plane. For all deformed samples in this study, there is a large peak at 2° in neighbour-pair misorientation angle distribution, which is not present in the random- or neighbour-pair data of the starting material (Fig. 4(f), 5(f), 6(f)). Moreover, neighbour-pair misorientation angles show much higher frequencies between 2° and 10° than random-pair data. These observations suggest recovery and subgrain rotation operated in parallel with strain-induced GBM. The dislocation activity required to generate subgrain structures and to provide the strain energy driving force for strain-induced GBM is likely the primary control on grain rotation (Duval and Castelnau, 1995; Llorens et al., 2016).

The opening-angle θ of the *c*-axes cone as well as the CPO intensity decrease with decreasing temperature (Table 2, 4; Fig. 8-10, 11(c), 13). Earlier studies have inferred that the selective growth of the grains oriented for easy slip orientations becomes less active due to the reduction of GBM activity at lower temperatures (Qi et al., 2017, 2019). Lower temperatures, for constant displacement rate experiments, correspond to higher stresses. Previous studies in deformed metals suggest a higher stress is likely a cause of higher dislocation densities (Bailey and Hirsch, 1960; Ajaja, 1991), that in turn will require kinematically more lattice rotation. The misorientation angle at which neighbour-pair frequency reduces to be equal to the random-pair frequency increases with decreasing temperature (Fig. 4(f), 5(f), 6(f)). Moreover, neighbour-pair misorientation axes at misorientation angles of 5°-10° show primary maxima lying in the basal plane (Fig. 4 (g), 5(g), 6(g)) for all deformed samples. These observations support the hypothesis that grain rotation becomes more prominent at lower temperatures (Jacka and Li., 2000), and it is dominantly driven by intracrystalline glide on the basal plane. More active grain rotation can lead to a closure of *c*-axis cone at lower temperatures: maxima parallel to compression are characteristic of strains ≥ 20% at temperatures colder than -30 °C (Craw et al., 2018; Prior et al., 2015).

4.1.4 CPO development: differences related to grain size

The CPO intensity (as indicated by M-index) of “small” grains is generally lower than “big” grains, and this contrast strengthens with decreasing temperature (Fig. 11(d)). At ~12% strain, the CPO pattern of “big” grains is clearer than “small” grains, at all temperatures (Fig. 12). These observations suggest a mechanism that weakens the CPO development may be associated with the “small” grains. At lower temperatures (-20 °C and -30 °C) typical “core-and-mantle” structures have small grains with orientations that are dispersed around neighbouring large grains (Fig. 7) and the misorientations of small grains with large or small neighbours lack a consistent or rational crystallographic control crystallographic control. Whole sample misorientations show that boundaries with >10° misorientation are less crystallographically-controlled than low angle boundaries. There are two published explanations that can explain weakening of CPO in smaller grains and the lack of rational crystallographic misorientation axes of small grains relative to each other or to larger grains. “Spontaneous” nucleation (Duval et al., 2012) driven by the relaxation of the dislocation-related internal stress field may produce nuclei with orientations not related to their corresponding parent grains (Falus et al., 2011; Chauve et al., 2017), and thus lead to a weaker CPO. Previous rock deformation studies reported small recrystallized grains having CPOs that are randomly dispersed equivalents of the stronger parent grain CPOs (Jiang et al., 2000; Bestmann and Prior, 2003; Storey and Prior, 2005; Warren and Hirth, 2006). These observations are commonly interpreted as the result of an increase in the contribution of grain boundary sliding (GBS) in fine grains. Craw and others (2018) reported similar observations in uniaxially deformed Antarctic ice, and the reduction of CPO intensity in grains with finer sizes was attributed to GBS. Bestmann and Prior (2003) suggest a randomization of boundary misorientation axes among “small” grains can result from sliding along boundaries of newly formed grains. GBS can accompany grain shape change by dislocation or diffusion processes (Raj and Ashby, 1971; Crossman and Ashby, 1975; Langdon 1994, 2006, 2009). Recently, Cross and others (2017b) found evidence for specific orientations (i.e., those lying in the plane of maximum vorticity) being randomized by GBS.

GBS is inherently grain size sensitive (Raj and Ashby, 1971; Gifkins 1976; Langdon, 1994; Warren and Hirth, 2006) and identification of GBS processes in ice was initially made by identification of grain size sensitivity of mechanical data for the deformation of fine-grained ice (Goldsby and Kohlstedt, 1997, 2001). Ice experiments at -10°C with two initial grain sizes, one similar to our experiments (PIL007 is one of these older experiments) and the other coarser, show significant peak stress grain size sensitivity (Fig. 3 in Qi et al., 2017), with a 2 to 3 fold increase in strain rate for a given stress. The grain size sensitivity is hidden in flow stress data as the grain size becomes controlled by the stress (Jacka and Li, 1994; De Bresser et al, 2001) and a flow law relationship can be defined independent of the grain size (De Bresser et al, 2001)

Both hypotheses— “spontaneous” nucleation and GBS—explain a weakening of CPO in “small” grains and these two ideas are not mutually exclusive. We have greater confidence in the GBS interpretation because it is consistent with the grain size sensitivity that is observed in comparable ice deformation experiments. Without GBS another explanation is needed for the grain size sensitivity. Further work is needed to test both hypotheses. Most critical are experiments where nuclei can be observed whilst they are very small and subsequent misorientations can be documented, as might be possible with 3-D microscopy methods (Lauridsen et al., 2003; Poulson et al., 2004), and experiments where fiducial markers are used to confirm the physical existence of offsets on grain boundaries (Schmid et al, 1977; Spiers, 1979 ; Beeré, 1978; Eleti et al., 2020).

4.2 Future work: implications for enhancement (weakening)

The mechanical weakening, i.e. stress drop after peak in constant load experiments and strain rate enhancement from secondary to tertiary creep in constant load experiments, has been associated with: (1) the softening of grains related to reduction in defect content associated with dynamic recovery and recrystallisation (Montagnat and Duval., 2000; Sakai et al., 2014), (2) increased contribution of grain size sensitive deformation mechanisms due to grain size reduction resulting from dynamic recrystallization (De Bresser et al., 2001), and (3) development of strong CPO in viscously anisotropic materials (Durham and Goetze, 1977; Hansen et al., 2012) such as ice. The microstructural data as discussed in section 4.1 will enable us to comment on the contribution of different mechanisms to the weakening in deformed polycrystalline ice.

All experiments show weakening after peak stress. Weakening is classically observed during dynamic recrystallization, and it was attributed to a balance between GBM and nucleation of new grains (Montagnat and Duval., 2000; Sakai et al., 2014). In this study, mean and median ice grain size reduces with strain at all temperatures (Table 3, Fig. 11(a)). Grain size is commonly reduced during rock deformation in the laboratory (e.g. Pieri et al., 2001; Hansen et al., 2012) and in nature (Trimby et al., 1998; Bestmann and Prior, 2003). At smaller grain sizes the strain rate contribution of grain size sensitive (GSS) mechanisms increases or the stress required to drive a given strain rate contribution of GSS decreases. For this reason, grain size reduction has been proposed as a weakening mechanism (Rutter and Brodie, 1988; De Bresser et al 2001; Kilian et al., 2011; Campbell and Menegon, 2019). On the other hand, many published papers on ice sheet mechanics imply that enhancement (weakening) is caused by anisotropy development and there are analytical numerical models that seek to quantify this relationship (Azuma, 1995; Morland and Staroszczyk, 2009; Placidi et al., 2010). At -10 °C the CPO development includes many grains with basal plane orientations that would facilitate further axial shortening and it is intuitive that the CPO development could provide a cause for the weakening. However, at -30 °C the CPO developed at high strain is a narrow cone or cluster with many basal planes sub-perpendicular to compression. In this case the CPO would hinder further axial shortening and it is intuitive that the CPO should cause strengthening. Nevertheless, weakening occurs at -30 °C. Development of CPO cannot provide a uniform explanation for weakening across the range of laboratory experiments presented here. Therefore, further studies are required to quantify: (1) the contribution of nucleation and GBM to the total stress drop if the balance of GBM and nucleation is considered as the weakening mechanism; (2) The contribution of grain size insensitive, e.g. dislocation creep, and grain size sensitive processes, e.g. GBS, to the total stress drop if grain size reduction is considered as the weakening mechanism.

5 Conclusions

1. We deformed isotropic polycrystalline pure water ice to successive strains (~3%, 5%, 8%, 12% and 20%) under a constant displacement rate (strain rate $\sim 1.0 \times 10^{-5} s^{-1}$) at -10, -20 and -30 °C. For all deformed samples, stress first rises to a peak at ~1-4% strain and then drops to lower stresses at higher strains. Samples deformed at colder temperatures show higher peak and final stresses, as expected for the temperature dependency of creep. Microstructural and CPO analyses were conducted on deformed ice samples using cryo-EBSD.
2. All deformed samples develop distinct subgrain boundaries and show a peak at 2°-3° in the neighbour-pair misorientation angle distribution. Mean/median subgrain size is smaller than mean/median grain size. These observations suggest that dislocation glide and associated recovery and subgrain rotation were active in all deformed samples. Neighbour-pair low-angle (5°-10°) misorientation axes show primary maxima lying in the basal plane, for all samples, suggesting that basal glide dominated the intragranular deformation process. Subgrain boundary misorientation distributions extend to higher misorientation angles with strain and with decreasing temperature, suggesting that subgrain rotation develops progressively and is more effective at lower temperatures.
3. All deformed samples have skewed grain size distributions with a strong peak at small (<100 μm) sizes and a tail to larger sizes. The grain size peak is smaller than the grain size of the starting material (~297 μm) and a stereological analysis suggests that many of the small grains, measured in 2 - dimensions, are also small in 3 – dimensions. The number density of “distinct” grains (counting 2-D grains that are out of the analysis plane to the same 3-D grain) is more than 3 times that in the starting material for all deformed samples and the number density increases with strain. These data suggest that nucleation is involved in dynamic recrystallization. “Core-and-mantle” (small grains surrounding larger grains) are observed at high strains and are clearest at -20 and -30 °C, suggesting that subgrain rotation recrystallization has occurred

and is more important at lower temperatures. Lobate grain boundaries suggest that strain induced grain boundary migration has occurred in all samples.

4. Many of the deformed samples have CPOs defined by open cones (small circles) of *c*-axes. The cone opening-angle decreases with strain. The CPO intensity and *c*-axis opening-angle both decrease as the temperature drops from -10 °C to -30 °C. At -30 °C and 20% strain the *c*-axes define a cluster with maximum parallel to compression, rather than an open cone. We interpret that the of the open *c*-axis cone develops because strain-induced GBM favours the growth of grains in easy slip orientations. The closure of the *c*-axes cone with strain is interpreted primarily as the result of grain rotation related to intragranular dislocation glide on the basal plane. We infer that grain rotation becomes more prominent at lower temperatures, whilst GBM is more effective at higher temperatures.
5. Small grains have a weaker CPO than large grains. This distinction is slight at -10 °C, but becomes much clearer at lower temperatures. Neighbour-pair high-angle (≥ 10°) misorientation axes, corresponding to grain boundaries are not strongly aligned in the basal plane, nor with any other crystal direction. An additional process is needed to explain these observations. We identify two candidate processes; (1) grain boundary sliding causing rotation of grains without crystallographic control on the rotation axes and (2) "spontaneous" nucleation in random initial orientations.

Author contributions. DJP, DLG and SF designed the research. DJP, SF, TH, AJC and CQ performed experiments. SF, DJP and MN collected the cryo-EBSD data. SF, DJP and JW analysed data. SF and DJP wrote the draft. All authors edited the paper.

Acknowledgements. We are thankful to Pat Langhorne for providing the cold room facility at University of Otago. This work was supported by a NASA fund (NNX15AM69G) and two Marsden Funds of the Royal Society of New Zealand (UOO1116 and UOO052). SF was supported by the University of Otago doctoral scholarship, the Antarctica New Zealand doctoral scholarship and the University of Otago PERT (Polar Environment Research Theme) seed funding. We thank the journal reviwers Maurine Montagnat and Olivier Castelnau for very helpful reviews of the paper and Roger LeB. Hooke and Christopher J. L. Wilson for helpful additional comments.

Competing interests. The authors declare that they have no conflict of interest.

Data availability. Data available on request from the authors.

References

Ajaja, O.: Role of recovery in high temperature constant strain rate deformation, J Mater Sci, 26, 6599–6605, https://doi:10.1007/BF02402651, 1991.

Alley, R. B.: Flow-law hypotheses for ice-sheet modeling, J. Glaciol., 38, 245–256, https://doi.org/10.1017/s0022143000003658, 1992.

Austin, N. J. and Evans, B.: Paleowattmeters: A scaling relation for dynamically recrystallized grain size, Geology, 35, 343–4, https://doi.org/10.1130/g23244a.1, 2007.

Azuma, N.: A flow law for anisotropic polycrystalline ice under uniaxial compressive deformation, Cold Regions Science and Technology, 23, 137–147, https://doi.org/10.1016/0165-232x(94)00011-l, 1995.

Bachmann, F., Hielscher, R., and Schaeben, H.: Grain detection from 2-D and 3-D EBSD data—Specification of the MTEX algorithm, Ultramicroscopy, 111, 1720-1733, https://doi.org/10.1016/j.ultramic.2011.08.002, 2011.

Bailey, J. E. and Hirsch, P. B.: The dislocation distribution, flow stress, and stored energy in cold-worked polycrystalline silver, Philosophical Magazine, 5, 485–497, https://doi.org/10.1080/14786436008238300, 1960.

Bamber, J. L., Oppenheimer, M., Kopp, R. E., Aspinall, W. P., and Cooke, R. M.: Ice sheet contributions to future sea-level rise from structured expert judgment, Proceedings of the National Academy of Sciences of the United States of America, 116, 11195-11200, https://doi.org/10.1073/pnas.1817205116, 2019.

Beeré, W.: Stresses and deformation at grain boundaries, Philosophical Transactions of the Royal Society of London. Series A, Mathematical and Physical Sciences, 288(1350), 177–196, https://doi.org/10.1098/rsta.1978.0012, 1978.

Berger, A., Herwegh, M., Schwarz, J.-O. and Putlitz, B.: Quantitative analysis of crystal/grain sizes and their distributions in 2D and 3D, Journal of Structural Geology, 33, 1751–1763, https://doi.org/10.1016/j.jsg.2011.07.002, 2011.

Bestmann, M. and Prior, D. J.: Intragranular dynamic recrystallization in naturally deformed calcite marble: diffusion accommodated grain boundary sliding as a result of subgrain rotation recrystallization, Journal of Structural Geology, 25, 1597-1613, https://doi.org/10.1016/s0191-8141(03)00006-3, 2003.

Bindschadler, R. A., Nowicki, S., Abe-Ouchi, A., Aschwanden, A., Choi, H., Fastook, J., Granzow, G., Greve, R., Gutowski, G., Herzfeld, U., Jackson, C., Johnson, J., Khroulev, C., Levermann, A., Lipscomb, W. H., Martin, M. A., Morlighem, M., Parizek, B. R., Pollard, D., Price, S. F., Ren, D. D., Saito, F., Sato, T., Seddik, H., Seroussi, H., Takahashi, K., Walker, R., and Wang, W. L.: Ice-sheet model sensitivities to environmental forcing and their use in projecting future sea level (the SeaRISE project), Journal of Glaciology, 59, 195-224, https://doi.org/10.3189/2013jog12j125, 2013.

Budd, W. F. and Jacka, T. H.: A review of ice rheology for ice sheet modelling, Cold Regions Science and Technology, 16, 107-144, https://doi.org/10.1016/0165-232x(89)90014-1, 1989.

Budd, W. F., Warner, R. C., Jacka, T. H., Li, J. and Treverrow, A.: Ice flow relations for stress and strain-rate components from combined shear and compression laboratory experiments, Journal of Glaciology, 59(214), 374–392, https://doi.org/10.3189/2013jog12j106, 2013.

Campbell, L. R. and Menegon, L.: Transient High Strain Rate During Localized Viscous Creep in the Dry Lower Continental Crust (Lofoten, Norway), Journal of Geophysical Research: Solid Earth, 124, 10240–10260, https://doi.org/10.1029/2019jb018052, 2019.

Castelnau, O., Duval, P., Lebensohn, R. A. and Canova, G. R.: Viscoplastic modeling of texture development in polycrystalline ice with a self-consistent approach: Comparison with bound estimates, Journal of Geophysical Research: Solid Earth, 101 13851–13868, https://doi.org/10.1029/96JB00412, 1996.

Castelnau, O., Duval, P., Montagnat, M. and Brenner, R.: Elastoviscoplastic micromechanical modeling of the transient creep of ice, Journal of Geophysical Research, 113(B11), 749–14, https://doi.org/10.1029/2008JB005751, 2008.

Chauve, T., Montagnat, M., Barou, F., Hidas, K., Tommasi, A. and Mainprice, D.: Investigation of nucleation processes during dynamic recrystallization of ice using cryo-EBSD, Phil. Trans. R. Soc. A, 375 20150345–20, https://doi.org/10.1098/rsta.2015.0345, 2017.

Craw, L., Qi, C., Prior, D. J., Goldsby, D. L., and Kim, D.: Mechanics and microstructure of deformed natural anisotropic ice, J. Struct. Geol., 115, 152–166, https://doi.org/10.1016/j.jsg.2018.07.014, 2018.

Cross, A. J., Prior, D. J., Stipp, M. and Kidder, S.: The recrystallized grain size piezometer for quartz: An EBSD-based calibration, Geophysical Research Letters, 44, 6667–6674, https://doi.org/10.1002/2017gl073836, 2017a.

Cross, A. J., Hirth, G. and Prior, D. J.: Effects of secondary phases on crystallographic preferred orientations in mylonites, Geology, 45, 955–958, https://doi.org/10.1130/g38936.1, 2017b.

Cole, D. M.: Preparation of polycrystalline ice specimens for laboratory experiments, Cold Regions Science and Technology, 1, 153-159, https://doi.org/10.1016/0165-232x(79)90007-7, 1979.

Cuffey, K.M. and Paterson, W.S.B. (4th Eds.): The Physics of Glaciers, Butterworth-Heinemann, Elsevier, U.S.A., 2010.

De Bresser, J., Ter Heege, J., and Spiers, C.: Grain size reduction by dynamic recrystallization: can it result in major rheological weakening?, Int. J. Earth Sci., 90, 28–45, https://doi.org/10.1007/s005310000149, 2001.

Derby, B.: The dependence of grain size on stress during dynamic recrystallisation, Acta Metallurgica et Materialia, 39, 955–962, https://doi.org/10.1016/0956-7151(91)90295-c, 1991.

Dutton, A., Carlson, A. E., Long, A. J., Milne, G. A., Clark, P. U., DeConto, R., Horton, B. P., Rahmstorf, S., and Raymo, M. E.: Sea-level rise due to polar ice-sheet mass loss during past warm periods, Science, 349, 153, https://doi.org/10.1126/science.aaa4019, 2015.

Durham, W. B. and Goetze, C.: Plastic flow of oriented single crystals of olivine: 1. Mechanical data, Journal of geophysical Research, 82, 5737-5753, https://doi.org/10.1029/jb082i036p05737, 1977.

Durham, W. B., Heard, H. C., and Kirby, S. H.: Experimental deformation of polycrystalline H2O ice at high pressure and low temperature: Preliminary results, Journal of Geophysical Research: Solid Earth, 88, B377-B392, https://doi.org/10.1029/jb088is01p0b377, 1983.

Durham, W. B., Kirby, S. H., and Stern, L. A.: Effects of dispersed particulates on the rheology of water ice at planetary conditions, Journal of Geophysical Research: Planets, 97, 20883-20897, https://doi.org/10.1029/92je02326, 1992.

Durham, W. B., Prieto-Ballesteros, O., Goldsby, D. L., and Kargel, J. S.: Rheological and Thermal Properties of Icy Materials, Space Science Reviews, 153, 273-298, https://doi.org/10.1007/s11214-009-9619-1, 2010.

Duval, P.: Creep and recrystallization of polycrystalline ice, bulmi, 102, 80–85, https://doi.org/10.3406/bulmi.1979.7258, 1979.

Duval, P., Ashby, M. F., and Anderman, I.: Rate-controlling processes in the creep of polycrystalline ice, J. Phys. Chem., 87, 4066–4074, https://doi.org/10.1021/j100244a014, 1983.

Duval, P. and Castelnau, O.: Dynamic recrystallization of ice in polar ice sheets, J. Phys. IV, 05, C3–197–C3–205, https://doi:10.1051/jp4:1995317, 1995.

Duval, P., Montagnat, M., Grennerat, F., Weiss, J., Meyssonnier, J., and Philip, A.: Creep and plasticity of glacier ice: a material science perspective, Journal of Glaciology, 56, 1059–1068, https://doi.org/10.3189/002214311796406185, 2010.

Eleti, R. R., Chokshi, A. H., Shibata, A., and Tsuji, N.: Unique high-temperature deformation dominated by grain boundary sliding in heterogeneous necklace structure formed by dynamic recrystallization in HfNbTaTiZr BCC refractory high entropy alloy, Acta Materialia, 183, 64–77, https://doi.org/10.1016/j.actamat.2019.11.001, 2020.

Falus, G., Tommasi, A., and Soustelle, V.: The effect of dynamic recrystallization on olivine crystal preferred orientations in mantle xenoliths deformed under varied stress conditions, Journal of Structural Geology, 33, 1528–1540, https://doi.org/10.1016/j.jsg.2011.09.010, 2011.

Faria, S. H., Weikusat, I., and Azuma, N.: The microstructure of polar ice. Part II: State of the art, Journal of Structural Geology, 61, 21–49, https://doi.org/10.1016/j.jsg.2013.11.003, 2014.

Fliervoet, T. F., Drury, M. R., and Chopra, P. N., Crystallographic preferred orientations and misorientations in some olivine rocks deformed by diffusion or dislocation creep: Tectonophysics, 303, 1-27, https://doi.org/10.1016/s0040-1951(98)00250-9, 1999.

Gammon, P. H., Kiefte, H., Clouter, M. J., and Denner, W. W.: Elastic constants of artificial and natural ice samples by Brillouin spectroscopy, Journal of glaciology, 29, 433-460, https://doi.org/10.3189/s0022143000030355, 1983.

Gao, X. Q. and Jacka, T. H.: The approach to similar tertiary creep rates for antarctic core ice and laboratory prepared ice, J. Phys. Colloques, 48, C1–289–C1–296, https://doi:10.1051/jphyscol:1987141, 1987.

Gifkins, R.: Grain-boundary sliding and its accommodation during creep and superplasticity, Metallurgical transactions a, 7, 1225-1232, https://doi.org/10.1007/bf02656607, 1976.

Glen, J. W.: The creep of polycrystalline ice. Proceedings of the Royal Society of London. Series A. Mathematical and Physical Sciences, 228, 519-538, https://doi.org/10.1098/rspa.1955.0066, 1955.

Goldsby, D. L. and Kohlstedt, D. L.: Grain boundary sliding in fine-grained ice I, Scripta Materialia, 37, 1399-1406, https://doi.org/10.1016/s1359-6462(97)00246-7, 1997.

Goldsby, D. L. and Kohlstedt, D. L.: Superplastic deformation of ice: Experimental observations, Journal of Geophysical Research: Solid Earth, 106, 11017-11030, https://doi.org/10.1029/2000jb900336, 2001.

Gomez-Rivas, E., Griera, A., Llorens, M. G., Bons, P. D., Lebensohn, R. A., and Piazolo, S.: Subgrain rotation recrystallization during shearing: insights from full-field numerical simulations of halite polycrystals, Journal of Geophysical Research: Solid Earth, 122, 8810-8827, https://doi.org/10.1002/2017jb014508, 2017.

Grennerat, F., Montagnat, M., Castelnau, O., Vacher, P., Moulinec, H., Suquet, P. and Duval, P.: Experimental characterization of the intragranular strain field in columnar ice during transient creep, Acta Materialia, 60, 3655–3666, https://doi.org/10.1016/j.actamat.2012.03.025, 2012.

Grimmer, H.: The distribution of disorientation angles if all relative orientations of neighbouring grains are equally probable, Scripta Metallurgica, 13, 161–164, https://doi.org/10.1016/0036-9748(79)90058-9, 1979.

Guillope, M. and Poirier, J. P.: Dynamic recrystallization during creep of single-crystalline halite: An experimental study, Journal of Geophysical Research: Solid Earth, 84, 5557-5567, https://doi.org/10.1029/jb084ib10p05557, 1979.

Halfpenny, A., Prior, D. J., and Wheeler, J.: Analysis of dynamic recrystallization and nucleation in a quartzite mylonite, Tectonophysics, 427, 3-14, https://doi.org/10.1016/j.tecto.2006.05.016, 2006.

Hansen, L. N., Zimmerman, M. E., and Kohlstedt, D. L.: The influence of microstructure on deformation of olivine in the grain-boundary sliding regime, J. Geophys. Res., 117, B09201, https://doi.org/10.1029/2012JB009305, 2012.

Hartmann, W. K.: Surface evolution of two-component stone / ice bodies in the Jupiter region, Icarus, 44, 441-453, https://doi.org/10.1016/0019-1035(80)90036-6, 1980.

Heard, H. C., Durham, W. B., Boro, C. O., and Kirby, S. H.: A triaxial deformation apparatus for service at 77 ≤T≤ 273 K, in: The Brittle-Ductile Transition in Rocks, edited by: Duba, A. G., Durham, W. B., Handin, J. W., and Wang, H. F., 225–228, https://doi.org/10.1029/GM056p0225, 1990.

Hidas, K., Tommasi, A., Mainprice, D., Chauve, T., Barou, F. and Montagnat, M.: Microstructural evolution during thermal annealing of ice-Ih, Journal of Structural Geology, 99, 31–44, https://doi.org/10.1016/j.jsg.2017.05.001, 2017.

Hirth, G., and Tullis, J.: Dislocation creep regimes in quartz aggregates, Journal of structural geology, 14, 145-159, https://doi.org/10.1016/0191-8141(92)90053-y, 1992.

Hobbs, B. E., Means, W. D., and Williams, P. F. (1st Eds.): An outline of structural geology, Wiley, 1976.

Homer, D. R. and Glen, J. W.: The creep activation energies of ice, Journal of Glaciology, 21, 429-444, https://doi.org/10.1017/s0022143000033591, 1978.

Hooke, R. L. and Hudleston, P. J.: Ice Fabrics in a Vertical Flow Plane, Barnes Ice Cap, Canada, Journal of Glaciology, 25(92), 195–214, doi:10.3189/S0022143000010443, 1980.

Hooke, R. L. and Hudleston, P. J.: Ice fabrics from a borehole at the top of the south dome, Barnes Ice Cap, Baffin Island, Geological Society of America Bulletin, 92(5), 274–281, https://doi.org/10.1130/0016-7606(1981)92<274:iffaba>2.0.co;2, 1981.

Hudleston, P.J.: Structures and fabrics in glacial ice: a review, J. Struct. Geol., 81, 1–27, https://doi.org/10.1016/j.jsg.2015.09.003, 2015.

Humphreys, F. J. and Hatherly, M. (2nd Eds.): Recrystallization and related annealing phenomena, Elsevier, 2004.

Jacka, T. H. and Maccagnan, M.: Ice crystallographic and strain rate changes with strain in compression and extension, Cold Regions Science and Technology, 8(3), 269–286, https://doi.org/10.1016/0165-232x(84)90058-2, 1984.

Jacka, T. H. and Li, J.: The steady-state crystal size of deforming ice, Annals of Glaciology, 20, 13-18, https://doi.org/10.3189/172756494794587230, 1994.

Jacka, T. H. and Li, J.: Flow rates and crystal orientation fabrics in compression of polycrystalline ice at low temperatures and stresses, in: International Symposium on Physics of Ice Core Records, Shikotsukohan, Hokkaido, Japan, 14–17 September 1998, edited by: Hondoh, T., 83–102, 2000.

Jafari, M. and Najafizadeh, A.: Correlation between Zener–Hollomon parameter and necklace DRX during hot deformation of 316 stainless steel, Materials Science and Engineering A, 501, 16–25, https://doi.org/10.1016/j.msea.2008.09.073, 2009.

Jessell, M. W.: Grain boundary migration and fabric development in experimentally deformed octachloropropane, Journal of Structural Geology, 8, 527–542, https://doi.org/10.1016/0191-8141(86)90003-9, 1986.

Jiang, Z., Prior, D. J., and Wheeler, J.: Albite crystallographic preferred orientation and grain misorientation distribution in a low-grade mylonite: implications for granular flow, Journal of Structural Geology, 22, 1663-1674, https://doi.org/10.1016/s0191-8141(00)00079-1, 2000.

Journaux, B., Chauve, T., Montagnat, M., Tommasi, A., Barou, F., Mainprice, D. and Gest, L.: Recrystallization processes, microstructure and crystallographic preferred orientation evolution in polycrystalline ice during high-temperature simple shear, The Cryosphere, 13, 1495–1511, https://doi.org/10.5194/tc-13-1495-2019, 2019.

Kamb, W. B.: Ice petrofabric observations from Blue Glacier, Washington, in relation to theory and experiment, Journal of Geophysical Research, 64, 1891–1909, https://doi:10.1029/JZ064i011p01891, 1959.

Kamb, W. B.: Experimental recrystallization of ice under stress, in: Flow and Fracture of Rocks, edited by Heard, H. C., Borg, I. Y., Carter, N. L., and Rayleigh, C. B., American Geophysical Union, 211–242, https://doi.org/10.1029/gm016p0211, 1972.

Kamb, B.: Basal Zone of the West Antarctic Ice Streams and its Role in Lubrication of Their Rapid Motion, American Geophysical Union (AGU), Washington, D. C., 2008.

Kilian, R., Heilbronner, R., and Stünitz, H.: Quartz grain size reduction in a granitoid rock and the transition from dislocation to diffusion creep, Journal of Structural Geology, 33, 1265-1284, https://doi.org/10.1016/j.jsg.2011.05.004, 2011.

Kirby, S. H., Durham, W. B., Beeman, M. L., Heard, H. C. and Daley, M. A.: Inelastic properties of ice 1h at low temperatures and high pressures, J. Phys. Colloques, 48, C1–227–C1–232, https://doi.org/10.1051/jphyscol:1987131, 1987.

Kopp, R. E., DeConto, R. M., Bader, D. A., Hay, C. C., Horton, R. M., Kulp, S., Oppenheimer, M., Pollard, D. and Strauss, B. H.: Evolving Understanding of Antarctic Ice-Sheet Physics and Ambiguity in Probabilistic Sea-Level Projections, Earth's Future, 5, 1217–1233, https://doi.org/10.1002/2017ef000663, 2017.

Kuiper, E. J. N., Weikusat, I., de Bresser, J. H., Jansen, D., Pennock, G. M., and Drury, M. R.: Using a composite flow law to model deformation in the NEEM deep ice core, Greenland: Part 1 the role of grain size and grain size distribution on the deformation of Holocene and glacial ice, The Cryosphere Discuss, https://doi.org/10.5194/tc-2018-275, 2019a.

Kuiper, E. J. N., de Bresser, J. H. P., Drury, M. R., Eichler, J., Pennock, G. M. and Weikusat, I.: Using a composite flow law to model deformation in the NEEM deep ice core, Greenland: Part 2 the role of grain size and premelting on ice deformation at high homologous temperature, The Cryosphere Discussions, https://doi:10.5194/tc-2018-275, 2019b.

Lallemant, H. G. A.: Subgrain rotation and dynamic recrystallization of olivine, upper mantle diapirism, and extension of the Basin-and-Range Province, Tectonophysics, 119, 89-117, https://doi.org/10.1016/0040-1951(85)90034-4, 1985.

Langdon, T. G.: A unified approach to grain boundary sliding in creep and superplasticity, Acta Metallurgica et Materialia, 42, 2437–2443, https://doi.org/10.1016/0956-7151(94)90322-0, 1994.

Langdon, T. G.: Grain boundary sliding revisited: Developments in sliding over four decades, J Mater Sci, 41, 597–609, https://doi.org/10.1007/s10853-006-6476-0, 2006.

Langdon, T. G.: Seventy-five years of superplasticity: historic developments and new opportunities, J Mater Sci, 44, 5998–6010, https://doi.org/10.1007/s10853-009-3780-5, 2009.

Lauridsen, E. M., Poulsen, H. F., Nielsen, S. F. and Juul Jensen, D.: Recrystallization kinetics of individual bulk grains in 90% cold-rolled aluminium, Acta Materialia, 51, 4423–4435, https://doi.org/10.1016/s1359-6454(03)00278-7, 2003.

Little, T. A., Prior, D. J., Toy, V. G. and Lindroos, Z. R.: The link between strength of lattice preferred orientation, second phase content and grain boundary migration: A case study from the Alpine Fault zone, New Zealand, Journal of Structural Geology, 81(C), 59–77, https://doi.org/10.1016/j.jsg.2015.09.004, 2015.

Llorens, M.-G., Griera, A., Bons, P. D., Roessiger, J., Lebensohn, R., Evans, L. and Weikusat, I.: Dynamic recrystallisation of ice aggregates during co-axial viscoplastic deformation: a numerical approach, Journal of Glaciology, 62, 1–19, https://doi.org/10.1017/jog.2016.28, 2016.

Lopez-Sanchez, M. A. and Llana-Fúnez, S.: An evaluation of different measures of dynamically recrystallized grain size for paleopiezometry or paleowattometry studies, Solid Earth, 6, 475-495, https://doi.org/10.5194/se-6-475-2015, 2015.

Mainprice, D., Bachmann, F., Hielscher, R., and Schaeben, H.: Descriptive tools for the analysis of texture projects with large datasets using MTEX: strength, symmetry and components, Geological Society, London, Special Publications, 409, 251-271, https://doi.org/10.1144/sp409.8, 2015.

MacDonald, J. M., Wheeler, J., Harley, S. L., Mariani, E., Goodenough, K. M., Crowley, Q. and Tatham, D.: Lattice distortion in a zircon population and its effects on trace element mobility and U–Th–Pb isotope systematics: examples from the Lewisian Gneiss Complex, northwest Scotland, Contrib Mineral Petrol, 166, 21–41, https://doi.org/10.1007/s00410-013-0863-8, 2013.

Mellor, M. and Cole, D. M.: Deformation and failure of ice under constant stress or constant strain-rate, Cold Regions Science and Technology, 5, 201-219, https://doi.org/10.1016/0165-232x(82)90015-5, 1982.

Mellor, M. and Cole, D. M.: Stress/strain/time relations for ice under uniaxial compression, Cold Regions Science and Technology, 6, 207–230, https://doi.org/10.1016/0165-232x(83)90043-5, 1983.

Montagnat, M. and Duval, P.: Rate controlling processes in the creep of polar ice, infuence of grain boundary migration associated with recrystallization, Earth and Planetary Science Letters, 183, 179–186, https://doi.org/10.1016/s0012-821x(00)00262-4, 2000.

Montagnat, M., Azuma, N., Dahl-Jensen, D., Eichler, J., Fujita, S., Gillet-Chaulet, F., Kipfstuhl, S., Samyn, D., Svensson, A. and Weikusat, I.: Fabric along the NEEM ice core, Greenland, and its comparison with GRIP and NGRIP ice cores, The Cryosphere, 8, 1129–1138, https://doi.org/10.5194/tc-8-1129-2014, 2014.

Montagnat, M., Chauve, T., Barou, F., Tommasi, A., Beausir, B., and Fressengeas, C.: Analysis of dynamic recrystallization of ice from EBSD orientation mapping, Frontiers in Earth Science, 3, 81, https://doi.org/10.3389/feart.2015.00081, 2015.

Monz, M. E., Hudleston, P. J., Prior, D. J., Michels, Z., Fan, S.., Negrini, M., and Langhorne, P.: Electron backscatter diffraction (EBSD) based determination of crystallographic preferred orientation (CPO) in warm, coarse-grained ice: a case study, Storglaciären, Sweden, The Cryosphere Discuss, https://doi.org/10.5194/tc-2020-135, 2020.

Morawiec, A.: Misorientation-Angle Distribution of Randomly Oriented Symmetric Objects, J Appl Crystallogr, 28, 289–293, https://doi.org/10.1107/s0021889894011088, 1995.

Morland, L. W. and Staroszczyk, R.: Ice viscosity enhancement in simple shear and uni-axial compression due to crystal rotation, International Journal of Engineering Science, 47, 1297–1304, https://doi.org/10.1016/j.ijengsci.2008.09.011, 2009.

Obbard, R., Baker, I. and Sieg, K.: Using electron backscatter diffraction patterns to examine recrystallization in polar ice sheets, Journal of Glaciology, 52, 546–557, https://doi.org/10.3189/172756506781828458, 2006.

Passchier, C. W. and Trouw, R. A. (2nd Eds.): Microtectonics, Springer Science and Business Media, 2005.

Peternell, M., Dierckx, M., Wilson, C. J. L. and Piazolo, S.: Quantification of the microstructural evolution of polycrystalline fabrics using FAME: Application to in situ deformation of ice, Journal of Structural Geology, 61, 109–122, https://doi.org/10.1016/j.jsg.2013.05.005, 2014.

Peternell, M. and Wilson, C. J. L.: Effect of strain rate cycling on microstructures and crystallographic preferred orientation during high-temperature creep, Geology, 44, 279–282, https://doi.org/10.1130/g37521.1, 2016.

Piazolo, S., Bestmann, M., Prior, D. J., and Spiers, C. J.: Temperature dependent grain boundary migration in deformed-then-annealed material: observations from experimentally deformed synthetic rocksalt, Tectonophysics, 427, 55-71, https://doi.org/10.1016/j.tecto.2006.06.007, 2006.

Piazolo, S., Montagnat, M. and Blackford, J. R.: Sub-structure characterization of experimentally and naturally deformed ice using cryo-EBSD, Journal of Microscopy, 230, 509–519, https://doi.org/10.3189/172756506781828458, 2008.

Piazolo, S., Wilson, C. J., Luzin, V., Brouzet, C., and Peternell, M.: Dynamics of ice mass deformation: Linking processes to rheology, texture, and microstructure, Geochemistry, Geophysics, Geosystems, 14, 4185-4194, https://doi.org/10.1002/ggge.20246, 2013.

Pieri, M., Burlini, L., Kunze, K., Stretton, I. and Olgaard, D. L.: Rheological and microstructural evolution of Carrara marble with high shear strain: results from high temperature torsion experiments, Journal of Structural Geology, 23, 1393–1413, https://doi.org/10.1016/s0191-8141(01)00006-2, 2001.

Placidi, L., Faria, S. H., and Hutter, K.: On the role of grain growth, recrystallization and polygonization in a continuum theory for anisotropic ice sheets, Annals of Glaciology, 39, 49-52, https://doi.org/10.3189/172756404781814410, 2004.

Placidi, L., Greve, R., Seddik, H. and Faria, S. H.: Continuum-mechanical, Anisotropic Flow model for polar ice masses, based on an anisotropic Flow Enhancement factor, Continuum Mech. Thermodyn., 22, 221–237, https://doi.org/10.1007/s00161-009-0126-0, 2010.

Poirier, J. P. and Nicolas, A.: Deformation-induced recrystallization due to progressive misorientation of subgrains, with special reference to mantle peridotites, The Journal of Geology, 83, 707-720, https://doi.org/10.1086/628163, 1975.

Pollard, D.: A retrospective look at coupled ice sheet–climate modeling, Climatic Change, 100, 173–194, https://doi.org/10.1007/s10584-010-9830-9, 2010.

Ponge, D. and Gottstein, G.: Necklace formation during dynamic recrystallization: Mechanisms and impact on flow behavior, Acta Materialia, 46, 69–80, https://doi.org/10.1016/s1359-6454(97)00233-4, 1998.

Prior, D.J., Lilly, K., Seidemann, M., Vaughan, M., Becroft, L., Easingwood, R., Diebold, S., Obbard, R., Daghlian, C., Baker, I., and Caswell, T.: Making EBSD on water ice routine, Journal of microscopy, 259, 237-256, https://doi.org/10.1111/jmi.12258, 2015.

Qi, C., Goldsby, D. L., and Prior, D. J.: The down-stress transition from cluster to cone fabrics in experimentally deformed ice, Earth Planet. Sc. Lett., 471, 136–147, https://doi.org/10.1016/j.epsl.2017.05.008, 2017.

Qi, C., Prior, D.J., Craw, L., Fan, S., Llorens, M.G., Griera, A., Negrini, M., Bons, P.D., and Goldsby, D.L.: Crystallographic preferred orientations of ice deformed in direct-shear experiments at low temperatures, The Cryosphere, 13, 351-371, https://doi.org/10.5194/tc-13-351-2019, 2019.

Raj, R. and Ashby, M. F.: On grain boundary sliding and diffusional creep, Metallurgical Transactions, 2, 1113–1127, https://doi:10.1007/BF02664244, 1971.

Rignot, E., Mouginot, J., and Scheuchl, B.: Ice flow of the Antarctic ice sheet, Science, 333, 1427-1430, https://doi.org/10.1126/science.1208336, 2011.

Rutter, E. H. and Brodie, K. H.: The role of tectonic grain size reduction in the rheological stratification of the lithosphere, Geol Rundsch, 77, 295–307, https://doi.org/10.1007/bf01848691, 1988.

Sakai, T., Belyakov, A., Kaibyshev, R., Miura, H. and Jonas, J. J.: Dynamic and post-dynamic recrystallization under hot, cold and severe plastic deformation conditions, Progress in Materials Science, 60, 130–207, https://doi.org/10.1016/j.pmatsci.2013.09.002, 2014.

Scapozza, C. and Bartelt, P. A.: The influence of temperature on the small-strain viscous deformation mechanics of snow: a comparison with polycrystalline ice, Annals of Glaciology, 37, 90-96, https://doi.org/10.3189/172756403781815410, 2003.

Schmid, S. M., Boland, J. N. and Paterson, M. S.: Superplastic flow in finegrained limestone, Tectonophysics, 43, 257-291, https://doi.org/10.1016/0040-1951(77)90120-2, 1977.

Seidemann, M., Prior, D. J., Golding, N., Durham, W. B., Lilly, K., and Vaughan, M. J.: The role of kink boundaries in the deformation and recrystallisation of polycrystalline ice, Journal of Structural Geology, 136, 104010, https://doi.org/10.1016/j.jsg.2020.104010, 2020.

Shigematsu, N., Prior, D. J. and Wheeler, J.: First combined electron backscatter diffraction and transmission electron microscopy study of grain boundary structure of deformed quartzite, Journal of Microscopy, 224, 306–321, http://doi:10.1111/j.1365-2818.2006.01697.x, 2006.

Skemer, P., Katayama, I., Jiang, Z., and Karato, S. I.: The misorientation index: Development of a new method for calculating the strength of lattice-preferred orientation, Tectonophysics, 411, 157-167, https://doi.org/10.1016/j.tecto.2005.08.023, 2005.

Spiers, C. J.: Fabric development in calcite polycrystals deformed at 400° C, Bulletin de Minéralogie, 102, 282–289, https://doi.org/10.3406/bulmi.1979.7289, 1979.

Stern, L. A., Durham, W. B., and Kirby, S. H.: Grain-size-induced weakening of H2O ices I and II and associated anisotropic recrystallization, Journal of Geophysical Research: Solid Earth, 102, 5313-5325, https://doi.org/10.1029/96jb03894, 1997.

Stipp, M., StuÈnitz, H., Heilbronner, R., and Schmid, S. M.: The eastern Tonale fault zone: a ‘natural laboratory’for crystal plastic deformation of quartz over a temperature range from 250 to 700 C, Journal of structural geology, 24, 1861-1884, https://doi.org/10.1016/s0191-8141(02)00035-4, 2002.

Storey, C. D. and Prior, D. J.: Plastic deformation and recrystallization of garnet: a mechanism to facilitate diffusion creep, Journal of Petrology, 46, 2593-2613, https://doi.org/10.1093/petrology/egi067, 2005.

Treverrow, A., Budd, W. F., Jacka, T. H., and Warner, R. C.: The tertiary creep of polycrystalline ice: experimental evidence for stress-dependent levels of strain-rate enhancement, Journal of Glaciology, 58, 301-314, https://doi.org/10.3189/2012jog11j149, 2012.

Trimby, P. W., Prior, D. J., and Wheeler, J.: Grain boundary hierarchy development in a quartz mylonite, Journal of Structural Geology, 20, 917-935, https://doi.org/10.1016/s0191-8141(98)00026-1, 1998.

Underwood, E. E., Quantitative Stereology for Microstructural Analysis, in McCall, J. L., and Mueller, W. M., eds., Microstructural Analysis: Tools and Techniques: Boston, MA, Springer US, p. 35-66, 1973.

Urai, J. L., Means, W. D., and Lister, G. S.: Dynamic recrystallization of minerals, in: Mineral and Rock Deformation, edited by: Hobbs, B. and Heard, H., Laboratory Studies, 36, 161–199, https://doi.org/10.1029/gm036p0161, 1986.

Vaughan, M. J., Prior, D. J., Jefferd, M., Brantut, N., Mitchell, T. M., and Seidemann, M.: Insights into anisotropy development and weakening of ice from in situ P wave velocity monitoring during laboratory creep, J. Geophys. Res.-Sol. Ea., 122, 7076–7089, https://doi.org/10.1002/2017JB013964, 2017.

Warren, J. M. and Hirth, G.: Grain size sensitive deformation mechanisms in naturally deformed peridotites, Earth and Planetary Science Letters, 248, 438-450, https://doi.org/10.1016/j.epsl.2006.06.006, 2006.

Weertman, J.: Creep deformation of ice, Annual Review of Earth and Planetary Sciences, 11, 215-240, https://doi.org/10.1146/annurev.ea.11.050183.001243, 1983.

Weikusat, I., Kuiper, E.-J. N., Pennock, G. M., Kipfstuhl, S. and Drury, M. R.: EBSD analysis of subgrain boundaries and dislocation slip systems in Antarctic and Greenland ice, Solid Earth, 8, 883–898, https://doi.org/10.5194/se-8-883-2017, 2017.

Whalley, W. B. and Azizi, F.: Rock glaciers and protalus landforms: Analogous forms and ice sources on Earth and Mars, Journal of Geophysical Research: Planets, 108, https://doi.org/10.1029/2002je001864, 2003.

Wheeler, J., Prior, D., Jiang, Z., Spiess, R. and Trimby, P.: The petrological significance of misorientations between grains, Contrib Mineral Petrol, 141(1), 109–124, https://doi.org/10.1007/s004100000225, 2001.

Wheeler, J., Jiang, Z., Prior, D. J., Tullis, J., Drury, M. R., and Trimby, P. W.: From geometry to dynamics of microstructure: using boundary lengths to quantify boundary misorientations and anisotropy, Tectonophysics, 376, 19-35, https://doi.org/10.1016/j.tecto.2003.08.007, 2003.

Wheeler, J., Mariani, E., Piazolo, S., Prior, D. J., Trimby, P., and Drury, M. R.: The weighted Burgers vector: a new quantity for constraining dislocation densities and types using electron backscatter diffraction on 2-D sections through crystalline materials, Journal of microscopy, 233, 482-494, https://doi.org/10.1111/j.1365-2818.2009.03136.x, 2009.

White, S.: The effects of strain on the microstructures, fabrics, and deformation mechanisms in quartzites, Philosophical Transactions of the Royal Society of London, ser. A, Mathematical and Physical Sciences, 283, 69-86, https://doi.org/10.1098/rsta.1977.0014, 1976.

Wilson, C. J. L. and Russell-Head, D. S.: Steady-state preferred orientation of ice deformed in plane strain at –1° C, Journal of Glaciology, 28, 145–160, https://doi.org/10.3189/s0022143000011850, 1982.

Wilson, C. J. L. and Peternell, M.: Ice deformed in compression and simple shear: control of temperature and initial fabric, Journal of Glaciology, 58, 11-22, https://doi.org/10.3189/2012jog11j065, 2012.

Wilson, C. J. L., Peternell, M., Piazolo, S. and Luzin, V.: Microstructure and fabric development in ice: Lessons learned from in situ experiments and implications for understanding rock evolution, Journal of Structural Geology, 61, 50–77, https://doi.org/10.1016/j.jsg.2013.05.006, 2014.

Wilson, C. J. L., Hunter, N. J., Luzin, V., Peternell, M., and Piazolo, S.: The influence of strain rate and presence of dispersed second phases on the deformation behaviour of polycrystalline D2O ice, Journal of Glaciology, 65, 101-122, https://doi.org/10.1017/jog.2018.100, 2019.

Wilson, C. J. L., Peternell, M., Hunter, N. J. R. and Luzin, V.: Deformation of polycrystalline D2O ice: Its sensitivity to temperature and strain-rate as an analogue for terrestrial ice, Earth and Planetary Science Letters, 532, 115999, https://doi:10.1016/j.epsl.2019.115999, 2020.

Xia, H., and Platt, J. P.: Quartz grainsize evolution during dynamic recrystallization across a natural shear zone boundary, Journal of Structural Geology, 109, 120-126, https://doi.org/10.1016/j.jsg.2018.01.007, 2018.

Table 1 Summary of experiments

Sample No.	Temperature	Initial length	True axial strain	Peak stress (corrected)	Strain rate at peak stress	True axial strain at peak stress	Final stress (corrected)	Final strain rate
	T (°C)	L_0 (mm)	(ε)	σ_p (MPa)	$\dot{\varepsilon_p}$ (s^{-1})	ε_p	σ_f (MPa)	$\dot{\varepsilon_f}$ (s^{-1})
PIL176	-10	30.480	0.03	1.78	1.03×10^{-5}	0.02	1.70	1.04×10^{-5}
PIL163	-10	48.768	0.05	2.92	1.03×10^{-5}	0.01	2.42	1.06×10^{-5}
PIL178	-10	39.624	0.08	2.54	1.11×10^{-5}	0.02	1.97	1.19×10^{-5}
PIL177	-10	40.640	0.12	2.85	1.11×10^{-5}	0.03	1.90	1.21×10^{-5}
[1]PIL007	-10	63.754	0.19	2.13	1.03×10^{-5}	0.02	1.33	1.22×10^{-5}
PIL254	-20	39.624	0.03	4.33	1.05×10^{-5}	0.02	4.25	1.06×10^{-5}
PIL182	-20	46.990	0.04	4.88	8.09×10^{-6}	0.02	4.44	8.94×10^{-6}
PIL184	-20	31.242	0.08	3.64	1.13×10^{-5}	0.04	3.24	1.17×10^{-5}
PIL185	-20	41.656	0.12	4.69	1.09×10^{-5}	0.03	3.68	1.19×10^{-5}
PIL255	-20	49.530	0.20	4.66	1.10×10^{-5}	0.03	2.93	1.28×10^{-5}
PIL165	-30	37.846	0.03	8.24	1.08×10^{-5}	0.03	8.15	1.09×10^{-5}
PIL162	-30	50.546	0.05	8.71	1.07×10^{-5}	0.03	7.87	1.10×10^{-5}
PIL164	-30	45.974	0.07	8.93	1.03×10^{-5}	0.03	7.31	1.07×10^{-5}
PIL166	-30	45.466	0.12	7.60	1.11×10^{-5}	0.03	6.45	1.20×10^{-5}
PIL268	-30	47.240	0.21	7.82	1.10×10^{-5}	0.02	5.00	1.31×10^{-5}

[1] Experiment from study by Qi and others (2017).

Table 2 Summary of EBSD analyses

Sample No.	*T* (°C)	Data with 30 µm step size				Data with 5 µm step size			
		Map area (Width × Length (mm))	No. indexed	No. grains	M-index for all indexed pixels	Map area (Width × Length (mm))	No. indexed	No. grains	M-index for all indexed pixels
undeformed	-	33.18 × 20.55	545323	11318	0.00370	24.47 × 7.86	4444599	1242	0.004500
PIL176	-10	25.00 × 25.00	353781	4728	0.00119	5.41 × 4.00	785025	694	0.010244
PIL163	-10	24.53 × 10.28	201134	4851	0.00858	6.80 × 4.16	992513	1494	0.008886
PIL178	-10	16.20 × 20.30	235789	6270	0.05765	5.50 × 4.11	690117	1028	0.046907
PIL177	-10	16.67 × 15.38	163507	5018	0.04068	5.49 × 4.14	645076	1507	0.040403
[1]PIL007	-10	13.10 × 5.87	91830	1655	0.12457	1.88 × 12.43	1010898	1789	0.118133
PIL254	-20	34.26 × 9.33	166929	2735	0.00227	5.41 × 4.24	641292	903	0.006909
PIL182	-20	36.58 × 6.04	213919	4053	0.00540	5.48 × 4.28	691817	907	0.004948
PIL184	-20	21.09 × 7.14	120209	2440	0.01296	5.50 × 4.13	665454	1157	0.010872
PIL185	-20	26.36 × 7.92	121589	3127	0.01541	5.56 × 4.23	625128	3023	0.019941
PIL255	-20	12.42 × 7.95	25644	1213	0.101764	3.41 × 4.20	472774	3057	0.106619
PIL165	-30	19.57 × 14.78	258779	4728	0.00077	5.45 × 3.07	594671	589	0.006147
PIL162	-30	25.96 × 10.00	191672	4833	0.00442	8.11 × 3.97	937793	2399	0.004555
PIL164	-30	18.22 × 22.56	229261	6087	0.02164	4.04 × 5.55	598744	1515	0.017329
PIL166	-30	31.26 × 18.29	415185	8878	0.02334	8.08 × 3.98	1043672	6036	0.020205
PIL268	-30	5.76 × 20.76	93394	1039	0.101730	5.69 × 10.18	1664877	8215	0.063540

[1] Experiment from study by Qi and others (2017).

Table 3 Summary of subgrain and grain sizes

Sample No.	T (°C)	[2]ε	[3]Percentage of repeat counted grains in 2-D (%)	[4]Number density of “distinct” grains(μm^{-2})	Number density of “distinct” grains as ratio to starting material	[5]$\bar{d}$/[6]d_{median} (μm)	[8]$\overline{D}$ (μm)	[9]D_{median} (μm)	[10]$D_{q,25\%}$ (μm)	[11]$D_{q,75\%}$ (μm)	[12]D_{SMR} (μm)	[13]$\overline{D_{big}}$ (μm)	[14]$\overline{D_{small}}$ (μm)	[15]D_{peak} (μm)	[16]$d_{peak,2°}$ (μm)
						[7]$\varphi \geq 2°$									
undeformed	-	-	1.90	9.97E-06	1.00	291/280	297	291	165	413	274	-	-	300	-
PIL176	-10	0.03	9.45	3.24E-05	3.25	134/79	156	117	48	250	132	250	51	30	20
PIL163	-10	0.05	11.71	4.75E-05	4.76	104/77	125	98	54	171	110	197	58	35	25
PIL178	-10	0.08	13.47	3.82E-05	3.83	127/108	140	119	72	188	127	194	63	55	50
PIL177	-10	0.12	14.19	5.14E-05	5.15	96/77	114	90	54	155	101	184	59	40	30
[1]PIL007	-10	0.19	13.07	6.25E-05	6.27	96/78	106	88	51	143	96	174	58	50	45
PIL254	-20	0.03	7.40	5.75E-05	5.77	91/46	114	62	36	174	93	197	38	25	20
PIL182	-20	0.04	5.30	3.97E-05	3.98	103/67	148	122	62	220	131	188	42	30	25
PIL184	-20	0.08	10.61	4.73E-05	4.74	88/58	122	89	48	164	105	169	42	45	20
PIL185	-20	0.12	7.76	1.05E-04	10.49	55/40	75	53	36	85	66	132	41	30	20
PIL255	-20	0.20	12.29	1.28E-04	12.85	55/46	64	53	36	81	59	106	41	30	25
PIL165	-30	0.03	2.07	3.15E-05	3.16	108/60	149	108	48	241	126	203	38	40	20
PIL162	-30	0.05	4.87	7.27E-05	7.29	70/49	103	76	45	135	91	144	40	35	20
PIL164	-30	0.07	5.58	6.67E-05	6.69	59/38	98	61	39	113	82	158	39	30	20
PIL166	-30	0.12	6.01	1.34E-04	13.45	57/47	67	54	37	79	61	104	70	35	25
PIL268	-30	0.21	5.66	1.18E-04	11.88	42/30	60	37	29	53	50	158	35	30	20

[1] Experiment from study by Qi and others (2017). [2] True axial strain. [3] See section S4 of supplementary material for method. 2-D grains attributed to the same 3-D grain are selected by a critical misorientation angle threshold of 10°. [4] Number density of "distinct" grains, which is calculated from number of "distinct" grains divided by total grain area. "Distinct" grains are calculated by counting 2-D grains attributed to the same 3-D grain as one. 2-D grains attributed to the same 3-D grain are selected by a critical misorientation angle threshold of 10° (section 3.3.2 and section S4 in supplementary material). [5] Mean subgrain size. [6] Median subgrain size. [7] Boundary misorientation angle. [8] Mean grain size. [9] Median grain size. [10] Lower quartiles, which split off the lowest 25% of the grain sizes from the highest 75%. [11] Higher quartiles, which split off the highest 25% of the grain sizes from the lowest 75%. [12] Square mean root grain size. [13] Mean grain size of "big grains". [14] Mean grain size of "small grains". [15] Peak grain size in grain size distribution. [16] Peak grain size in subgrain size (with $\varphi \geq 2°$) distribution.

Table 4 Summary of the open half-angle of the c-axis cone (θ) from this study and the literature

Reference	Name	Mat-erial	T (°C)	No. of c-axes	θ (°)	Conditions*		True axial strain rate converted (s^{-1})	True axial strain converted (%)
This study	PIL163	H_2O	-10	353781	40	Constant displacement rate $\dot{\varepsilon} = \sim 1 \times 10^{-5} s^{-1}$	$\varepsilon = 5\%$	1.06×10^{-5}	5.0
	PIL178	H_2O	-10	201134	36		$\varepsilon = 8\%$	1.19×10^{-5}	8.0
	PIL177	H_2O	-10	235789	36		$\varepsilon = 12\%$	1.21×10^{-5}	12.0
	PIL007	H_2O	-10	163507	34		$\varepsilon = 19\%$	1.22×10^{-5}	19.0
	PIL182	H_2O	-20	213919	30		$\varepsilon = 4\%$	8.94×10^{-6}	4.0
	PIL184	H_2O	-20	120209	26		$\varepsilon = 8\%$	1.17×10^{-5}	8.0
	PIL185	H_2O	-20	121589	28		$\varepsilon = 12\%$	1.19×10^{-5}	12.0
	PIL255	H_2O	-20	25644	32		$\varepsilon = 20\%$	1.28×10^{-5}	20.0
	PIL164	H_2O	-30	229261	14		$\varepsilon = 7\%$	1.07×10^{-5}	7.0
	PIL166	H_2O	-30	415185	16		$\varepsilon = 12\%$	1.20×10^{-5}	12.0
	PIL268	H_2O	-30	93394	8		$\varepsilon = 21\%$	1.31×10^{-5}	21.0
Jacka and Maccagnan (1984)	A2	H_2O	-3	132	42	Constant load $\sigma = \sim 0.2$ MPa	$\dot{\gamma} = 3.6 \times 10^{-8} s^{-1}, \gamma = 2.4\%$	5.17×10^{-8}	3.4
	A3	H_2O	-3	98	36		$\dot{\gamma} = 4.0 \times 10^{-8} s^{-1}, \gamma = 2.9\%$	5.77×10^{-8}	4.1
	A4	H_2O	-3	111	28		$\dot{\gamma} = 6.1 \times 10^{-8} s^{-1}, \gamma = 6.8\%$	9.04×10^{-8}	9.8
	A5	H_2O	-3	95	36		$\dot{\gamma} = 6.3 \times 10^{-8} s^{-1}, \gamma = 7.3\%$	9.37×10^{-8}	10.6
	A6	H_2O	-3	108	26		$\dot{\gamma} = 6.1 \times 10^{-8} s^{-1}, \gamma = 15.0\%$	9.53×10^{-8}	22.3
	A7	H_2O	-3	96	30		$\dot{\gamma} = 6.0 \times 10^{-8} s^{-1}, \gamma = 32.5\%$	1.02×10^{-7}	51.0
Jacka and Li (2000)	N/A	H_2O	-5	87	26	Constant load, $\sigma = 0.2$ MPa	$\dot{\gamma} = 3.4 \times 10^{-8} s^{-1}, \gamma = 11.0\%$	5.18×10^{-8}	16.2
	N/A	H_2O	-10	100	32	Constant load, $\sigma = 0.2$ MPa	$\dot{\gamma} = 6.6 \times 10^{-9} s^{-1}, \gamma = 10.0\%$	9.99×10^{-9}	14.6
	N/A	H_2O	-15	173	38	Constant load, $\sigma = 0.5$ MPa	$\dot{\gamma} = 7.5 \times 10^{-8} s^{-1}, \gamma = 11.0\%$	1.14×10^{-7}	16.2
	N/A	H_2O	-15	199	32	Constant load, $\sigma = 0.4$ MPa	$\dot{\gamma} = 3.6 \times 10^{-8} s^{-1}, \gamma = 11.0\%$	5.49×10^{-8}	16.2
Piazolo et al (2013)	MD6	D_2O	-7	N/A	35	Constant displacement rate	$\dot{e} = 6 \times 10^{-7} s^{-1}, e = 10\%$	6.67×10^{-7}	11.0
	MD10	D_2O	-7	N/A	35		$\dot{e} = 2.5 \times 10^{-6} s^{-1}, e = 10\%$	2.78×10^{-6}	11.0
	MD3	D_2O	-7	N/A	35		$\dot{e} = 2.5 \times 10^{-6} s^{-1}, e = 20\%$	3.13×10^{-6}	22.0
	MD12	D_2O	-7	N/A	35		$\dot{e} = 1.0 \times 10^{-5} s^{-1}, e = 10\%$	1.11×10^{-5}	11.0
	MD4	D_2O	-7	N/A	35		$\dot{e} = 1.0 \times 10^{-5} s^{-1}, e = 20\%$	1.25×10^{-5}	22.0
	MD22	D_2O	-7	N/A	30		$\dot{e} = 1.0 \times 10^{-5} s^{-1}, e = 40\%$	1.67×10^{-5}	51.0
Montagnat et al (2015)	N/A	H_2O	-5	2838	40	Constant load, $\sigma = 0.8$ MPa	$\dot{e} = 1.2 \times 10^{-7} s^{-1}, e = 7\%$	1.30×10^{-7}	7.0
	N/A	H_2O	-5	N/A	35	Constant load, $\sigma = 0.75$	$\dot{e} = 3.9 \times 10^{-7} s^{-1}, e = 12\%$	4.43×10^{-7}	12.8
	N/A	H_2O	-5	1862	35	Constant load, $\sigma = 0.7$ MPa	$\dot{e} = 3.8 \times 10^{-7} s^{-1}, e = 13\%$	4.37×10^{-7}	13.9
	N/A	H_2O	-5	830	33	Constant load, $\sigma = 0.8$ MPa	$\dot{e} = 3.8 \times 10^{-7} s^{-1}, e = 18\%$	4.63×10^{-7}	19.9

Qi et al (2017)	PIL7	H_2O	-10	N/A	37	Constant displacement rate	$\dot{\varepsilon} = \sim 1 \times 10^{-5} s^{-1}$, $\varepsilon = 18\%$	1.10×10^{-5}	18.0
	PIL32	H_2O	-10	N/A	34		$\dot{\varepsilon} = \sim 2 \times 10^{-6} s^{-1}$, $\varepsilon = 21\%$	2.31×10^{-6}	21.0
	PIL33	H_2O	-10	N/A	26		$\dot{\varepsilon} = \sim 2 \times 10^{-4} s^{-1}$, $\varepsilon = 22\%$	2.42×10^{-4}	22.0
	PIL35	H_2O	-10	N/A	35		$\dot{\varepsilon} = \sim 1 \times 10^{-5} s^{-1}$, $\varepsilon = 13\%$	1.35×10^{-5}	13.0
	PIL36	H_2O	-10	N/A	34		$\dot{\varepsilon} = \sim 5 \times 10^{-5} s^{-1}$, $\varepsilon = 19\%$	5.02×10^{-5}	19.0
Vaughan et al (2017)	def013	H_2O	-5	206641	42	Constant displacement rate $\dot{e} = \sim 1 \times 10^{-6} s^{-1}$	$e = 3\%$	1.03×10^{-6}	3.0
	def012	H_2O	-5	309428	36		$e = 5\%$	1.05×10^{-6}	5.1
	def011	H_2O	-5	218653	38		$e = 7.5\%$	1.08×10^{-6}	7.8
	def010	H_2O	-5	335722	34		$e = 10\%$	1.11×10^{-6}	10.5
Craw et al (2018)	PIL133	H_2O	-30	N/A	0	Constant displacement rate	$\dot{\varepsilon} = \sim 2 \times 10^{-6} s^{-1}$, $\varepsilon = 20\%$	2.60×10^{-6}	20
	PIL141	H_2O	-30	N/A	0		$\dot{\varepsilon} = \sim 5 \times 10^{-6} s^{-1}$, $\varepsilon = 23\%$	7.20×10^{-6}	23
	PIL132	H_2O	-30	N/A	0		$\dot{\varepsilon} = \sim 2 \times 10^{-5} s^{-1}$, $\varepsilon = 20\%$	2.80×10^{-5}	20
Wilson et al (2020)	MD7	D_2O	-3	N/A	34	Constant displacement rate	$\dot{e} = 1.0 \times 10^{-5} s^{-1}$, $e = 20\%$	1.25×10^{-5}	22
	MD9	D_2O	-10	N/A	33		$\dot{e} = 2.5 \times 10^{-6} s^{-1}$, $e = 20\%$	3.13×10^{-6}	22
	DH24	D_2O	-20	N/A	30		$\dot{e} = 2.5 \times 10^{-6} s^{-1}$, $e = 20\%$	3.13×10^{-6}	22
	D1_5	D_2O	-3	N/A	34		$\dot{e} = 2.5 \times 10^{-6} s^{-1}$, $e = 20\%$	3.13×10^{-6}	22
	D1_1	D_2O	-1	N/A	36		$\dot{e} = 2.5 \times 10^{-6} s^{-1}$, $e = 20\%$	3.13×10^{-6}	22
Hooke and Hudleston (1981)	Coarse-100m	Natural ice	-4 ~ -6	65	22-32	Constant uniaxial strain rate $\dot{e} = 5.7 \times 10^{-11} s^{-1}$	$\bar{\gamma}_{oc} = 40\%$	7.71×10^{-11}	30
	Coarse-125m			53	28-38		$\bar{\gamma}_{oc} = 50\%$	8.37×10^{-11}	38
	Coarse-154m			82	22-32		$\bar{\gamma}_{oc} = 60\%$	9.09×10^{-11}	47
	Coarse-175m			56	20-30		$\bar{\gamma}_{oc} = 70\%$	9.90×10^{-11}	55
	Coarse-191m			93	19-29		$\bar{\gamma}_{oc} = 80\%$	1.08×10^{-10}	64
	Coarse-215m			155	18-28		$\bar{\gamma}_{oc} = 90\%$	1.18×10^{-10}	73
	Coarse-238m			61	15-25		$\bar{\gamma}_{oc} = 110\%$	1.41×10^{-10}	90
	Coarse-291m			119	14-24		$\bar{\gamma}_{oc} = 126\%$	2.00×10^{-10}	126
	Coarse-315m			102	13-23		$\bar{\gamma}_{oc} = 143\%$	2.38×10^{-10}	143
	Fine-125m			52	26		$\bar{\gamma}_{oc} = 40\%$	7.71×10^{-11}	30
	Fine-150m			89	21		$\bar{\gamma}_{oc} = 50\%$	8.37×10^{-11}	38
	Fine-175m			65	28		$\bar{\gamma}_{oc} = 60\%$	9.09×10^{-11}	47

Fine -238m	79	17	$\bar{\gamma}_{oc} = 110\%$	1.41×10^{-10}	90

* $\dot{\varepsilon}$ is the true axial strain rate, ε is the true axial strain, $\dot{\gamma}$ is the octahedral shear strain rate, γ is the octahedral shear strain, $\dot{e}$ is the engineering axial strain rate, e is the engineering axial strain, σ is the initial stress, $\bar{\gamma}_{oc}$ is the natural octahedral unit shear.

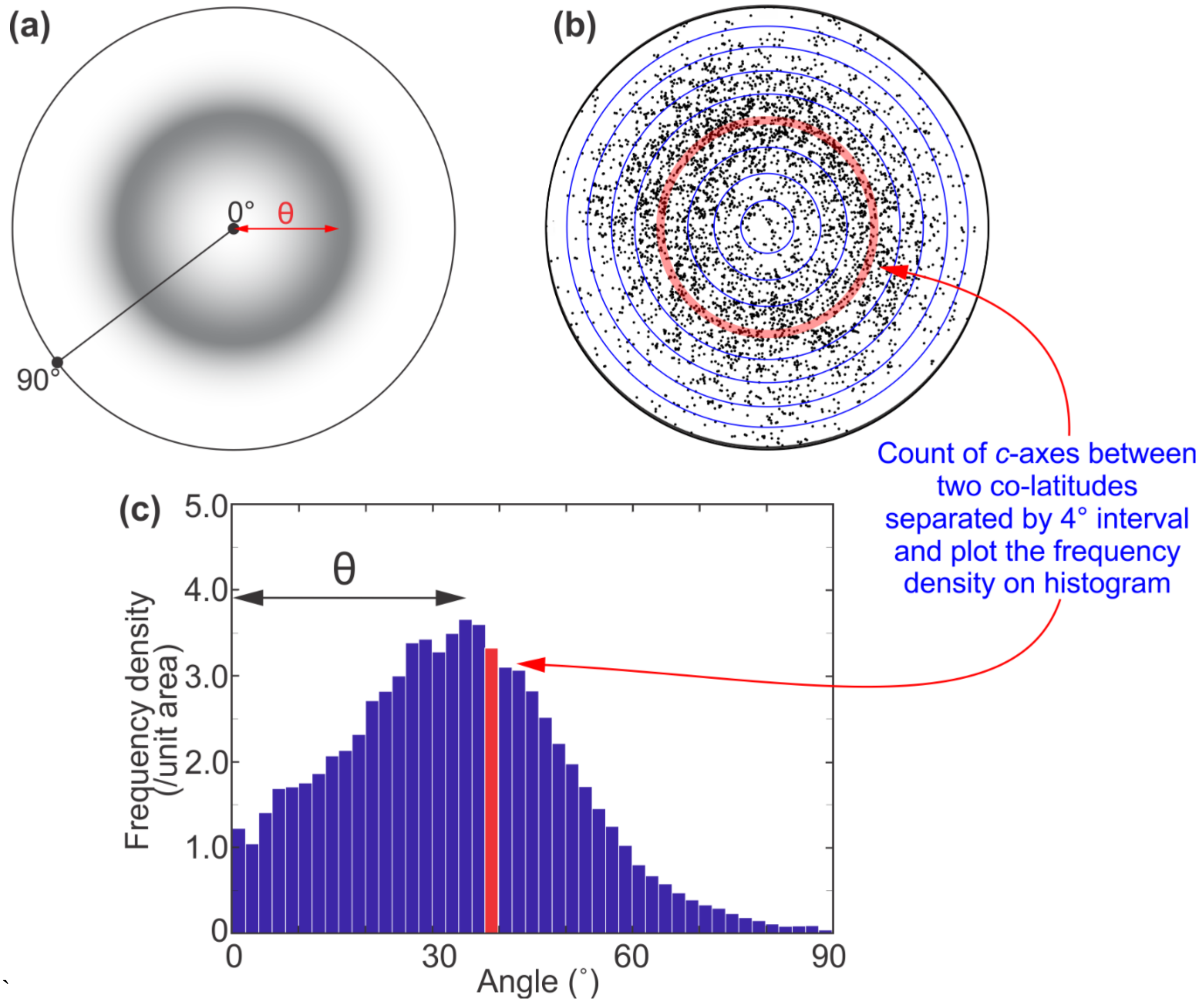

Count of *c*-axes between two co-latitudes separated by 4° interval and plot the frequency density on histogram

Figure 1. (a) Typical *c*-axes distribution at high temperatures with compression axis perpendicular to the page. **(b)** A schematic drawing explaining the method used to quantify the distribution of *c*-axes. The *c*-axes point pole figure taken from PIL178 is used as an example. The pole figure is plotted with lower hemisphere equal-area projection, and compression axis perpendicular to the page. Only 3000 points are plotted for demonstration purpose. At a given angle, red transparent circle covering co-latitudes separated by 4 degrees' interval is drawn. The points lying between the given co-latitudes (covered by the red transparent circle) are counted. The frequency density of the points is calculated from the normalised counts divided by the normalised area between the given co-latitudes. **(c)** The distribution of *c*-axes frequency density as a function of angle to the compression axis. The angle corresponds to the peak in the distribution is taken as the opening half-angle θ for the cone (small circle) shaped *c*-axes distribution. Throughout the text this is referred to as the opening-angle.

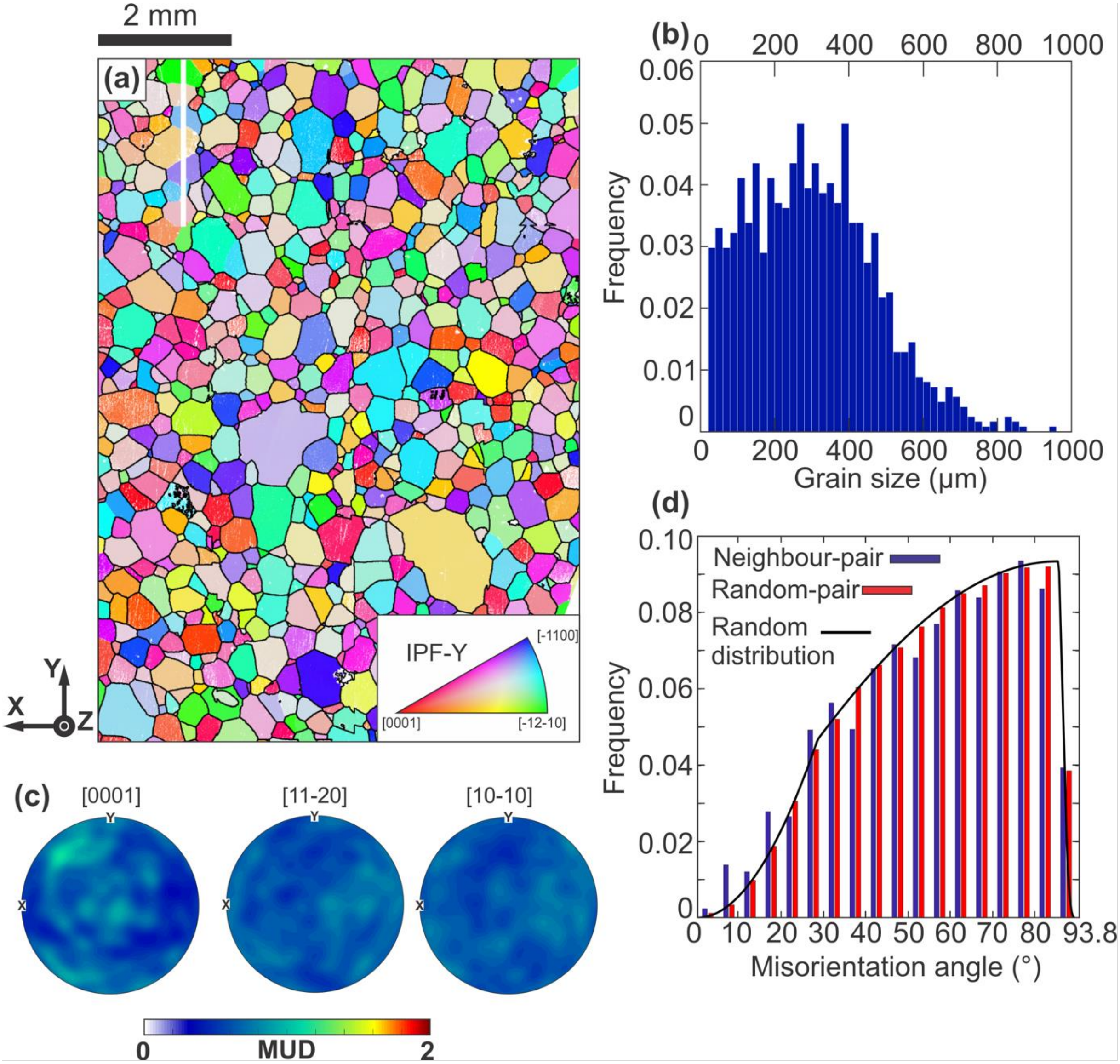

Figure 2. Microstructural details of undeformed standard ice. The EBSD data collected with 5 μm step size are presented as **(a)** Orientation maps coloured by IPF-Y, which uses the colour map to indicate the crystallographic axes that are parallel to the y-axis as shown by the black arrows. **(b)** Grain size distribution. **(c)** The distributions of orientations for [0001] (*c*-axes), [11-20] (*a*-axes) and [10-10] (poles to *m*-planes). **(d)** Misorientation angle distribution for **(a)**. Neighbour-pair misorientation angle distribution is shown with blue bars. Random-pair misorientation angle distribution is shown with red bars. Misorientation angle distribution calculated for randomly distributed ice 1h crystals are shown with black line.

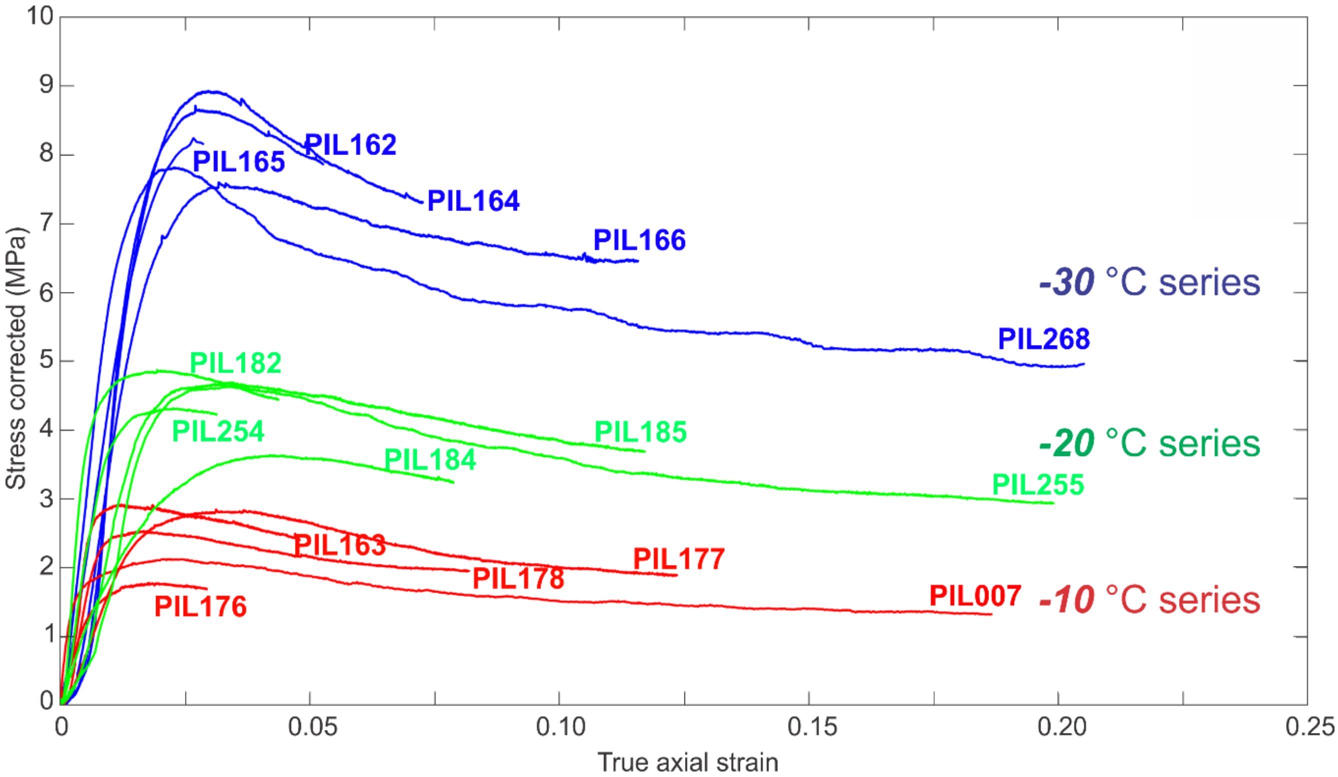

5 **Figure 3.** The stress-strain curves for all the deformed ice samples. The *x*-axis is the true axial strain (Eq. (2)). The *y*-axis is the uniaxial stress. The stress has been corrected for the change of sample cross-sectional area, assuming constant sample volume during the deformation.

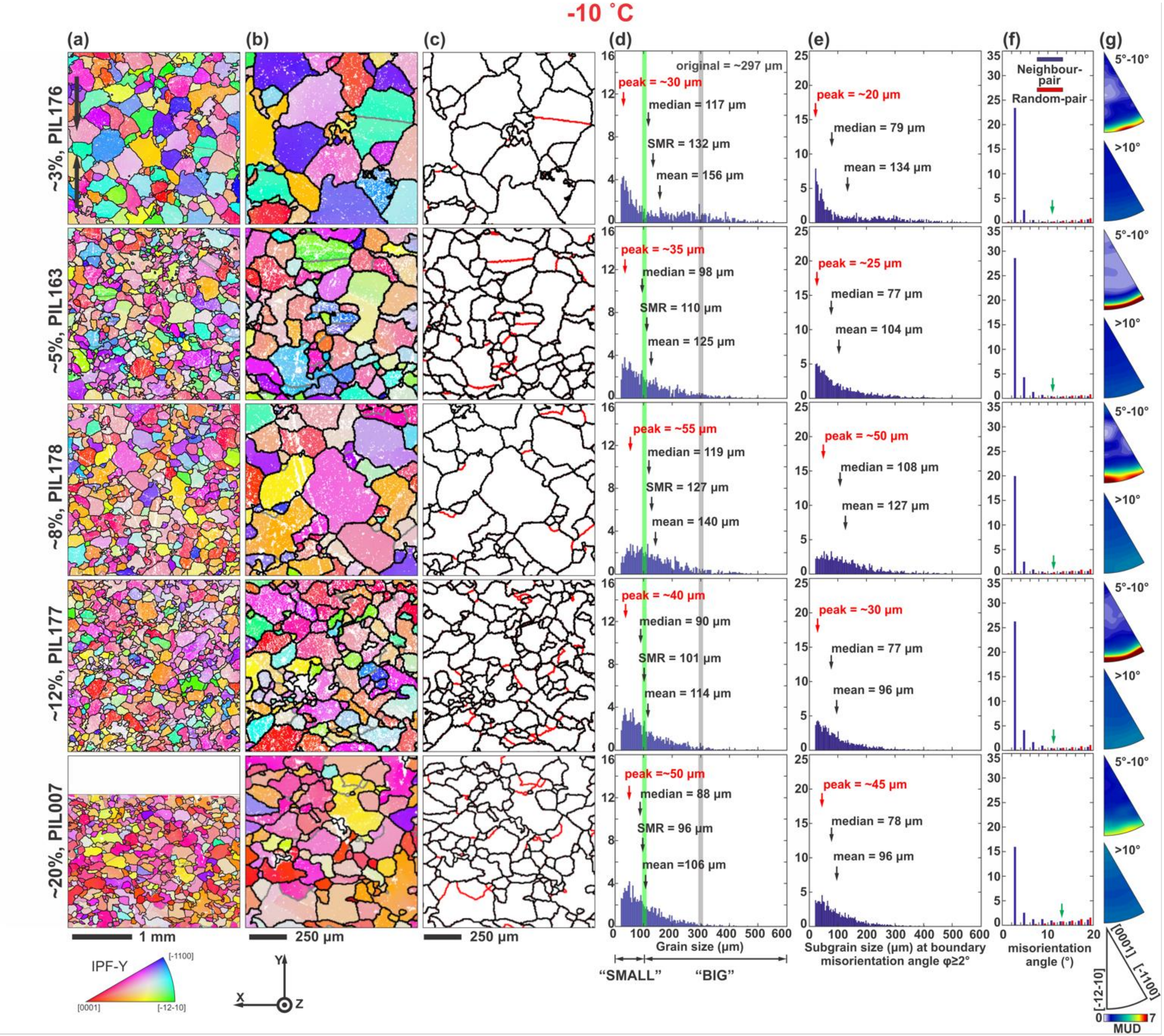
-10 ˚C
(a)
(b)
(c)
(d)
(e)
(f)
(g)
~3%, PIL176
~5%, PIL163
~8%, PIL178
~12%, PIL177
~20%, PIL007
original = ~297 µm
peak = ~30 µm
median = 117 µm
SMR = 132 µm
mean = 156 µm
peak = ~20 µm
median = 79 µm
mean = 134 µm
Neighbour-pair
Random-pair
5°-10°
>10°
peak = ~35 µm
median = 98 µm
SMR = 110 µm
mean = 125 µm
peak = ~25 µm
median = 77 µm
mean = 104 µm
peak = ~55 µm
median = 119 µm
SMR = 127 µm
mean = 140 µm
peak = ~50 µm
median = 108 µm
mean = 127 µm
peak = ~40 µm
median = 90 µm
SMR = 101 µm
mean = 114 µm
peak = ~30 µm
median = 77 µm
mean = 96 µm
peak =~50 µm
median = 88 µm
SMR = 96 µm
mean =106 µm
peak = ~45 µm
median = 78 µm
mean = 96 µm
1 mm
250 µm
250 µm
Grain size (µm)
"SMALL"
"BIG"
Subgrain size (µm) at boundary misorientation angle φ≥2°
misorientation angle (°)
IPF-Y
[-1100]
[0001]
[-12-10]
Y
X
Z
[0001]
[-1100]
[-12-10]
0
7
MUD

Figure 4. Microstructural analyses of deformed ice samples at -10 °C. Axial true strain increases from ~3% on top to ~20% to bottom. The EBSD data collected with 5 μm step size are presented as **(a)** orientation maps at low magnification and **(b)** orientation maps of selected areas at high magnification. Orientation maps are coloured by IPF-Y, which uses the colour map to indicate the crystallographic axes that are parallel to the vertical shortening direction as shown by the black arrows. Ice grain boundaries with a misorientation larger than 10° are shown black. Non-indexed pixels are shown white. Subgrain boundaries, where misorientation angles between neighbouring pixels are between 2° and 10°, are shown grey. Maps show data without interpolation. **(c)** Distribution of subgrain boundaries. Subgrain boundaries are shown red. Grain boundaries are shown black. **(d)** Distribution of ice grain size presented in 4 μm bins. Mean, median and square mean root (SMR) diameters are indicated by black arrows. The main peak of the grain size distribution is indicated by a red arrow. Vertical grey line marks the mean grain size of the starting material. Vertical green line marks the threshold grain size between "big grains" and "small grains" (see text). **(e)** Distribution of subgrain size presented in 4 μm bins. The subgrain size is calculated by applying the boundary misorientation angle of $\varphi \geq 2°$. **(f)** Distribution of neighbour-pair and random-pair misorientation angles. The misorientation angle at which neighbour-pair frequency reduces to be equal to the random-pair frequency is marked with a green arrow. **(g)**. Misorientation axes distribution plotted in crystal reference frame as contoured inverse pole figure (IPF). The contoured IPFs are coloured by MUD. Neighbour-pair misorientation axes for neighbouring pixels with misorientation angles of 5°-10° are presented in the upper box. Grain boundary (>10°) misorientation axes using pixels along the grain boundaries of neighbouring grains are presented in the lower box.

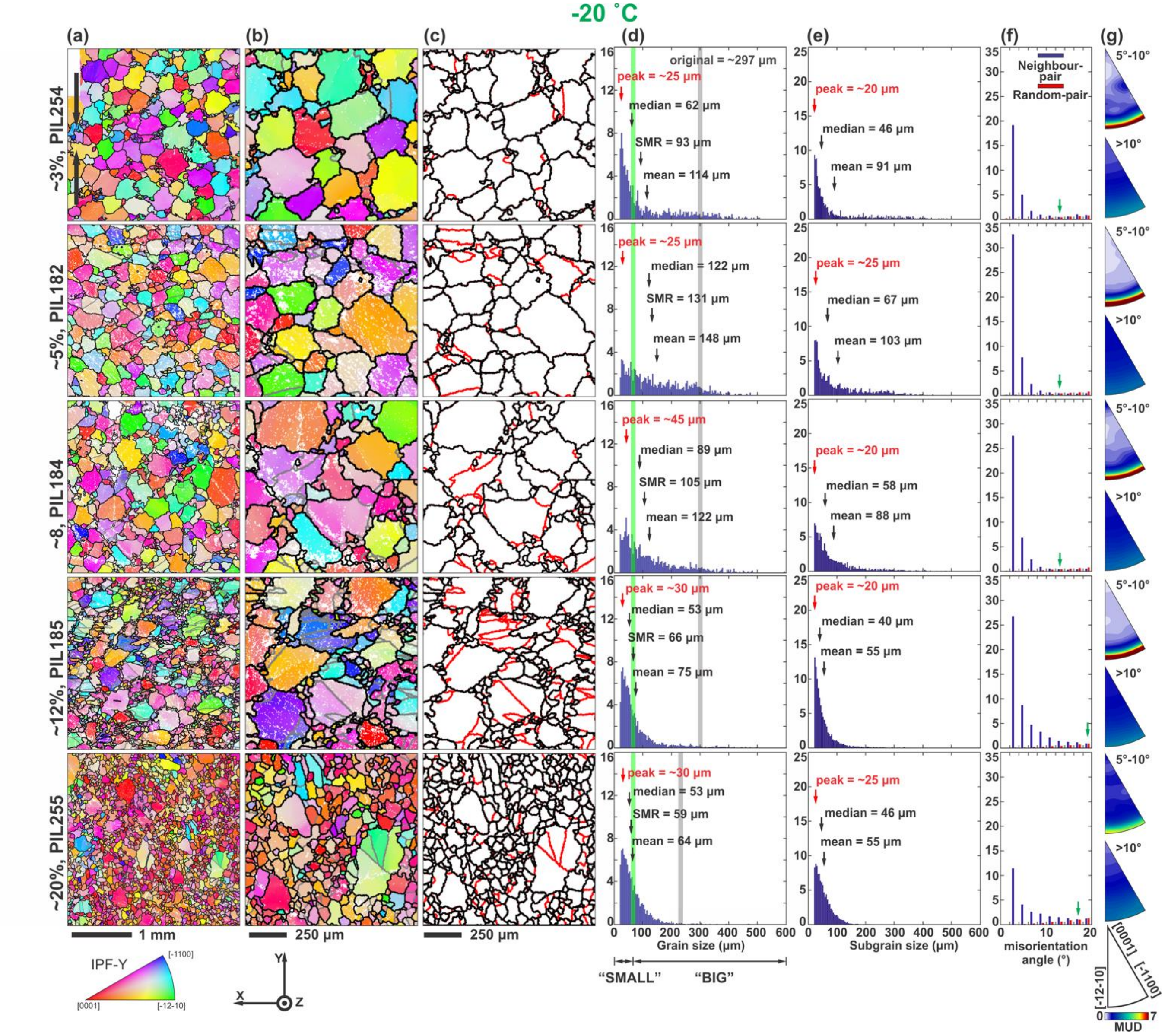

Figure 5. Microstructural analyses of deformed ice samples at -20 °C. Axial true strain increases from ~3% on top to ~20% to bottom. The descriptions of columns **(a)** to **(g)** are the same as in Fig. 4.

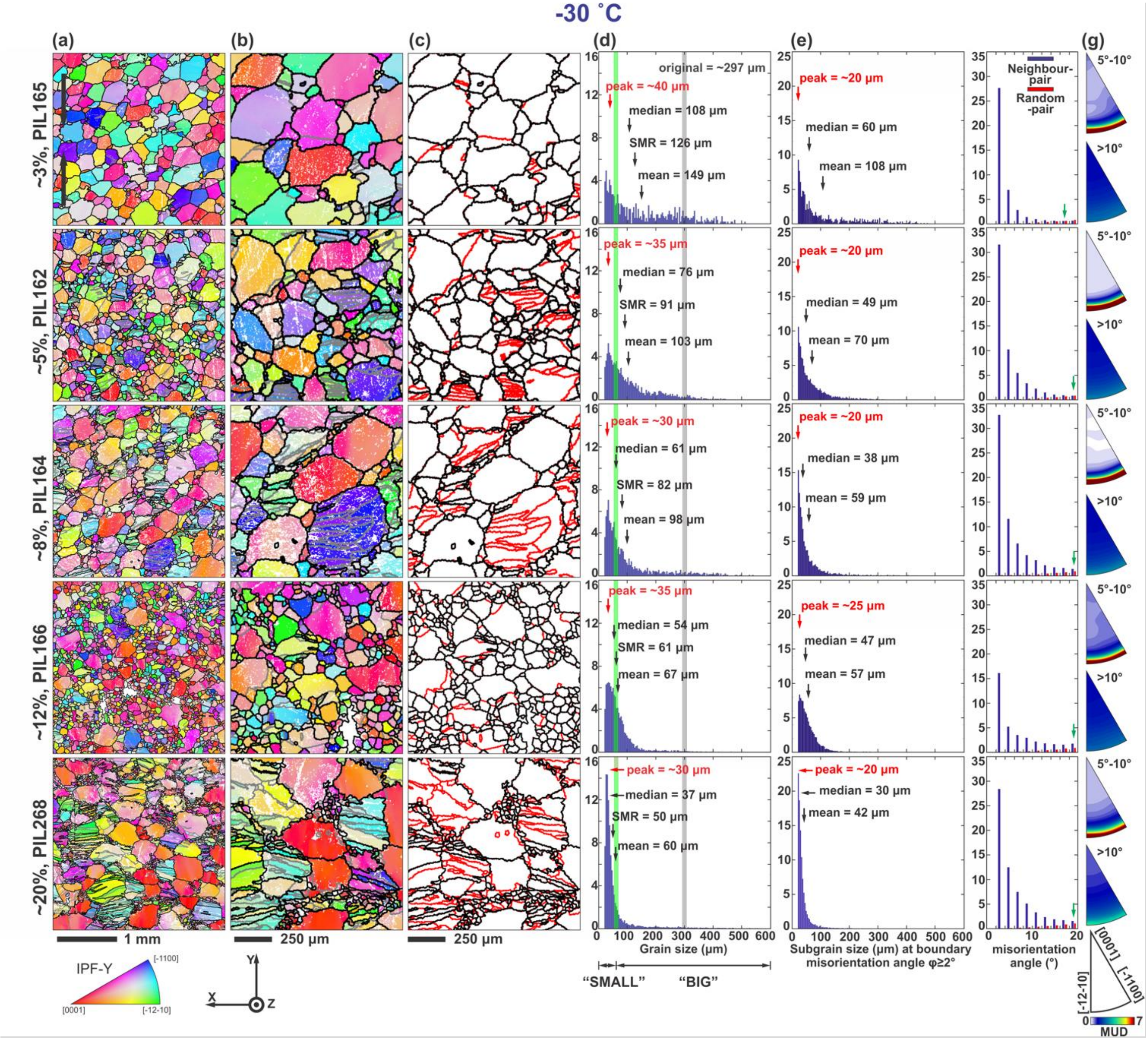

Figure 6. Microstructural analyses of deformed ice samples at -30 °C. Axial true strain increases from ~3% on top to ~20% to bottom. The descriptions of columns **(a)** to **(g)** are the same as in Fig. 4.

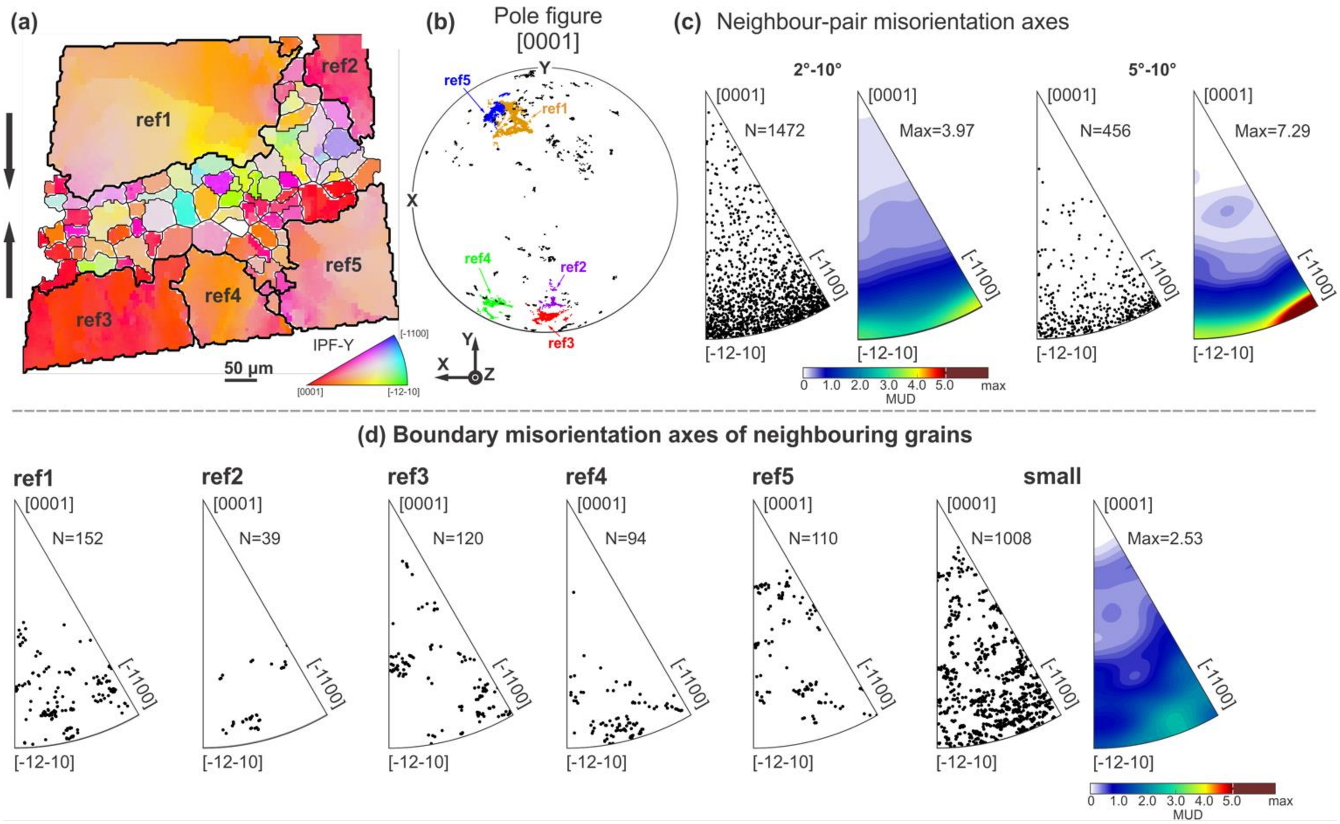

Figure 7. Misorientation axes analyses of a sub-area from the EBSD map of sample PIL268 (-30 °C, ~20% strain). **(a)** orientation map coloured by IPF-Y, which uses the colour map to indicate the crystallographic axes that are parallel to the vertical shortening direction as shown by the black arrows. Ice grain boundaries with a misorientation larger than 10° are shown black. "Big" reference grains are shown with thick black boundaries. "Small" grains are shown with thin black boundaries. **(b)** The pole figure of *c*-axes corresponding to orientations of all pixels of grains in **(a)**. *c*-axes of "small" grains are shown with black dots. *c*-axes of "big" reference grains are shown with dots coloured by non-black colours. **(c)** Neighbour-pair misorientation axes for neighbouring pixels with misorientation angles of 2°-10° and 5°-10° corresponding to **(a)**. The misorientation axes are plotted in crystal reference frame as inverse pole figure (IPF). The IPF either shows all points or coloured by MUD. The number of points or maximum value of MUD are given next to each IPF. **(d)** Boundary misorientation axes of "big" reference grains and corresponding neighbouring grains, and neighbouring grains among "small" grains. Grain boundary misorientation axes are calculated using pixels along the grain boundaries of neighbouring grains.

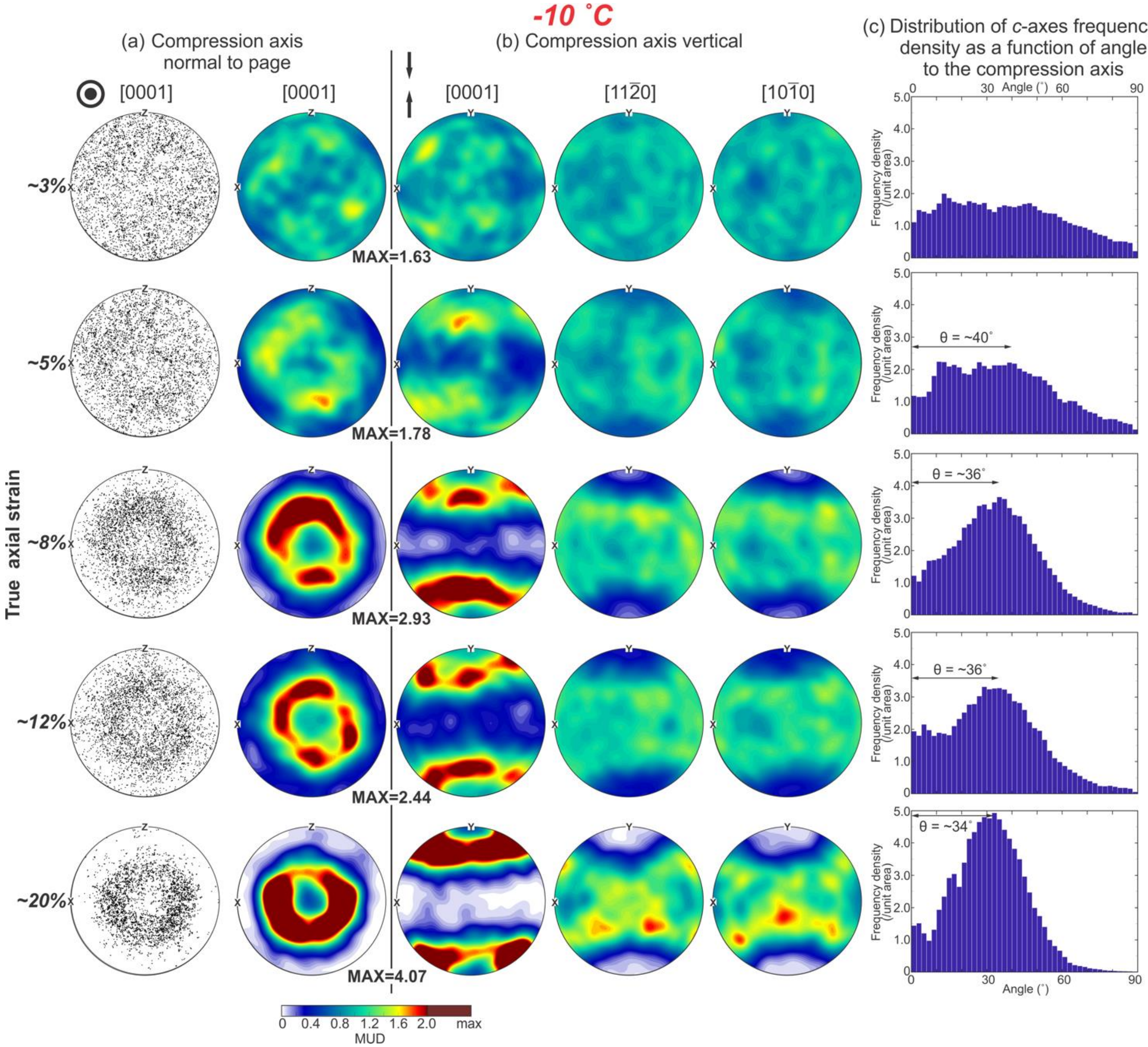

Figure 8. Crystallographic preferred orientations (CPOs) from EBSD data with 30 µm step size for ice samples deformed at -10 °C. Axial true strain increases from ~3% on top to ~20% to bottom. **(a)** The distributions of [0001] (*c*-axes) orientations plotted as point pole figures with 5000 randomly selected points and contoured pole figures. The compression axis is perpendicular to the page. **(b)** The distributions of orientations for [0001] (*c*-axes), [11-20] *a*-axes and [10-10] (poles to *m*-planes) plotted as contoured pole figures. The compression axis is vertical. Contoured pole figures are contoured based on MUD. The maximum value of MUD for the *c*-axis CPO of each sample is given between columns (a) and (b). **(c)** Distributions of the [0001] axes frequency density as a function of angle to the compression axis. Open half-angle *θ* of the cone (small circle) is presented on each histogram.

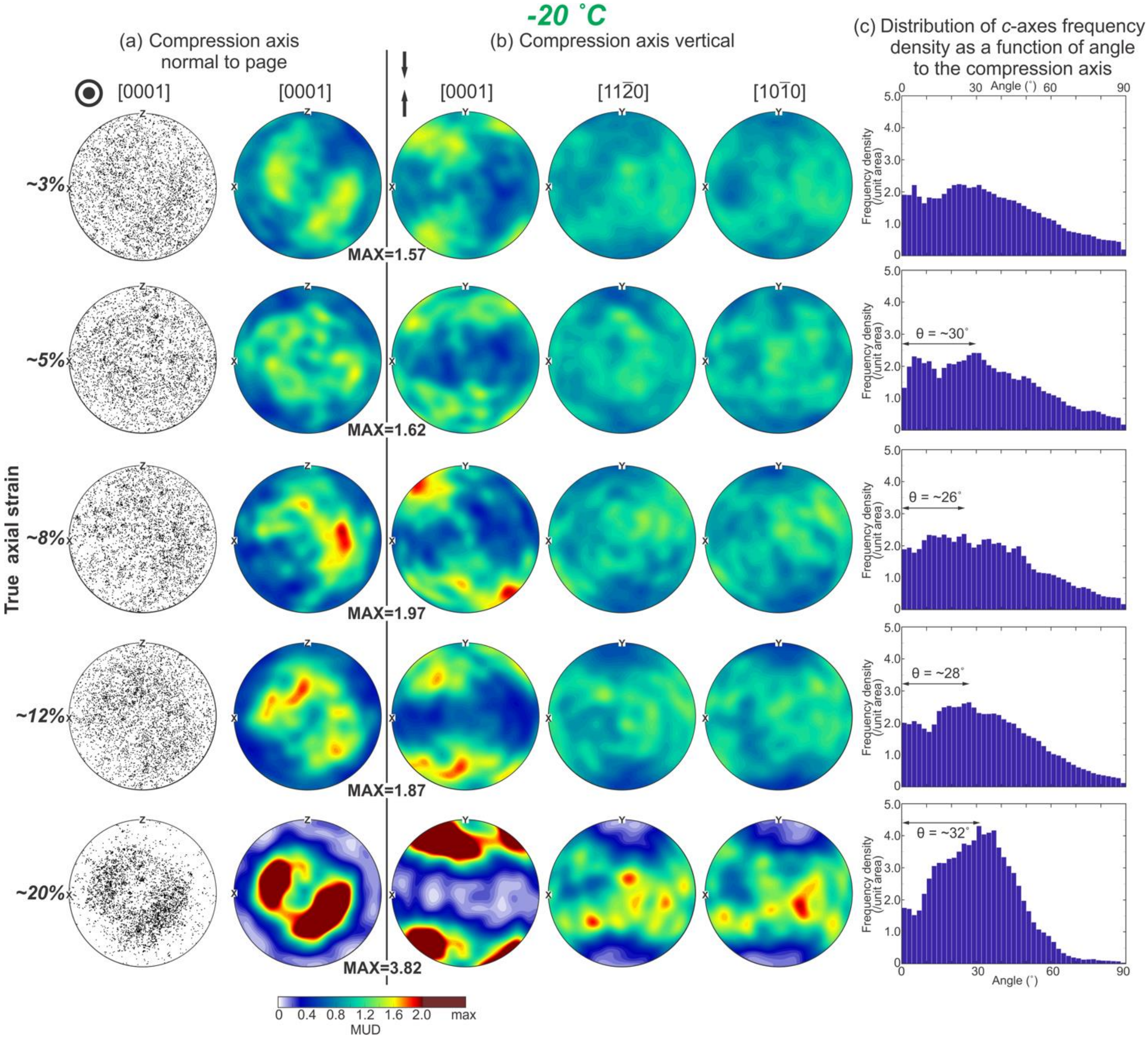

Figure 9. Crystallographic preferred orientations (CPOs) from EBSD data with 30 µm step size for ice samples deformed at -20 °C. Explanation of annotations and the descriptions of sections **(a)** to **(c)** are the same as in Fig. 8.

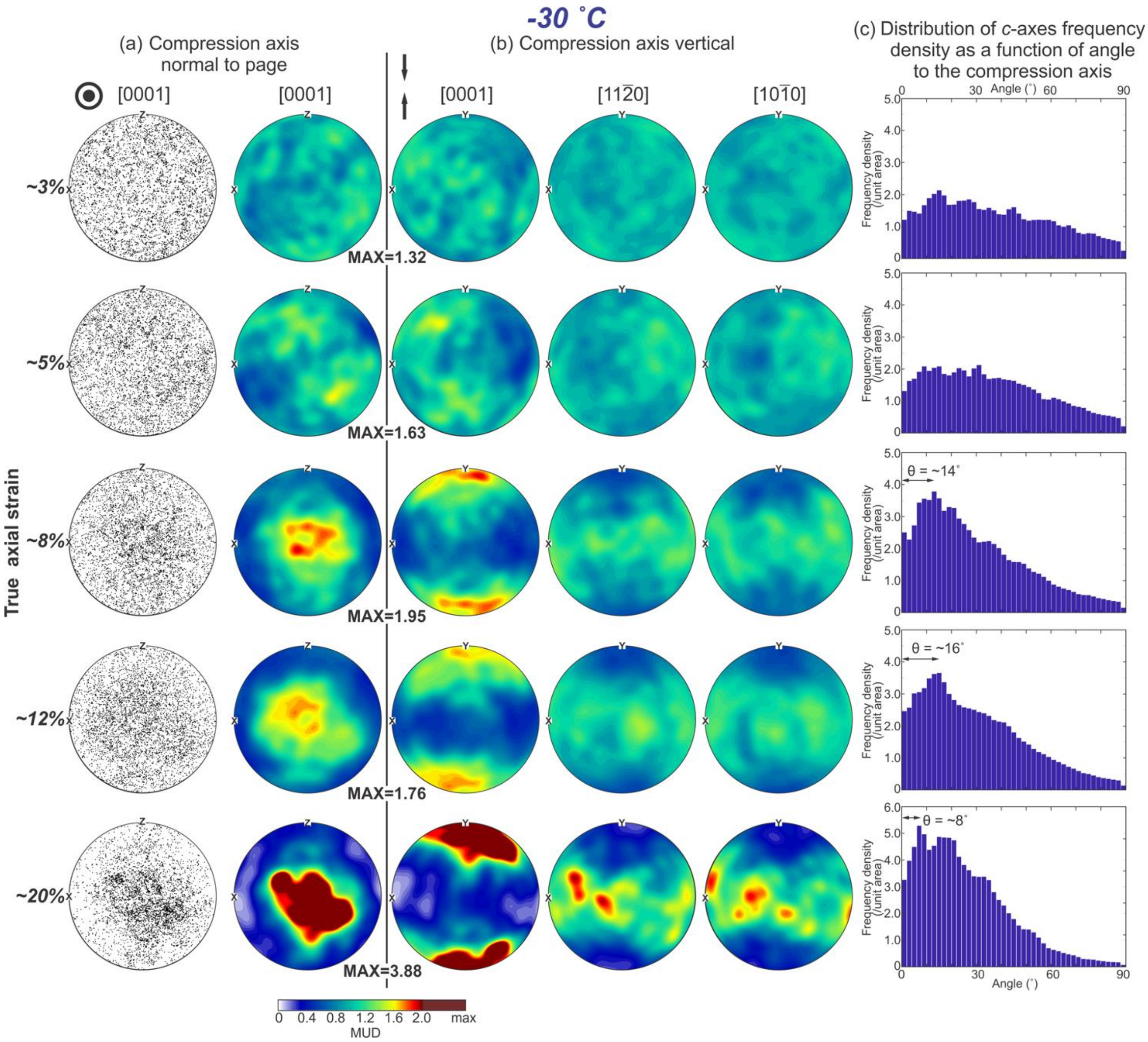

Figure 10. Crystallographic preferred orientations (CPOs) from EBSD data with 30 µm step size for ice samples deformed at -30 °C. Explanation of annotations and the descriptions of sections **(a)** to **(c)** are the same as in Fig. 8.

5

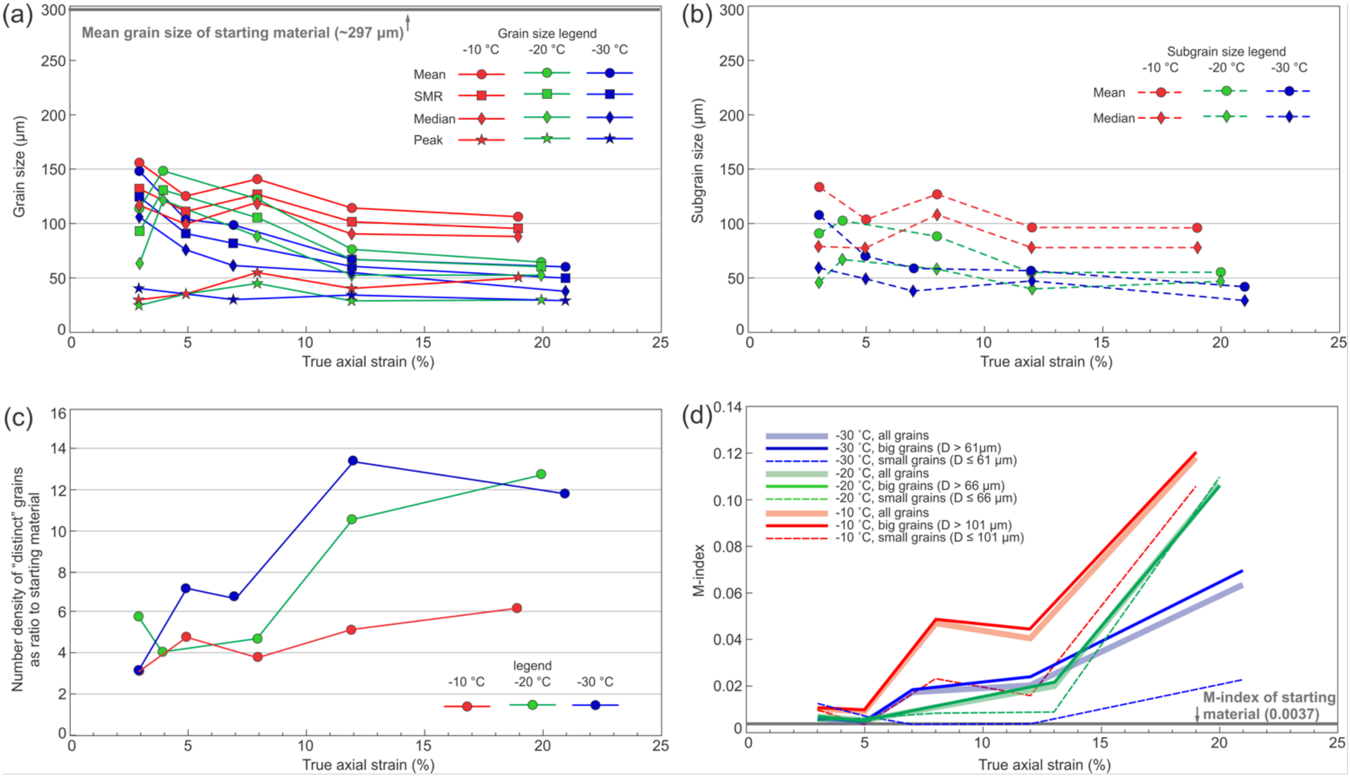

Figure 11. (a) Variation in the mean, SMR (square mean root), median and peak grain size as a function of true axial strain in each temperature series. **(b)** Variation in the mean, and median subgrain grain size at boundary misorientation angle threshold of 2° as a function of true axial strain in each temperature series. **(c)** Variation in number density of "distinct" grains as ratio to starting material relative to true axial strain in each temperature series. **(d)** Variation in CPO strength (M-index) as a function of true axial strain for different grain size categories in each temperature series. M-indices are calculated from 5 µm EBSD data.

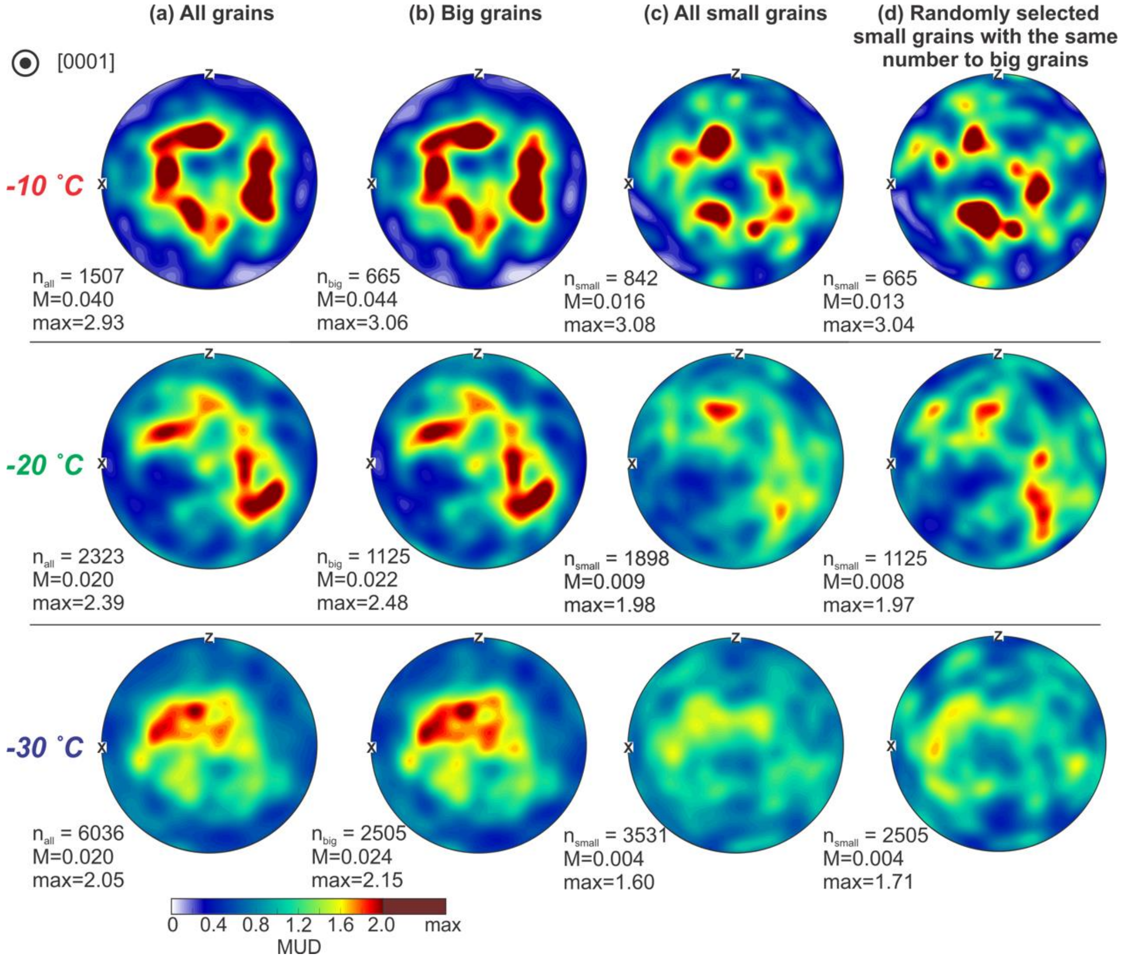

Figure 12. Contoured [0001] (*c*-axis) CPOs of **(a)** all grains, **(b)** “big grains”, **(c)** “small grains” and **(d)** randomly selected “small” grains with the same grain number of “big” grains, for the samples deformed to ~12% strain at different temperatures. The number of grains, M-indices and max MUD values are marked on the bottom left of pole figures. The *c*-axis CPOs are calculated based on all pixels taken from the EBSD data with 5 µm step size. Compression axis is in the centre of the stereonets.

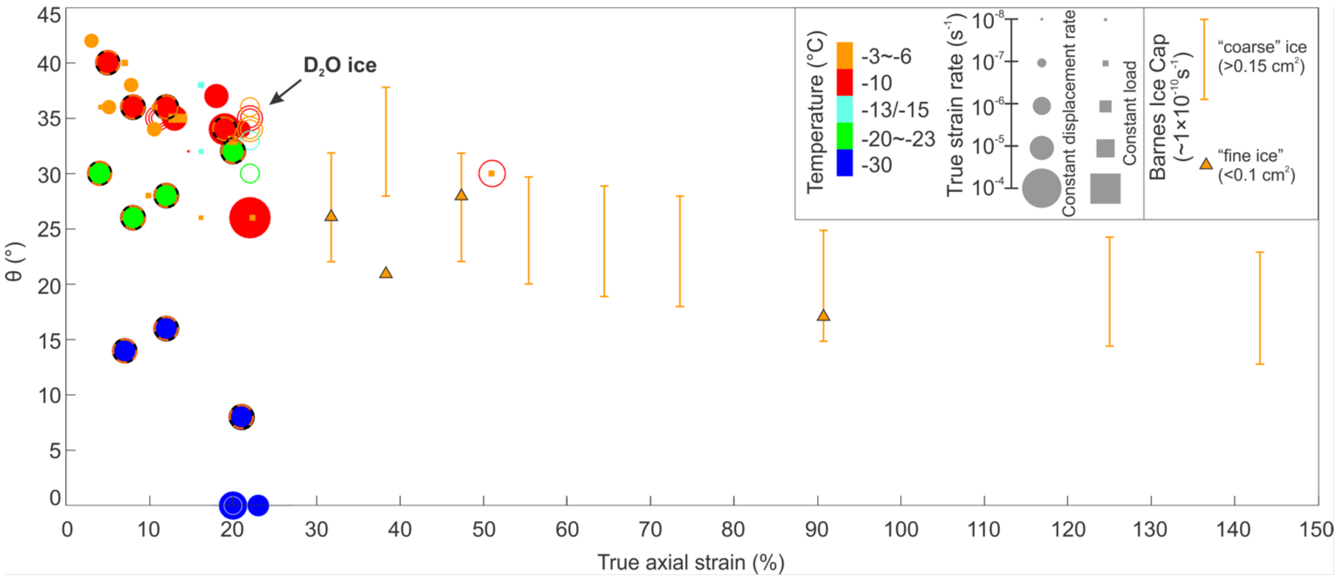

Figure 13. Plot of the relationship between the opening-angle, θ, of the cone-shaped *c*-axis CPO and the true strain. The data come from this study and the literature (Table 4). The data from naturally deformed ice (Hooke and Hudleston, 1981) are illustrated by bars with whiskers (cover uncertainty range of the open angle) for "coarse" ice and triangles with black edges for "fine" ice. The data from constant displacement rate experiments on D_2O ice (Piazolo et al, 2013; Wilson et al., 2020) are illustrated by hollow circles. The deformation of D_2O ice at -7 °C is a direct analogue for deforming H_2O ice at −10 °C (Wilson et al., 2019). The data from constant displacement rate experiments on H_2O ice (this study, Vaughan et al., 2017, Qi et al., 2017, Craw et al., 2018) are illustrated by filled circles. Data from this study are highlighted by orange-black edges. The data from constant load experiments (Jacka and Maccagnan, 1984; Jacka and Li, 2000; Montagnat et al., 2015) are illustrated by solid squares. Each marker is sized and coloured by the corresponding true strain rate and temperature, respectively. For all experiments the strain rate shown is the strain rate at the end of the experiment.

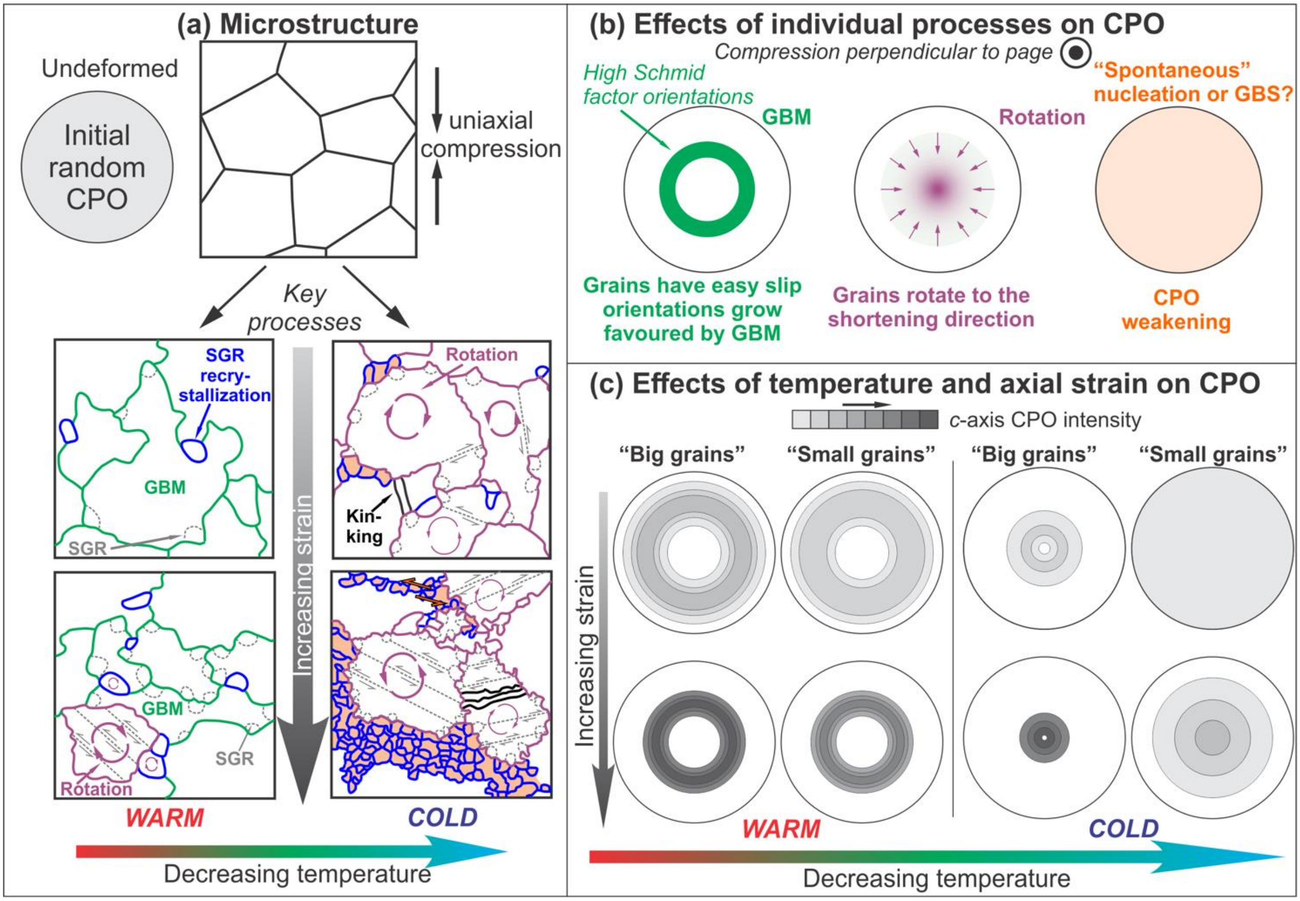

Figure 14. Schematic drawing of the microstructure and CPO development in ice deformed under uniaxial compression. **(a)** The effects of temperature and axial strain on the microstructural evolution. Grains undergoing different deformation processes are marked by different colours, with interpretations of the processes presented. **(b)** The effects of individual processes on CPO development. **(c)** The development of CPOs for "small grains" and "big grains" with strain at different temperatures. Starting point (shown in (a)) is a random CPO. SGR: subgrain rotation. GBM: grain boundary migration. GBS: grain boundary sliding.